ABSTRACT

Title of Document: EFFECT OF STRUCTURAL HEAT

CONDUCTION ON THE PERFORMANCE

OF MICRO-COMBUSTORS AND MICRO-

THRUSTERS

Timothy Thierry Leach, Doctor of Philosophy, 2005

Directed By: Professor Christopher P. Cadou, Department of Aerospace Engineering

This thesis investigates the effect of gas-structure interaction on the design and performance of miniaturized combustors with characteristic dimensions less than a few millimeters. These are termed 'micro-combustors' and are intended for use in devices ranging from micro-scale rocket motors for micro, nano, and pico-satellite propulsion, to micro-scale engines for micro-Unmanned Air Vehicle (UAV) propulsion and compact power generation. Analytical models for the propagation of a premixed laminar flame in a micro-channel are developed. The models' predictions are compared to the results of more detailed numerical simulations that incorporate multi-step chemistry, distributed heat transfer between the reacting gas and the combustor structure, heat transfer between the combustor and the environment, and heat transfer within the combustor structure. The results of the modeling and simulation efforts are found to be in good qualitative agreement and demonstrate that

the behavior of premixed laminar flames in micro-channels is governed by heat transfer within the combustor structure and heat loss to the environment.

The key findings of this work are as follows: First, heat transfer through the micro-combustor's structure tends to increase the flame speed and flame thickness. The increase in flame thickness with decreasing passage height suggests that micro-scale combustors will need to be longer than their conventional-scale counterparts. However, the increase in flame speed more than compensates for this effect and the net effect is that miniaturizing a combustor can increase its power density substantially. Second, miniaturizing chemical rocket thrusters can substantially increase thrust/weight ratio but comes at the price of reduced specific impulse (i.e. overall efficiency). Third, heat transfer through the combustor's structure increases steady-state and transient flame stability. This means that micro-scale combustors will be more stable than their conventional-scale counterparts. Fourth and finally, the extended temperature profile associated with the broadened flame causes a different set of elementary reactions to dominate the operation of the overall reaction mechanism at the micro-scale. This suggests that new chemical mechanisms may need to be developed in order to accurately simulate combustion at small-scales. It also calls into question the efficacy of single-step mechanisms presently used by other researchers.

EFFECT OF STRUCTURAL HEAT CONDUCTION ON THE PERFORMANCE
OF MICRO-COMBUSTORS AND MICRO-THRUSTERS

By

Timothy Thierry Leach

Dissertation submitted to the Faculty of the Graduate School of the
University of Maryland, College Park, in partial fulfillment
of the requirements for the degree of
Doctor of Philosophy
2005

Advisory Committee:
Professor Christopher P. Cadou, Chair/Advisor
Professor James Baeder
Professor Georg Dolzmann
Professor Andre Marshall
Professor Kenneth Yu

Dedication

To Jennifer and Anne-Sophie.

Acknowledgements

I would like to express my sincere gratitude to my advisor Chris Cadou for all he did for me during my graduate education at the University of Maryland. Thank you for supporting me, teaching me how to do research, giving me the opportunity to take initiative, believing in me, and for all the interesting discussions.

I would also like to thank the members of my dissertation committee for their time and insightful discussions: Professors Baeder, Dolzmann, Marshall, and Yu.

I would as well like to acknowledge the great help of Dr. Greg Jackson from the department of Mechanical Engineering at the University of Maryland, who provided me with the initial version of the numerical model used in this work and assisted in its modification.

Also, I would like to thank all of my friends at the University of Maryland: Anand, Daniel, John, Kiran, Scott, Shyam.

I would also like to thank Anand for all the interesting discussions and for his experimental data.

I would also like to express my deepest gratitude to Dr. Edna Hokenson for her incredible generosity which helped Jennifer and me so much. You will always be in our thoughts. RIP.

Table of Contents

List of Tables

List of Figures

List of Abbreviations

A Cross-sectional area

a Surface area per unit volume

a Non-dimensional oscillation amplitude

C_P Heat capacity at constant pressure

D Diffusion coefficient

E_a Activation energy

H Channel height

h Enthalpy

h_T Heat transfer coefficient

I_{sp} Specific impulse

Kn Knudsen number

k Thermal conductivity

L Channel length

M Mach number

Nu Nusselt number

P Pressure

R Gas constant

R Thermal resistance

RR Reaction rate

Re Reynolds number

r Ratio of throat to inlet nozzle heights

S_L Laminar flame speed

S/V Surface-to-volume ratio

T Temperature

T Thrust

T Oscillation period

T/W Thrust-to-weight ratio

t Thickness of the plate

U, u Velocity

V Volume

W Molecular weight

W Width of the plates

$\dot{w}$ Power generated by the combustion process

$\dot{w}_D$ Power density

x Streamwise coordinate

Y Mass fraction

Greek letters

β See Equation (2-4)

Dp Pressure loss

δ_{ph} Pre-heat zone thickness

δ_r Reaction zone thickness

e Small arbitrary velocity

η Efficiency

Φ Equivalence ratio

g Ratio of specific heats

λ Ratio of the thermal conductivity of the structure to the thermal conductivity

of the gas

m Viscosity

$\dot{\omega}$ Chemical production rate

Subscripts

ad   Adiabatic

bl   Boundary layer

ch   Channel

e, env Environment

eff   Effective

f   Flame

i   Ignition

k   Quantity associated with species k

fr   Freely propagating value

m   Mean

r, g   Gas

s   Structure

th   Thermal

0,i   Inlet

o   Overall

Chapter 1:   Introduction

1.1 Motivation

1.1.1. Nano and pico-satellite propulsion

Over the past several years, the Aerospace community has become increasingly interested in building smaller satellites weighing between 0.1 kg and 10 kg. These types of satellites are termed pico (0.1-1kg) and nano-satellites (1-10kg). Several factors are driving the satellite miniaturization trend. First, the miniaturization of electronics and computer systems makes it possible to reduce the weight and the volume of the avionics previously required to operate a satellite. Consequently, it is now possible to achieve the mission of a normal size satellite using a spacecraft whose size and payload weight are much smaller, thereby to lowering the mission cost. Second, constellations of many smaller satellites operating cooperatively offer increased reliability and enable new missions. Third, small satellites could serve as mobile platforms for satellite inspection, refueling, and repair.

However, the technology associated with these small satellites is in its infancy and much more research needs to be conducted in order to be able to fully take advantage of the possibilities offered by nano and pico-satellites. One major challenge is the development of small, light-weight propulsion systems that are also have adequate levels of efficiency. Existing micro-propulsion systems are very inefficient (Mueller[1]).

There are several reasons why chemical propellants are attractive energy storage medium for small satellite propulsion systems. First, the mass-specific energy density of liquid fuels is at least on the order of 50 MJ/kg, which is relatively high compared to, for example, the energy density of batteries which is on the order of 1 MJ/kg. The volume-specific energy density of such fuels is also large, which is a great advantage for aerospace applications where volume as well as mass is a decisive parameter. Second, combustion is a very well established and reliable means for energy release. Since it is well understood at regular scale, one can expect that it can be well-understood at microscale and this should make it very reliable. Third, it has been shown[2] that combustion in small volumes is possible in spite of the greatly increased heat loss to the environment.

1.1.2. Replacement for batteries

Owing to the large energy density of liquid hydrocarbon (HC) fuels compared to electro-chemical materials (~100MJ/kg vs. ~1MJ/kg), micro-combustors fueled by liquid HCs could replace batteries, provided that the energy in the hydrocarbon fuels is converted with at least 1% efficiency. These power systems could be used in a wide range of devices that are presently powered by batteries. If conversion efficiencies greater that 10% are achieved, the operating lifetime of these systems could be increased by a factor greater than 10. The use of a liquid fuel also offers the possibility of easy refueling.

1.1.3. Micro-engines for UAVs

The development of micro-UAVs (Unmanned Air Vehicles) depends on the availability of efficient and reliable powerplants. Figure 1-1 illustrates how the range of a micro-UAV depends on the method used to store and release energy in the vehicle.
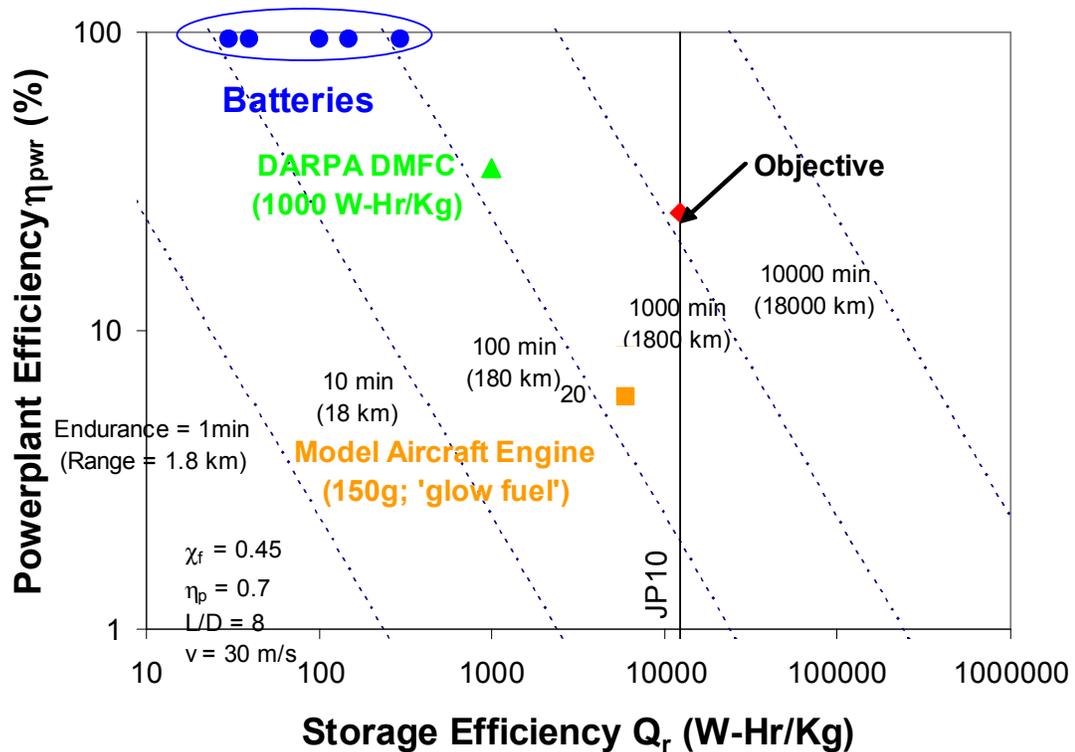
Figure 1-1: Estimated range of a micro-UAV as a function of energy storage efficiency and energy conversion efficiency.

The range of the vehicle is computed using the Brequet range equation[3] ($R = \eta_o \eta_p \left(\dfrac{L}{D}\right) \dfrac{Q_r}{g} \ln(1 + x_f)$) for a fixed-wing UAV with lift-to-drag ratio L/D of 8, propulsion efficiency η_p of 70%, ground velocity of 30 m/s, and fuel mass fraction x_f

3

of 45%. The figure suggests that in order to achieve the range objective, an internal combustion engine burning a heavy fuel (JP10) with efficiency greater than 20% appears to be the only option.

1.2 Challenges

One major barrier to developing practical H.C. fueled micro-rockets and micro-power systems is heat loss to the environment. Micro-combustors are very susceptible to this because their surface to volume ratio decreases with decreasing combustor size. As an example, consider the flow in the simple channel pictured in figure 1-2.
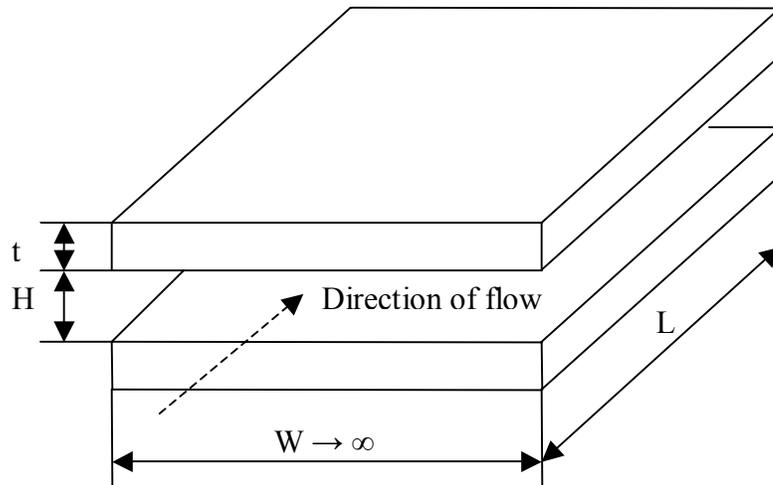
Figure 1-2: Diagram of a simple channel/micro-combustor.

The interior surface area can be expressed as:

$$S = 2WL \qquad (1\text{-}1)$$

while the interior volume is:

4

$$V = HWL \qquad (1\text{-}2)$$

Consequently the surface to area ratio is:

$$S_v \equiv \frac{S}{V} = \frac{2}{H} \qquad (1\text{-}3)$$

This surface-to-volume ratio increases as the size of the combustor is reduced. Figure 1-2 shows the evolution of the surface to volume ratio in such a reactor as a function of the passage height H. It shows that as the size of combustors decreases, the surface area increases with respect to the enclosed volume. Since the heat loss is proportional to surface area while the heat evolved during the chemical reaction is proportional to the enclosed volume, figure 1-2 suggests that as the size of combustors decreases, heat loss to the environment decreases more slowly than the amount of heat released by the combustion process.
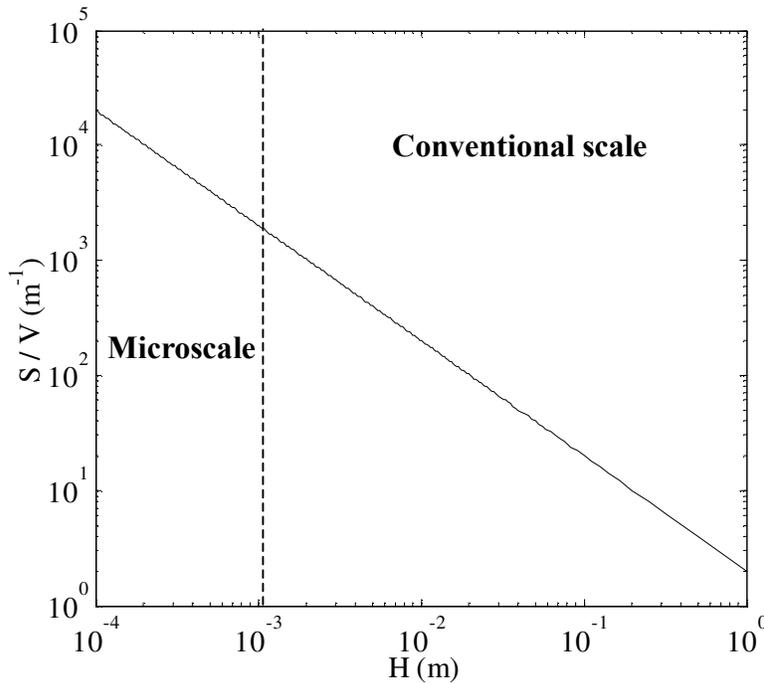
Figure 1-3: Evolution of the surface to area ratio as a function of passage height in a parallel plate reactor.

When heat loss becomes larger than heat release during combustion, chemical reaction cannot be sustained and the flame quenches.

Another major barrier to building efficient micro-combustors arises from recent experimental work[4] that indicates that flames in micro-combustors may be broader than in conventional devices. This, in turn, suggests that the distance needed to convert the fuel to products may have to be larger than in conventional combustors and that the design and construction of efficient micro-combustors may be more complicated than originally anticipated. The topic of flame broadening will be investigated in greater detail in Chapter 2.

Another challenge arises from the need to achieve high power density. This requires small length scales and large flow velocities which lead to small residence times. However, this also lowers the Damkohler number (i.e. the ratio of residence time to chemical time) making it potentially difficult to sustain a combustion wave.

Finally, the small length scales also make it difficult to use turbulent processes to increase the reaction rate and hence the power density. This is illustrated in figure 1-4 that shows the influence of the passage height on the Reynolds number for a flow of air at 300K in the simple channel of figure 1-1 at a velocity of 1m/s. For passage heights less than 2 cm, the flow is laminar and consequently turbulent enhancement of mixing and reaction rate cannot be achieved. Note that all the combustor dimensions considered in this work fall under this 2 cm threshold such that turbulence does not come into play.
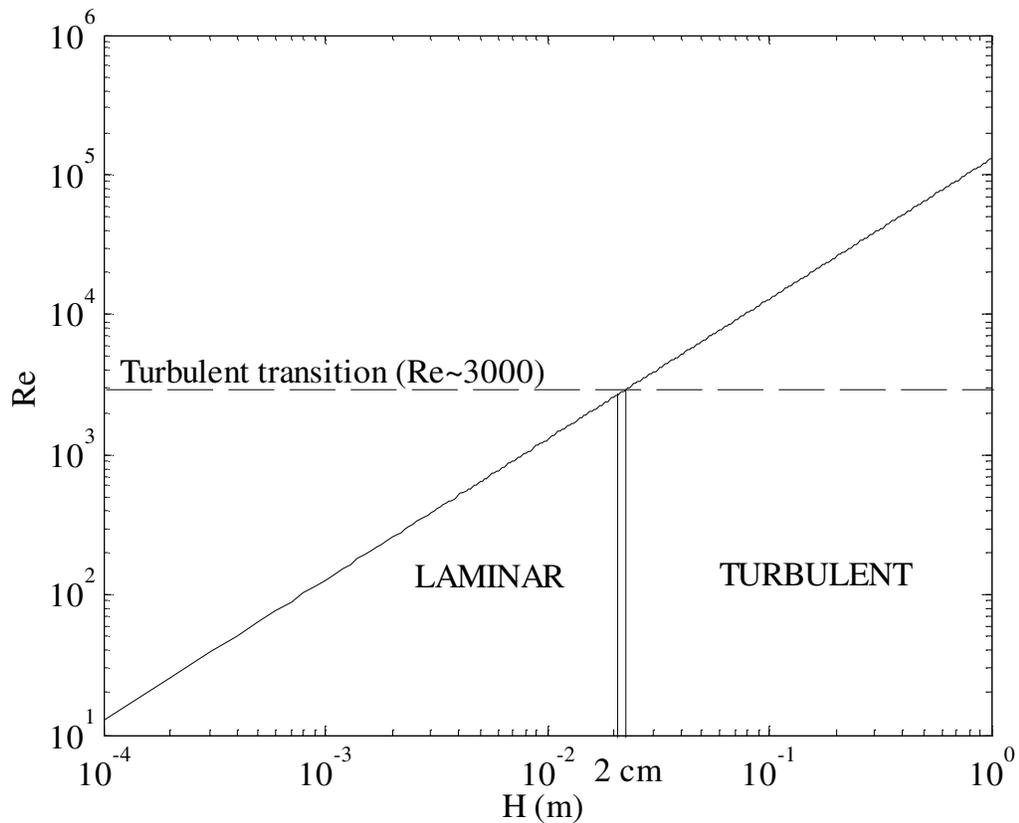
Figure 1-4: Influence of the passage height on the Reynolds number for a 1 m/s flow of air between two parallel plates at 300K.

1.3. Previous Work

1.3.1. Modeling

The problem of the effect of the presence of a structure in close proximity to a flame has been addressed by many researchers. One of the first was Zeldovich[5] in 1941. He studied the propagation of flames in a series of circular tubes and showed that there was a minimum value for the radius of the tube below which the flame was unable to propagate. He introduced the concept of thermal quenching to explain this

observation of a minimum tube size for flame propagation. It was based on the idea that if the heat loss to the environment is larger than the heat generated by combustion, the combustion cannot continue and therefore the flame cannot propagate.

In 1956, Spalding[6] developed an analytical theory to explain Zeldovich's observations. He considered the problem of a flame propagating non-adiabatically, with heat loss to the environment accounted for using a single (fixed) loss term in the gas-phase energy equation. One of the most important results of his analysis was the fact that two flame speeds are associated with the reactive mixture. The lower one is unstable and the higher one is always less than the freely propagating flame speed. As the magnitude of heat loss increases, the stable and unstable flame speeds approach each other and eventually coincide at the inflammability limit of the mixture. While Spalding's model was simplistic, the results and behaviors which he predicted are qualitatively consistent with modern experimental measurements in micro-combustors. Nevertheless, an improved theory is required that accounts for heat exchange within the combustor structure and the scale and geometry dependencies of the heat loss term.

While the thermal interaction between flame and structure can result in heat loss to the environment thereby lowering the flame speed of the mixture and degrading combustor perfomance, it can also be beneficial by providing an additional path for heat transfer from post-flame to pre-flame via the structure. This concept was first recognized and investigated by Weinberg[7] who introduced the term "heat recirculating burner" to describe the latter situation. Weinberg's work was subsequently followed by Takeno[8], who performed detailed theoretical and

experimental studies of the effect of heat recirculation. One of his important observations was that heat recirculation could result in gas temperatures that are higher than the adiabatic flame temperature. These have been termed "excess enthalpy" flames and the porous media burners that produce them are often called excess enthalpy burners.

More recently, researchers have investigated the influence of thermal exchange in the structure on the thermodynamic performance of miniaturized power systems. In 1998, Peterson[9] identified the minimum sizes for MEMS-based regenerative heat engines from a purely thermodynamic viewpoint. Using models for conduction within the structure of a generic Stirling engine and the heat loss to the environment, he was able to determine the efficiency of the heat engine as a function of the cycle temperature ratio, regenerator effectiveness and a non-dimensional "conduction parameter" that represented the ratio of heat lost to the environment via conduction through the structure to the heat released by combustion in the engine. He showed that as the conduction parameter increases, the size of the heat engine would need to increase in order to achieve a "reasonable" level of efficiency. The net result was that for given thermal properties of the structure of a combustor, a heat engine needs to have a certain minimum size to achieve acceptable operating efficiency. However, he did not incorporate any type of model for the combustion process and he neglected thermal exchange in the gas.

Aichlmayer[10] performed a more detailed investigation that included more realistic thermal coupling between the gas and the structure. He did so in the context of a miniature free-piston Homogeneous Charge Compression-Ignition (HCCI) engine where a premixed fuel-air mixture is compressed until ignition. HCCI engines differ

from diesel engines in that the fuel and air are premixed before entering the cylinder. They differ from spark-ignited engines because the mixture auto-ignites under compression and therefore requires no spark. In an HCCI engine, the mixture burns rapidly and homogeneously throughout the combustor volume. As a result, one would expect wall quenching to be less important than in regular engines and that HCCI engines would be a very advantageous operating mode for micro-combustors. Aichlmayer's calculation included full chemistry and also showed that there is a minimum size for HCCI engines that arises from the heat transfer to the structure. Reducing the aspect ratio of the engine improved efficiency by reducing the surface-to-volume ratio and consequently heat loss to the environment. However his model did not incorporate the effect of thermal exchange (i.e. conduction) within the structure itself.

In 2002[11], Daou and Matalon investigated combustion in a 2-D rectangular channel with fully developed Poiseuille flow and heat loss to the walls occurring perpendicularly to the flow direction. They focused on the effect of the heat loss to the channel walls and the inlet velocity on the flame speed and the burning rate of the fuel. They showed that as the passage height becomes smaller, the burning rate decreases because of heat loss to the walls. They also identified two modes of flame extinction: total extinction in small channels and local extinction at the walls in larger channels. In 2003[12], Daou and Matalon extended their work by studying the detailed structure of the flame. They showed that the wall quenching zone enlarged as heat transfer to the wall increased. However, both works relied on a simplified single step model for the chemical reaction and did not consider any axial (i.e. in the flow direction) conduction within the combustor walls.

In 2004, Ronney[13] developed a model for a "Swiss roll" heat recirculating burner where heat from the post flame region is transferred upstream to pre-heat the incoming reactants using a counter-flow heat exchanger. The combustion process was modeled as a perfectly stirred reactor (PSR). This work showed that heat conduction within the structure of the combustor in the flow direction is a dominating effect at microscale.

Recent work by Ju[14] in 2004 also highlighted the importance of heat conduction in the combustor structure. He extended Spalding's 1D theory to include the effect of heat recirculation within the structure of a micro-combustor in addiction to heat loss to the environment. Like Spalding, Ju observed two distinct flame speeds where the lower one was unstable. However, one major difference was the possibility for the higher flame speed to be in excess of the laminar flame speed due to heat recirculation.

Also in 2004, Vlachos[15] reported results of a 2D numerical simulation showing how axial heat conduction within the structure of a micro-channel can enhance flame stability. The work was motivated by earlier experimental observation of "Thermally Stabilized Combustion" by Churchill[16]. Vlachos also showed that the enhancement in stability is strongly affected by the thermal conductivity of the structure as well as heat loss to the environment. Vlachos showed that there is an optimum value of the structural thermal conductivity that maximizes flame stability with respect to heat loss to the environment.

Relatively little modeling of flows within micro-thrusters has been reported in the open literature where the effect of heat transfer to the thruster structure are incorporated. Levin[17] performed a study of the thermal coupling between reacting gas

11

and structure in such micro-thrusters at low pressure. The 2D gas-phase flow was resolved using DSMC while the structure temperature was computed using a Finite Element Method. Levin's work was motivated by the idea that high temperature flows in microscale systems cause the structure to reach high temperature which could in turns degrade its mechanical strength. Levin's work focused on the transient heating of the structure and how it affects the maximum impulse of micro-thrusters.

Other simulations of flows in micro-nozzles performed by Ketsdever[18] focused on how friction and viscous losses affect performance. This work aimed to determine whether a simple orifice configuration was more efficient than a contoured nozzle at micro-scale. Ketsdever's conclusion was that the nozzle to orifice thrust ratio depends on the Reynolds number and is less than one at low Re. However, nozzle to orifice specific impulse ratio was always greater than one, indicating that contoured nozzles provide better propulsive efficiency.

1.3.2. Experimental work

There has been a relatively large amount of work involving the design and construction of micro-combustors and micro-power systems that has met varying levels of success.

The MIT micro-engine project[19] is the oldest of the combustion based micro-scale power generation projects. The basic idea is to construct a shirt-button size gas turbine engine that could be attached to a lunchbox-size fuel tank (full of JP4) and be used to generate electric power for soldier-bourne navigation and communication gear. After more than ten years of effort, operation of the different elements of the

micro-engine have been demonstrated in isolation. However very substantial challenges remain in order to integrate those elements into a working (and suitably efficient) system. One important outcome of the research on the micro-gas turbine engine combustor was the demonstration that despite the challenges highlighted above, combustion in millimeter-scale silicon-based devices is possible (Mehra[20]). Additional work by Spadaccini[21] characterized the performance of the combustor and showed that catalytic micro-combustion of hydrocarbons was also possible. However, the overall efficiency of the micro-engine combustor is very low (<60% on HC fuels) and this alone could prevent the engine's thermodynamic cycle from closing.

The Swiss-roll combustor discussed previously is also part of an experimental program to develop a compact power system based on catalytic combustion and thermo-electrical generation. The Swiss-roll geometry minimizes heat loss to the environment while providing the opportunity for super-adiabatic flame temperatures (excess enthalpy) via heat recirculation through the walls of the combustor. The catalyst allows for combustion to be sustained at very low equivalence ratio, thereby limiting structure temperature. The use of a catalyst deposited on the combustor walls also capitalizes on the aforementioned high surface-to-volume typical of micro-combustors. Thermo-electric materials separate the hot and cold sides of the counter current heat exchanger and are used to generate electric power. Preliminary results[22] suggest that the approach is viable.

Another interesting approach is that taken by Masel's group at UIUC. The focus of this work[23] is on surface treatment and how it can enable combustion in very small

channels by preventing processes associated with flame quenching such as radical recombination at the wall. The results obtained demonstrate the possibility of sub-millimeter combustion and suggest the importance of surface properties and preparation on the design of efficient micro-combustors.

The first MEMS bi-propellant micro-thruster was developed by London[24] at MIT, in 2000. The performance of the thruster was surprisingly good despite the very small scale of the thruster in the transverse direction (Thrust~1N, I_{sp}~180s). Pressure losses through the device were smaller than expected because of the non-continuum effects (i.e. velocity slip at the wall).

Hitt's group[25] at the University of Vermont has demonstrated a MEMS-based H_2O_2 thruster. Hydrogen peroxide was injected in a sub-millimeter scale combustion chamber filled with platinum-coated rods. Reaction occurred in the combustion chamber and hot products were expanded through a nozzle. The device produced 500μN of thrust with a specific impulse of up to 180s.

Finally, Ketsdever's group[26] performed an experimental study of the supersonic flow in micro-orifices and nozzles and validated the results obtained during the computational phase of its investigation.

1.4. Objectives and Approach

The review of the literature has shown that axial heat transfer through a micro-combustor's structure has a significant impact on its overall performance and viability as part of a micro-chemical thruster or a compact power system. Therefore, the principal objective of this thesis is to develop a fundamental understanding of the role

of axial heat transfer on the performance of micro-scale combustors for these applications. This is accomplished through a combined program of analytical modeling and numerical simulation that focuses on the propagation of a laminar premixed flame in a rectangular channel where the flame exchanges heat with the structure, heat flows within the structure itself, and heat is lost to the environment. This 'model problem' has the advantage of being simple while at the same time incorporating most of the critical aspects of the problem. As a result, it can represent combustion in a wide range of micro-power systems.

The approach taken is as follows: First, a simple analytical model for flame propagation in a micro-channel is developed in order to gain a basic understanding of the physics that govern the problem and lead to the unusual observations of flame broadening and increased burning velocity at small scales. These results are compared to the predictions of more detailed one-dimensional numerical simulations that include conjugate heat transfer, heat loss to the environment, and multi-step chemistry. Second, the results of these calculations are used to identify the effects of varying the combustor geometry and the degree of heat loss to the environment on the power density and efficiency of a micro-combustor. Third, these results are used to predict how the performance of a micro-chemical thruster varies with its geometry and heat losses to the environment. Fourth, flame stabilization due to axial heat transfer is investigated. Fifth, and finally, the implications of axial heat transfer on the operation and selection of multi-step chemical kinetic mechanisms used to represent the combustion process in micro-channels are discussed.

Chapter 2: The Flame Broadening Phenomenon

2.1. Introduction

The work reported in this chapter focuses the challenge identified in the previous chapter that is associated with flame broadening in micro-combustors. The objective is to identify the basic governing physics of the phenomenon and to use this understanding to make recommendations regarding the design of efficient micro-combustors. To this end, a mechanism is proposed by which flame broadening occurs via the exchange of heat from the post-flame region to the pre-heat region through the structure of the combustor.

A simple analytical model is developed to describe the basic physics of the fluid-structure coupling problem. The derivation of the model employs reasoning similar to that used by Mallard and Le Chatelier to predict the velocity of a freely propagating flame but extends it to include the effect of the thermal exchange within the structure of the combustor. Both adiabatic and non-adiabatic situations are considered. The model is used to understand the basic physics of the problem by predicting the variation of the flame thickness with different the design parameters that characterize the combustor. These include the passage height, the thermal conductivity, the Nusselt number for heat transfer between the reacting flow and the structure, and the heat transfer coefficient between structure and the environment.

The predictions of the analytical model are subsequently compared to those of a more detailed one-dimensional numerical simulation with full chemistry, species diffusion and heat transfer in the structure.

Preliminary work in the area was reported by Leach[27] but significant improvements in the analytical model and numerical simulation, as well as an additional discussion of power density and pressure loss are presented here. Some of the results presented here are in press[28]

2.2. Analytical Model

Mallard and Le Chatelier's thermal model for flame propagation[29] predicts that the laminar flame speed S_L is proportional to the square root of the product of the thermal diffusivity ($k_r / \rho C_p$) of the unburned reactants and the chemical reaction rate RR:

$$S_L = \sqrt{\frac{k_r}{\rho C_p} \frac{T_f - T_i}{T_i - T_0} RR} \qquad (2\text{-}1)$$

T_o, T_i and T_f are respectively the temperatures of the unburned mixture, the temperature at ignition, and the temperature of the post-flame gases. The theory applies to free-burning (i.e. unconfined) laminar flames and is predicated on the notion that the flame speed is set by the rate at which heat diffuses upstream into the unburned mixture. Appendix I provides a theoretical overview of Mallard and Le Chatelier's thermal model for flame propagation, and an explanation of how a thermo-electrical analogy can be used to derive equation (2-1).

2.2.1. Adiabatic theory

The thermal theory of Mallard and Le Chatelier applies to freely propagating flame that does not exchange heat with the combustor structure or the surroundings. These effects are expected to become important when the flame thickness approaches the characteristic size of the combustion chamber as illustrated in figure 2-1. A more complex picture emerges when the theory is extended to include an additional heat exchange path through the structure from the post-flame region upstream to the pre-flame region. This is illustrated in figure 2-2 which shows that two additional heat transfer paths emerge in addition to conduction upstream through the gas – namely through the structure from the post-flame to the pre-flame, and from the structure to the environment. The path from the post-flame to the pre-flame has three elements: a path from the post-flame to the structure, a path through the structure, and a path from the structure to the pre-flame.
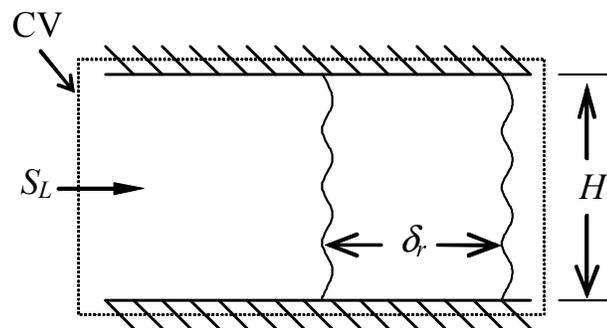
Figure 2-1: Flame stabilized in a passage where $H \sim \delta_r$.
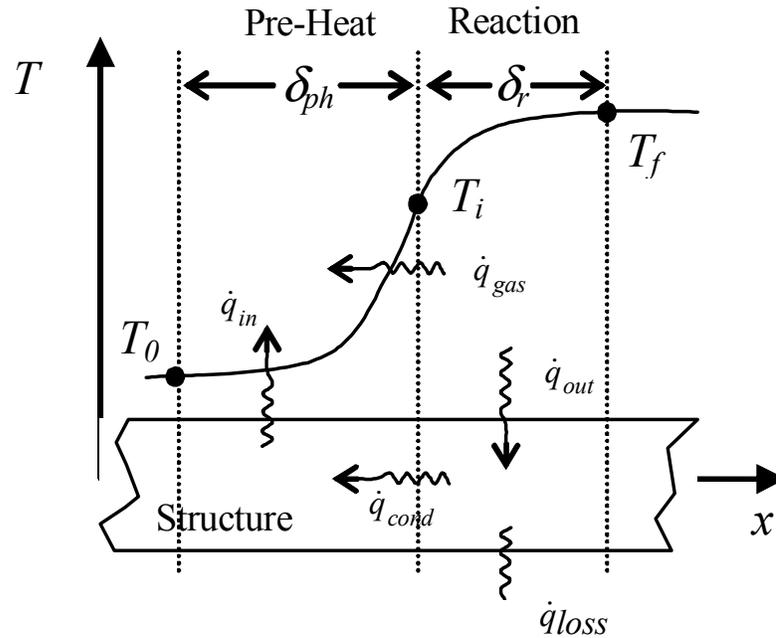
Figure 2-2: Thermal exchange in a flame in close contact with a structure. $\dot{q}_{gas}$ **and** $\dot{q}_{cond}$ **represent the heat conducted from the reaction zone to the pre-heat zone through the gas and through the structure respectively,** $\dot{q}_{out}$ **and** $\dot{q}_{in}$ **represent convective heat transfer between the gas and the structure, and** $\dot{q}_{loss}$ **represents the heat lost to the environment.**

The thermal resistor network of figure 2-3 can be used to visualize the heat exchange between the reaction and the preheat zones as well as the heat loss to the environment. In the figure, $\dot{q}_{gen}$ is the rate of heat generation by the reaction, $\dot{q}_{loss}$ is the rate at which heat is lost to the environment by convective heat transfer from the plates, T_e is the environment temperature, T_s is the structure temperature and T_f is the flame temperature. R_r and R_s are the resistances to conductive heat transfer in the gas

and the structure respectively and R_{bl} is the resistance to convective heat transfer from the gas to the structure. These thermal resistances can be expressed as follows:

$$R_r = \frac{\delta_r}{k_r A_r}, \ R_s = \frac{\delta_r}{k_s A_s}, \ R_{bl} = \frac{2H}{k_r Nu A_{conv}} \tag{2-2}$$

where k_r and k_s are the thermal conductivity of the gas and of the structure respectively, δ_r is the reaction zone thickness, H is the passage height, Nu is the Nusselt number and A_r, A_s and A_{conv} are the cross-sectional surface areas for conduction in the gas and the structure, and for convection between gas and structure respectively. A_{conv} is assumed to be based on the flame thickness δ_r.

Finally, it should be noted that the Mallard and Le Chatelier theory for freely-propagating laminar flames does not include a finite-dimensional pre-heat zone upstream of the reaction zone and so a model for heat transfer in the pre-heat zone is not included in the extension of the theory to micro-combustion. This is not intended, however, to imply that modeling the pre-heat zone is not important. It is simply to say that modeling this mechanism is beyond the scope of the simplified theory for micro-combustors presented here. As we will see, this omission does not prevent the model from producing qualitatively correct results.
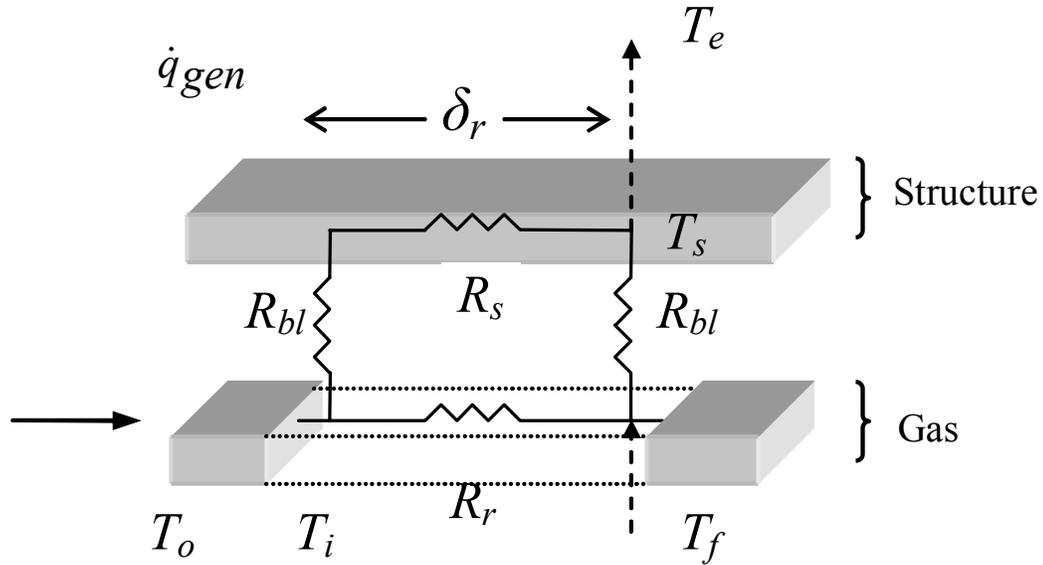
Figure 2-3: Thermal resistor network for visualizing heat exchange between gas and structure and heat loss to the environment. The two parallelepipeds represent streamtubes for heat transfer in the gas and the structure. $\dot{q}_{gen}$ **represents the heat generated by the combustion process,** $\dot{q}_{loss}$ **represents the heat lost to the environment.**

In the adiabatic case (corresponding to a tube that is perfectly insulated from the environment), $\dot{q}_{loss}$ is set to 0. Since the flame temperature is a constant equal to the adiabatic flame temperature, the rate at which heat is generated by the flame ($\dot{q}_{gen}$) does not need to be defined. Applying conservation of energy (the equivalent of Kirchoff's law) to the thermal circuit illustrated in figure 2-3 and assuming that $\delta_r = S_L / RR$ as is done in the Mallard-Le Chatelier theory leads to the following expression for the reaction zone thickness:

$$\delta_r = \sqrt{\beta \frac{k_r}{\rho C_p} \frac{T_f - T_i}{T_i - T_0} \frac{1}{RR}} \qquad (2\text{-}3)$$

Beta (β) is a parameter that accounts for the variation of the overall thermal resistance of the gas-structure combination as a function of the passage height H, the ratio ζ of the cross sectional areas for axial conduction in the structure and the reactant stream-tube $\left(\zeta = \frac{A_s}{A_r} \right)$ and the ratio λ of the thermal conductivity of the structure to that of the reactive mixture $\left(\lambda = \frac{k_s}{k_r} \right)$.

$$\beta = \frac{1 + \zeta \lambda \left(1 + \frac{2H^2}{\delta_r^2} \frac{1}{Nu} \right)}{1 + 2\zeta \lambda \frac{H^2}{\delta_r^2} \frac{1}{Nu}} \qquad (2\text{-}4)$$

Combining equations 2-3 and 2-4 yields a fourth order polynomial equation in δ_r for which four solutions can be found. Of these, only one value of δ_r is real positive and hence physically realistic. For a rectangular channel, $\zeta = \frac{2t}{H}$ where t is the thickness of the combustor wall. Combining equations 2-3 and 2-4 to solve for δ_r results in a fourth order algebraic equation with four possible roots. Only one of these is real and positive and hence physical.

Equations 2-3 and 2-4 indicate that the reaction zone thickness depends on the normalized thermal conductivity of the structure, the area ratio for axial conduction ζ, the passage height H, and the Nusselt number in addition to the usual parameters associated with the Mallard-Le Chatelier theory. While equation 2-3 is an implicit expression for δ_r because β is a function of δ_r, we can check that it has the proper

asymptotic behavior using equations 2-3 and 2-4. At zero Nusselt number or infinite passage height, equation 2-3 indicates that $\beta \rightarrow 1$. Inserting this result into equation 2-4 recovers the traditional formulation in which the reaction zone thickness only depends on the thermal diffusivity of the gas. Conversely, at large Nusselt numbers or small passage heights, equation 2-3 indicates that $\beta \rightarrow 1 + \zeta \lambda$, which is always greater than one. This indicates that the reaction zone thickness increases, leading to flame broadening. At large Nusselt numbers, the thermal resistance between the gas and the structure is small and the transport of heat (and hence the reaction zone length) is determined by the thermal resistance of the structure acting in parallel with the thermal resistance of the gas. As a result, in either the large Nusselt number or the small passage height limits, the reaction zone thickness is determined by the thermal conductivity of the structure and the gas, and the relative areas for axial heat conduction.

Thus, the simple model has shown that a conductive heat transfer conductive structure can increase heat transfer from the reaction zone to the upstream reactants. This can also lead to an increase in burning rate due to faster upstream conduction and pre-heating of the reactants. This is consistent with the effects of pre-heating reactants in laminar flames[30], and the pre-heating mechanism is very similar to that of 'excess enthalpy' burners[31,32] where increases in burning rate are also observed.

2.2.2. Non-adiabatic theory

The effect of heat loss to the environment, an important consideration in micro-combustors because of their large surface/volume ratios, can be incorporated by

adding a heat sink to the thermal network and by recognizing that the chemical reaction acts like a heat (or analogous current) source. In this case, $\dot{q}_{gen}$ is computed by adjusting the rate of heat generation in the adiabatic case $\dot{q}_{ad}$ by a factor that accounts for the effect of an arbitrary flame temperature T_f

$$\dot{q}_{gen} = \dot{q}_{ad} \exp\left(-\frac{E_a}{RT_f} + \frac{E_a}{RT_{f,ad}} \right) \quad\quad\quad (2\text{-}5)$$

In this expression, E_a is the activation energy, R is the gas constant and $T_{f,ad}$ is the adiabatic flame temperature. The value for E_a corresponds to a one-step overall reaction mechanism for stoichiometric H_2-air combustion and was taken from[33]. $\dot{q}_{loss}$ is expressed as a convective heat loss:

$$\dot{q}_{loss} = h_{Te} A_{loss} \left(T_s - T_e \right) \quad\quad\quad (2\text{-}6)$$

where $h_{T,e}$ is the coefficient for heat transfer from the plates to the environment and A_{loss} is the surface area for convective heat loss. Since heat loss occurs mainly in the region where the gas temperature is high, the area for heat loss is assumed to correspond to a length equal to the flame thickness. The heat transferred from the reaction zone to the preheat zone is written as the difference between the heat generated by the reaction and the heat lost to the environment:

$$\dot{q} = \dot{q}_{gen} - \dot{q}_{loss} \quad\quad\quad (2\text{-}7)$$

The value of $\dot{q}$ obtained using equation 2-7 is used to compute an 'effective' flame temperature which includes the effect of heat loss.

$$T_f = T_i + \dot{q} R_{eff} \qu\quad\quad\quad (2\text{-}8)$$

In this expression, T_i is the ignition temperature and R_{eff} is the effective thermal resistance of the thermal network defined as:

$$R_{eff}^{-1} = R_r^{-1} + (R_s + 2R_{bl})^{-1} \qquad (2\text{-}9)$$

Balancing the heat fluxes through the boundary layer, structure, and to the environment leads to the following expression for the peak temperature of the structure T_s:

$$T_s = T_i + (T_f - T_i)\frac{R_s + R_{bl}}{R_s + 2\,R_{bl}} - \dot{q}_{loss}\frac{R_r(R_s + R_{bl})}{R_r + R_s + R_{bl}} \qquad (2\text{-}10)$$

As before, performing a thermal balance on the entire network gives an expression for the flame thickness:

$$\delta_r = \frac{\dot{q}}{\rho\,C_p\,(T_i - T_0)\,RR} \qquad (2\text{-}11)$$

The reaction rate in equation 2-11 is the adiabatic reaction rate adjusted by a factor accounting for the 'effective' flame temperature T_f

$$RR = RR_{ad}\,\exp\left(-\frac{E_a}{RT_f} + \frac{E_a}{RT_{f,ad}}\right) \qquad (2\text{-}12)$$

The system of equations {2-5 - 2-12} can be solved using an iterative procedure and an initial guess that corresponds to the adiabatic case:

$$\begin{cases} T_f = T_{f,ad} \\ \dot{q} = \dot{q}_{ad} \end{cases} \qquad (2\text{-}13)$$

2.3. Numerical Model

A transient 1-D model developed by Zhu and Jackson for studying the performance of catalytic reactors is adapted to study the behavior of a flame stabilized in a channel. A complete description of the code may be found in[34] and only an abbreviated description is presented here. For the numerical model in this study, all surface chemistry is excluded from the calculations and as such there is no mass exchange between the surface and the gas phase. Further, the pressure in the channel flow is assumed constant, which implies that the momentum equation is neglected entirely and velocity is calculated from mass conservation. While this is appropriate for the purposes of comparison with the analytical model, the pressure drop in micro-channels can be a significant performance parameter because of its impact on the efficiency of thermodynamic cycles. In this case, however, we are interested in minimum size combustors with lengths on the order of the flame thickness. As a result, pressure losses are not expected to be significant. This will be further discussed in the "Results and Discussion" part of this chapter.

The numerical model divides the channel into axial cells and solves for the following variables in each cell: ρ, u, T, T_s, and Y_k where Y_k is the vector of mass fractions for the species in the gas phase. The governing equations in each cell for these variables include the following:

- Ideal gas law:

$$\rho = \frac{PW_m}{RT} \tag{2-14}$$

- Conservation of mass:

$$\frac{\partial(\rho u)}{\partial x} = 0 \qquad (2\text{-}15)$$

- Conservation of energy in the gas-phase:

$$\rho C_P \frac{\partial T}{\partial t} = -\rho u \frac{\partial\left(\sum_k (h_k Y_k)\right)}{\partial x} + \frac{\partial}{\partial x}\left(k_r\left(\frac{\partial T}{\partial x}\right)\right) - a_{ch} h_T (T - T_s) - \sum_k (W_k h_k \dot{\omega}_k) \quad (2\text{-}16)$$

- Conservation of species in the gas-phase:

$$\rho \frac{\partial Y_k}{\partial t} = \frac{\partial}{\partial x}\left(\rho D_k \frac{\partial Y_k}{\partial x}\right) - \rho u \frac{\partial Y_k}{\partial x} + W_k \dot{\omega}_k \qquad (2\text{-}17)$$

- Conservation of energy in the solid structure:

$$\rho_s C_{P,s} \frac{\partial T_s}{\partial t} = \frac{\partial}{\partial x}\left(k_s\left(\frac{\partial T_s}{\partial x}\right)\right) + a_s h_T (T - T_s) - a_{s,e} h_{T,e} (T_s - T_e) \qquad (2\text{-}18)$$

In the above equations, W_m is the mean molecular weight of the gas flow, $\dot{\omega}_k$ is the production rate of the kth species in the gas phase. a_{ch} represents the internal structural surface area per unit gas phase flow volume, and a_s and $a_{s,e}$ represent the internal and external structural surface area per unit structure volume respectively. Since we consider a parallel plate geometry these last parameters simplify to $a_{ch}=2/H$ and $a_s= a_{s,e} = 1/t$.

For the numerical model, a 9-species, 19-reaction mechanism[35] for H_2-air combustion is employed. Table 4 in Appendix II shows the reactions considered in the mechanism. Properties for the gas-phase species varied with temperature and were computed based on fitted polynomials (h_k and C_P) and on kinetic theory

approximations (k_r and D_k). The properties for the solid structure (ρ_s, C_{Ps} and k_s) did not vary with temperature in the numerical model.

The boundary conditions for equations 2-15 – 2-18 in the numerical model are as follows:

- at the inlet ($x = x_{in,}$):

$$\begin{cases} u = u_{in} \\ Y_k = Y_{k,in} \\ \rho u \overline{C}_P (T - T_{in}) = \zeta\, h_{T,in} (T_s - T) \\ h_{T,in} (T_s - T) = k_s \left(\dfrac{\partial T_s}{\partial x} \right) \end{cases} \qquad (2\text{-}19)$$

- and at the oulet ($x = x_{out,}$):

$$\begin{cases} \dfrac{\partial Y_k}{\partial x} = 0 \\ \dfrac{\partial T}{\partial x} = 0 \\ \dfrac{\partial T_s}{\partial x} = 0 \end{cases} \qquad (2\text{-}20)$$

For the inlet boundary at $x = x_{in}$, $h_{T,in}$ represents the effective heat transfer coefficient to the upstream portion of the gas flow, and for the current study $h_{T,in} = 0$ such that $T = T_{in}$ for the first cell boundary. For all runs in the current study, $T_{in} = 300$ K, and $Y_{k,in}$ are set for a H_2-air mixture with $\Phi = 1.0$. Pressure was held constant at 1.0 atm for all simulations. The value for u_{in} is determined during a model run as discussed below to ensure that the flame stabilization occurred away from the reactor inlet and thereby flame thicknesses were found independent of the inlet boundary conditions.

T_o

$h_{env}=1$ W/m^{2}K

U, P, T_o

d_r

Nu

t

$\varsigma =2t/H=1$

H

l

Computational grid
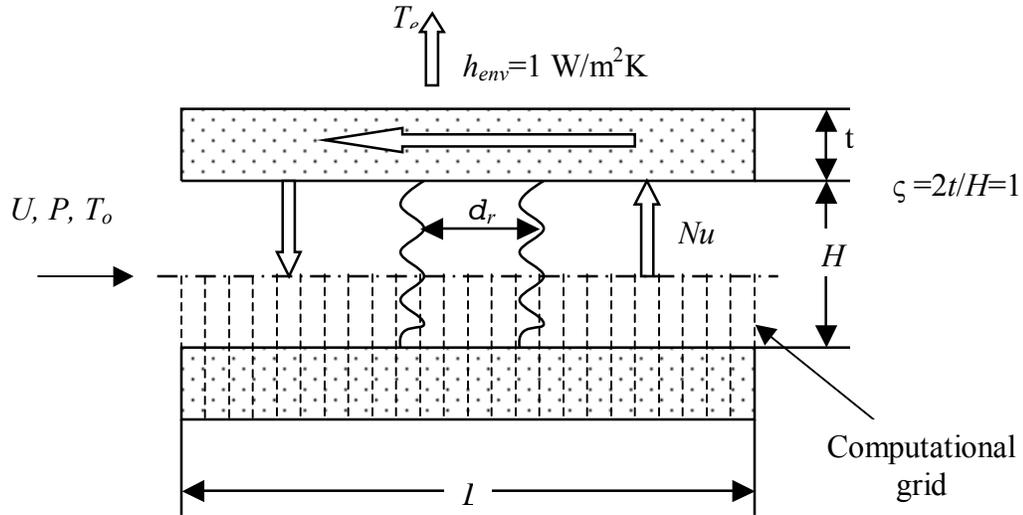
Figure 2-4: Schematic diagram of a flame stabilized in a micro-channel showing heat exchange between the reacting fluid and the structure, axial heat exchange through the structure, and heat loss to the environment. The computational grid is superimposed on the lower half of the domain.

A discretized version of equations {2-14 – 2-18} is solved simultaneously on an evenly spaced grid consisting of 201 elements with a domain length of 1.0 cm and the boundary conditions shown in equations 2-19 – 2-20. Adequate grid resolution has been verified by doubling the number of grid points and finding that flame thicknesses did not change from the 201-cell simulation. The 1.0 cm computational domain was sufficient to contain the reaction zone for all runs presented here. The code uses the method of lines to implement an adaptive time step. The convective terms are discretized using a Godunov-type upwind finite volume method while a

central difference method was used to discretize the diffusive terms. The resulting set of discrete equations was integrated using the stiff PDE solver LIMEX[36].

The numerical solution depends strongly on user-specified parameters including H, Nu, k_s and $h_{T,e}$, and for a given combination of user-defined parameters, the necessary u_{in} ($\approx S_L$) to stabilize the flame in the domain away from the inlet boundary is unknown. Conventional flame models have used the approach of solving the steady-state version of equations {2-14 – 2-18}, fixing a temperature within the computational domain, and solving for ρu as an eigenvalue for the system[37]. However, in the current study, it is desired to model conditions when the flame undergoes extinction, and thus rather than anchoring the flame with a fixed temperature in the mesh, an alternative approach based on the transient integration of equations {2-14 – 2-18} is implemented. An initial condition is set with T and T_s = 1000 K throughout the domain except the first gas point of the domain where T =300 K. The high initial values of T and T_s in the rest of the domain ensure that the flow 'lights'. The inlet velocity u_{in} is set to a value below the expected S_L. A steady solution is found typically after 10 s of transient integration and the flame is anchored at the inlet of the reactor. u_{in} is then increased by 0.1% and the solution is recalculated. This process is repeated until the induction zone length (based on the decay of the O_2 mass fraction in the flame zone) equals that calculated for the freely propagating flame. The value for the laminar flame speed associated with a freely propagating flame was found in[38] and equaled 2.1 m/s at the equivalence ratio considered here. At the final u_{in}, the integration continues for 100 s to ensure that the

final solution is at a steady-state condition for both the solid and gas phases and that the flame position is fixed in relation to the walls.

Upon determining the final solution at a value of u_{in} that provides a reaction zone away from the inlet, the flame thickness can be determined. The definition of flame thickness proposed by Sung and Law[39] is used where the flame thickness is the ratio of the total temperature difference to the maximum value of the temperature derivative:

$$\delta_r = \frac{T_f - T_0}{\left(\dfrac{dT}{dx}\right)_{max}} \qquad (1\text{-}21)$$

For H_2-air mixtures with $\Phi = 1.0$ and $T_0 = 300$ K, the flame thickness for a freely propagating flame computed using equation 1-21 is 0.42 mm and is consistent with values reported elsewhere[40]. For the same flame, the total temperature change across the flame is $T_f - T_0 = 2036$ K. This is 61 K lower than the difference associated with complete combustion by an adiabatic flame. This reduced temperature difference is the result of dissociation.

2.4. Results and Discussion

2.4.1. Adiabatic results

Figure 2-4 is a plot of the non-dimensional flame broadening (i.e. the ratio of the reaction zone of thickness δ_r to the reaction zone thickness associated with a freely propagating flame in the absence of the structure $\delta_{r,fr}$) as a function of the normalized passage height $H/\delta_{r,fr}$ for four values of Nu under adiabatic structure conditions (i.e.,

$h_{T,e} = 0$). The value of $\delta_{r,fr}$ found using the numerical simulation is 0.42 mm. The Nusselt number is a constant for fully-developed flows that depends on the geometry of the flow passage. Therefore, curves corresponding to different values of the Nusselt number are included to illustrate the effects of changing the thermal coupling between the gas and the structure by changing the flow geometry.
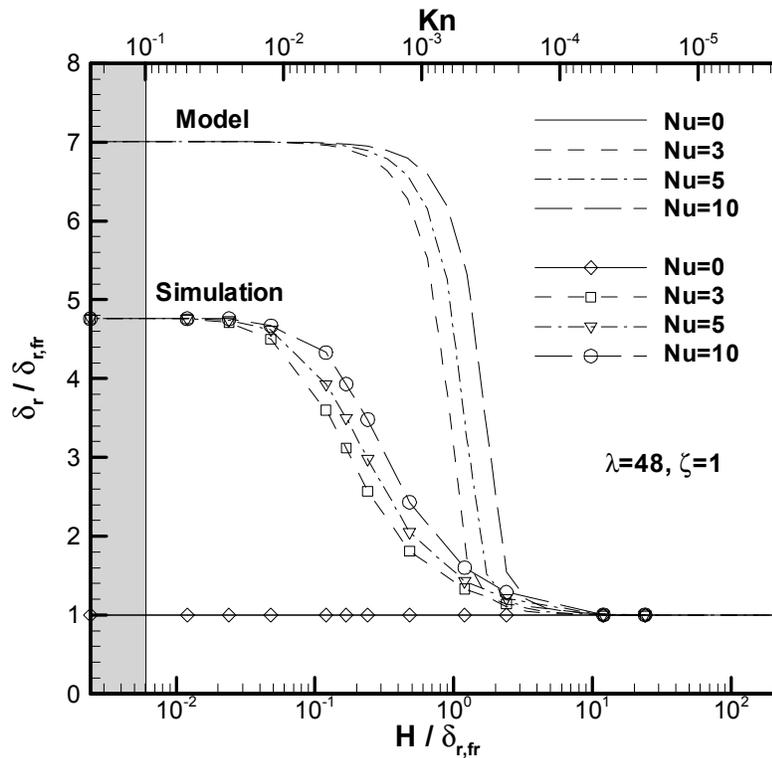
Figure 2-5: Fractional increase in reaction zone length δ_r as a function of the normalized flow passage height $H/\delta_{r,fr}$ for a range of Nusselt numbers. The lines without symbols correspond to the analytical model and the lines with symbols correspond to results from the numerical simulations. The predictions of the simulation and model are no longer valid in the shaded region because the Knudsen number is greater than 0.1.

The lines without symbols correspond to the simple analytical model while the dotted lines with symbols correspond to the numerical simulations. The analytical and numerical models have good *qualitative* agreement as both indicate that δ_r undergoes a limit cycle behavior with variations in H. At large H, $\delta_r/\delta_{r,fr} = 1$ and δ_r is determined by k_r (~0.2 W/mK). As H decreases, δ_r becomes more strongly influenced by the structure thermal conductivity k_s (10 W/mK). In both models, the strength of the thermal coupling between the fluid and the structure (determined in part by Nu) determines at what H the transition from gas to structure-dominated heat transfer occurs. The transition begins to occur as H decreases below $10\delta_{r,fr}$ (~ 5 mm) and the broadening has reached its maximum limit when $H < 0.01\delta_{r,fr}$ the unconfined flame thickness. Many factors contribute to the discrepancy in the amplitude of the broadening predicted by the numerical and analytical models. Some important differences include the use of multi-step versus single step chemistry, variable versus fixed gas-phase properties, and the use of discrete versus distributed heat transfer between the gas and the structure. Considering these major differences, the correspondence between the model and simulation is quite remarkable and indicates that the model captures the dominant aspects of the governing physics.

The results also show that inclusion of heat transfer through the structure leads to an important difference in how the burning velocity is related to the axial temperature gradient in freely propagating flames versus those stabilized in micro-channels. Both the original theory of Mallard and Le Chatelier and the theory for microchannels presented here are predicated on the notion that in order for a flame to propagate, heat

from the post-flame must be transferred upstream to heat the incoming reactants to the ignition temperature. Therefore, increasing the velocity of the reactants in both theories requires an increase in the heat flux from the post-flame to the pre-flame. In the original theory of Mallard and Le Chatelier, the only mechanism for accomplishing this is to increase the strength of the temperature gradient through the flame by decreasing the flame thickness. Thus, in freely-propagating flames, the burning velocity must be inversely related to the flame thickness. In micro-channels, however, an additional heat transfer path through the structure is available. This has two consequences: First, the presence of the second path takes some of the load off axial conduction in the gas. This means that less heat needs to be transferred through this path and the temperature gradient through the flame does not have to be as steep. This, in turn, means that the reaction zone can be longer. Second, the heat transfer through the structure increases with increasing contact area with the gas. Since the contact area increases with increasing reaction zone thickness, another mechanism for increasing heat transfer upstream is to increase the reaction zone thickness. Therefore for a flame stabilized in a micro-channel, the burning velocity is directly related to the flame thickness.

Finally, it is important to note that some of the data points in the left portion of figure 2-4 correspond to passage heights that are so small that the continuum hypothesis, and thus our numerical representation of the reacting fluid, may no longer apply. These sections have been shaded gray in this figure and the ones that follow. The model and simulation results are only projected into these areas to illustrate the complete limit-cycle behavior. The common metric for identifying length scales

where non-continuum effects become important is the Knudsen number. It is defined as the ratio of the mean free path λ of a gas molecule to the characteristic length scale of the device. In this work, the characteristic length scale is the passage height so:

$$Kn = \frac{\lambda}{H} \tag{2-22}$$

Table 1 summarizes the commonly accepted boundaries for the different flow regimes as a function of the Knudsen number[41].

Flow Regimes

$Kn < 0.01$	Continuum
$0.01 < Kn < 0.1$	Slip
$0.1 < Kn < 10$	Transitional
$10 < Kn$	Free Molecular

Table 1: Flow regimes associated with different Knudsen number ranges from[42]

The secondary x-axis on figure 2-4 shows that the smallest passage heights fall into the slip regime. While this is not necessarily a problem because the Navier-Stokes equations are valid through the entire slip regime[43], slip boundary conditions should be applied in the slip regime to account for possible discontinuities in velocity and temperature at the wall. Since the momentum equation is neglected in this work,

the only discontinuity that needs to be accounted for is the gas temperature at the wall. A fit to results of direct simulation Monte Carlo calculations for fully developed flow between infinite parallel plates[44] shows that the Nusselt number varies with Knudsen number as follows:

$$Nu = 7.86e^{-3.86Kn} \tag{2-23}$$

Figure 2-5 compares predictions of flame broadening made assuming the Nusselt number is constant (7.86, the value associated with fully developed continuum flow between parallel plates) to those made using equation 2-23. It shows that the near-wall temperature discontinuity in the slip regime has a negligible impact on the broadening phenomenon. Therefore, it does not appear that including this effect is particularly important for predicting the performance of micro-combustors. Furthermore, the smallest dimensions shown in figure 2-5 are probably not very realistic for practical devices. Instead, the lower size limit will most-likely be set by heat loss from the structure to the environment. This will be discussed later.
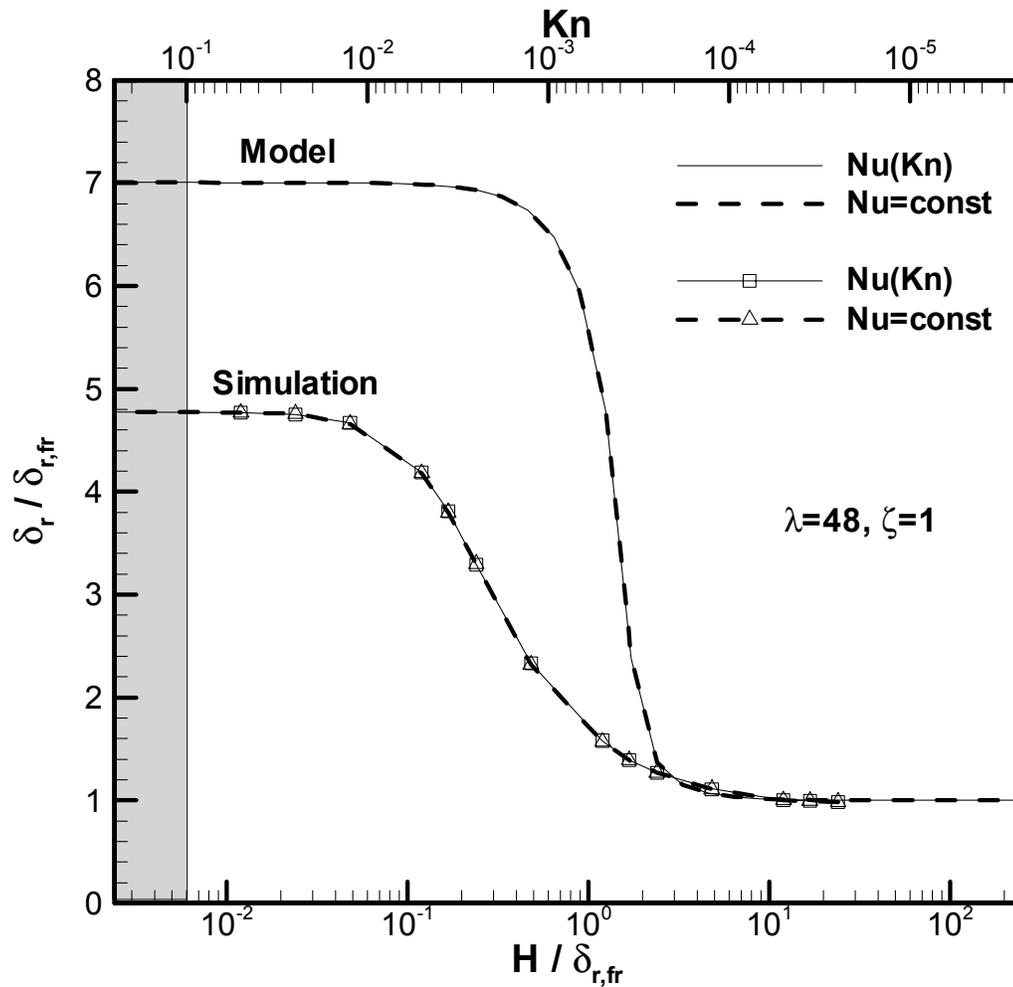
Figure 2-5: Comparison of the fractional increase in reaction zone length $\mathbf{d_r}$ as a function of the normalized flow passage height $H/\mathbf{d_{r,fr}}$ when temperature slip at the wall is and is not included. The lines without symbols correspond to the analytical model and the lines with symbols correspond to the numerical simulations. The solid lines show the results when temperature slip is included while the dashed lines correspond to a fixed Nusselt number of 7.86 corresponding to fully-developed flow between two parallel plates.

Figure 2-6 compares analytical and numerical predictions of the non-dimensional flame broadening $\delta_r/\delta_{r,fr}$ for flow between infinite parallel plates as a function of the normalized passage height $H/\delta_{r,fr}$ for three values of k_s. The change in Nusselt number with Knudsen number is included in this and all subsequent figures. Both the model and the simulation show that the broadening depends on k_s. Increasing k_s increases the heat transfer rate through the structure, which thereby reduces the necessary heat transfer rate through the gas phase. This enables the temperature gradient through the gas to be shallower and allows the reaction zone thickness to be longer than that required for a freely propagating flame. While both models show that the passage height corresponding to the transition from gas to structure-dominated thermal exchange does not depend strongly on k_s, the amplitude of the broadening phenomenon appears to be a stronger function of the thermal conductivity of the structure in the analytical model than in the numerical model.
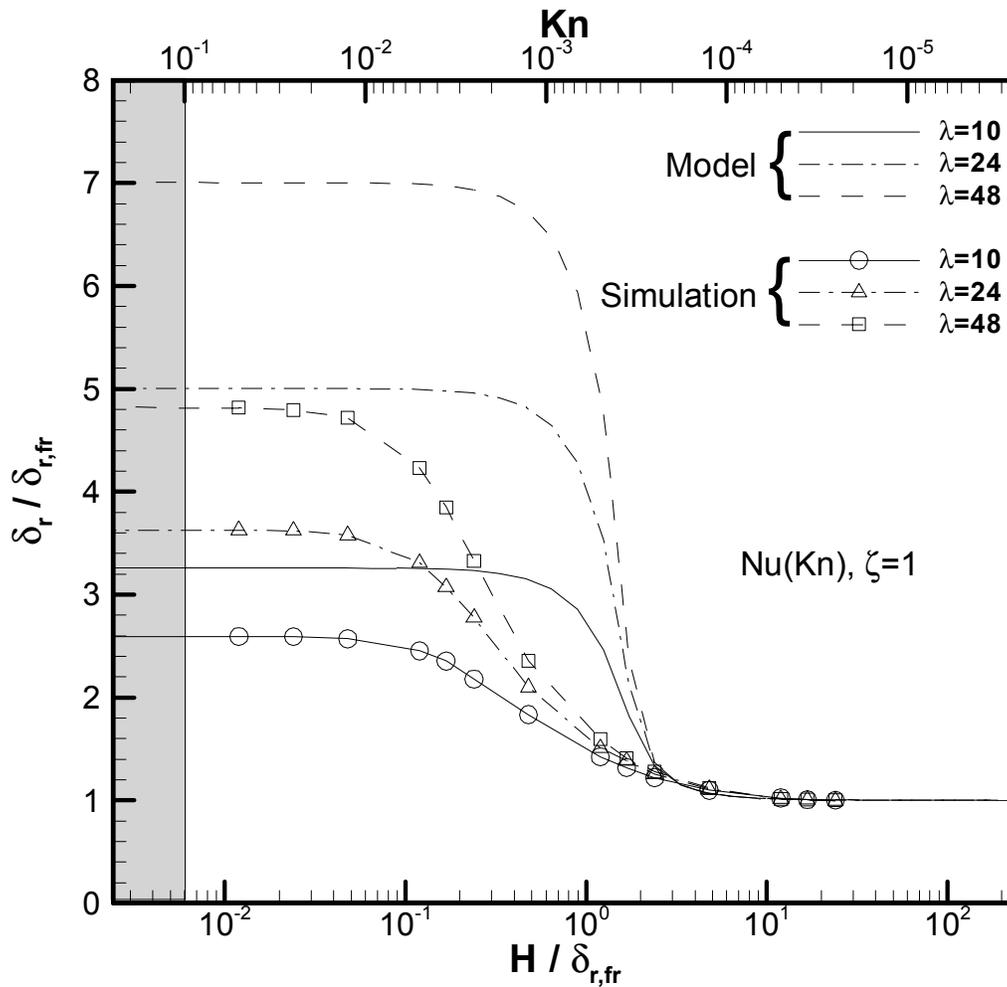
Figure 2-6: Fractional increase in reaction zone length δ_r as a function of the normalized flow passage height $H/\delta_{r,fr}$ for a range of normalized structure thermal conductivities λ. Lines without symbols correspond to the analytical model and the lines with symbols correspond to numerical model results and k_r=0.21 W/mK.

So far, the ratio of the cross-sectional areas for axial conduction of the structure to that of the gas has been help constant as the passage height is varied. However,

increasing the relative thickness of the structure compared to the gas will allow more heat to be conducted through the structure in the same way than increasing structure's thermal conductivity would. Therefore, the truly important parameter is the structure's conductance which is defined as $\lambda\zeta$. Figure 2-7 shows the effect of the structure's conductance on the flame broadening phenomenon for three values of $H/\delta_{r,fr}$. Both the analytical model and numerical simulation indicate that the increase in the reaction zone thickness approaches a limit with increasing conductance of the structure. This limit depends on Nu as well as H. For a highly conductive structure, the resistance to heat transfer at the gas/structure interface limits flame broadening. The magnitude of broadening predicted at the high structure conductance limit by the analytical model is approximately 50% larger than that predicted by the numerical simulation, but both show similar limit cycles.
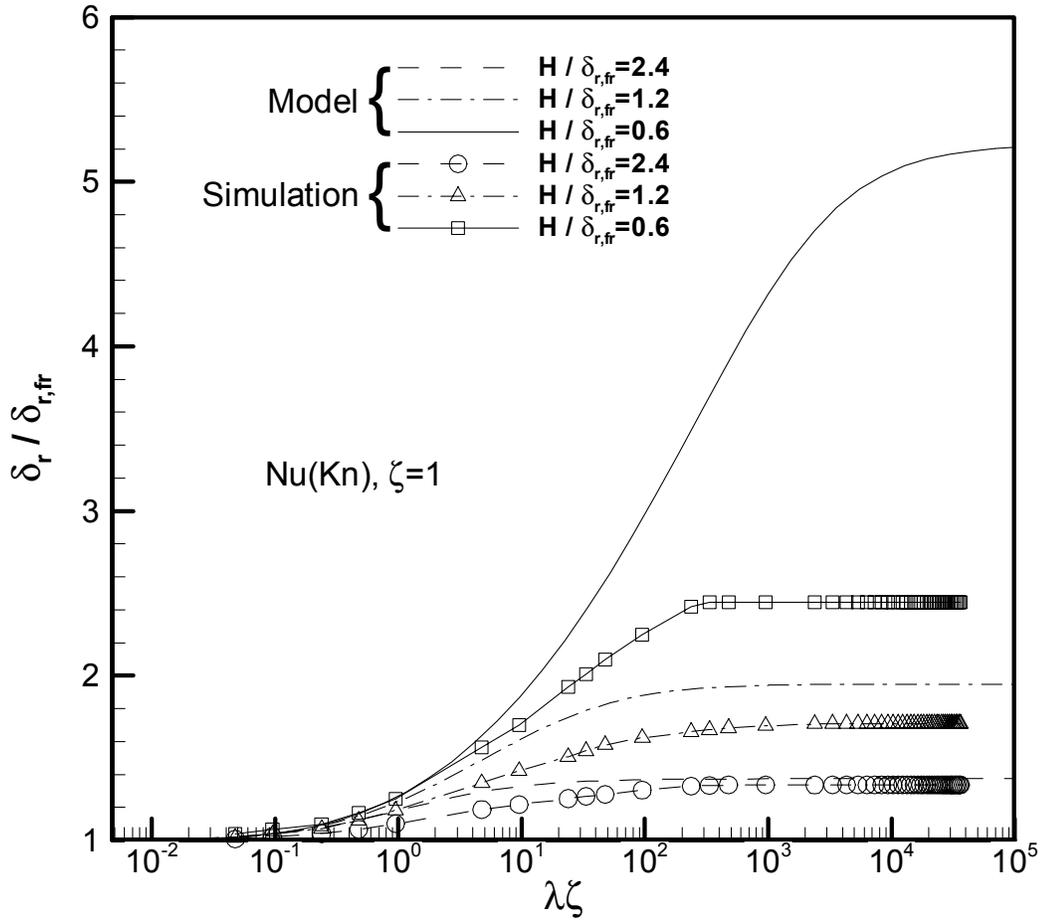
Figure 2-7: Fractional increase in reaction zone length δ_r as a function of non-dimensional thermal conductance ($\lambda\zeta$) of the structure for a range of normalized passage heights. $\delta_{r,fr}$ is the reaction zone length associated with a freely propagating flame, $\zeta=1$, $Nu=3$, and $k_r=0.21$ W/mK. Lines without symbols correspond to the analytical model and lines with symbols correspond to numerical model results.

So far, we have assumed that the combustor is adiabatic and that no heat is lost from the structure to the environment. The results for the adiabatic structure cases in figures 2-5 – 2-7 indicate that conduction of heat from the post-flame through the structure to the upstream preheat zone can broaden the reaction zone by a factor of 4 or more. The results also show that the thermal resistance between the gas flow and the structure limits heat transfer upstream and in turn limits the magnitude of the broadening phenomenon.

2.4.2. Non-adiabatic results

Heat loss from the structure to the environment is also important in micro-scale combustors because it dissipates energy that could be used to pre-heat the reactant mixture and can also lead to flame quenching. Figure 2-8 shows the non-dimensional flame broadening as a function of the normalized passage height for three values of $h_{T,e}$ for both the analytical model and the numerical simulation. For $h_{T,e}$ of $O(10)$ or less, reaction zone broadening arises as before, but as H decreases the heat loss to the environment eventually leads to a reduction in the flame zone thickness followed by extinction. Extinction occurs when the surface to volume ratio of the micro-channel becomes so large that heat loss to the environment prevents sufficient thermal feedback to the preheat zone to sustain continuous ignition of the flame. As $h_{T,e}$ increases to large values, the broadening phenomenon is replaced by a rapid reduction of the flame thickness with decreasing H and flame extinction occurs at relatively large H. The reduction in reaction zone thickness with decreasing H for structures with large thermal losses arises because steeper temperature gradients in the gas and

43

structure must be sustained in order to transfer an adequate fraction of the reaction heat release back to the preheat zone. These results suggest that the ability to prevent heat loss to the environment sets one limit on the minimum size of a micro-combustor. Finally, it is important to note that the heat transfer coefficient has been varied over an extremely wide range in figure 2-8 in order to illustrate what happens when heat loss to the environment is relatively weak and relatively strong. It would probably be quite difficult to achieve a heat transfer coefficient of 10 W/m²K or smaller in a practical device.
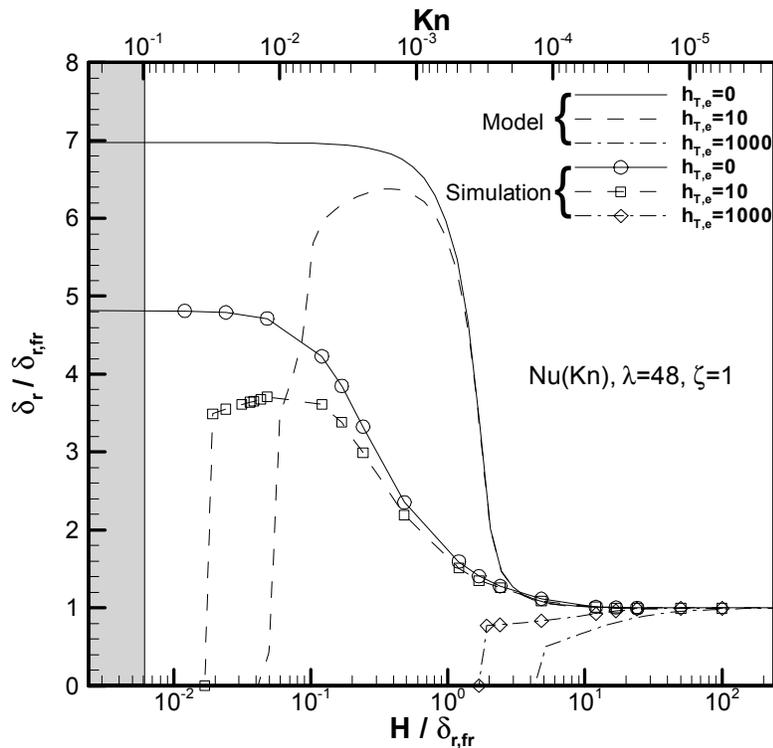
Figure 2-8: Fractional increase in reaction zone length δ_r as a function of the normalized flow passage height $H/\delta_{r,fr}$ for a range of heat transfer coefficients in W/m²K. Lines without symbols correspond to the analytical model and the lines with symbols correspond to numerical model results.

While the qualitative agreement between the analytical and numerical models lends credence to the principles underlying the modified Mallard-Le Chatelier theory, the quantitative discrepancy between the analytical model and numerical simulation is hardly surprising. As indicated earlier, the discrepancy can arise from numerous factors including the implementation of variable properties and multi-step chemistry in the numerical model. In addition, the single-step chemistry of the analytical model assumes that the reaction goes to completion while the multi-step chemistry of the analytical model accounts for dissociation and the accompanying reduction in flame temperature. Finally, the numerical model distributes the heat feedback from the structure throughout the reaction and preheat regions. This reduces to some extent the impact of the structural heat feedback in comparison to the analytical model which sends all of the heat transferred to the structure in the post-flame back to the preheat zone. Accordingly, the numerical model is less sensitive to changes in passage height, structure thermal conductivity, and Nusselt number than the analytical model.

2.4.3. Preliminary implications on power density

While the broadening phenomenon is of interest theoretically, it also has very practical implications on the development of high power density combustors. For the purpose of this work, the power density is defined as follows:

$$\dot{w}_D = \frac{\dot{W}}{V} \tag{2-22}$$

where $\dot{W}$ is the power generated by the combustion process and V is the volume of the combustor in which the chemical energy is released. We have already shown that thermal exchange with the structure increases the reaction zone thickness and this observation along with equation 2-22 indicates that the overall power density of the combustor might decrease as the size of the combustor is reduced. This, of course, would run counter to the objective of miniaturizing combustors in the first place, which is to increase power density. At the same time, however, we have already shown that the increased heat feedback from the structure to the preheat zone results in a substantial increase in the allowable burning velocity so the net effect is not clear.

The relative increase in the non-dimensional burning velocity and the non-dimensional flame thickness determined using the numerical model is illustrated in figure 2-9. It is important to note that the simple model predicts that the power density should remain constant as the passage height is varied because changes in flame speed are directly related to changes in flame thickness (since $\delta_r = S_L/RR$ is assumed). The results from the numerical model presented in figure 2-9, however, show that the evolution of those parameters is slightly different in both the amplitude of the increase and the passage height H corresponding to the transition point from a thin to a thick flame. This discrepancy can again be attributed to the mismatch in complexity between the simple analytical model and the numerical simulation.
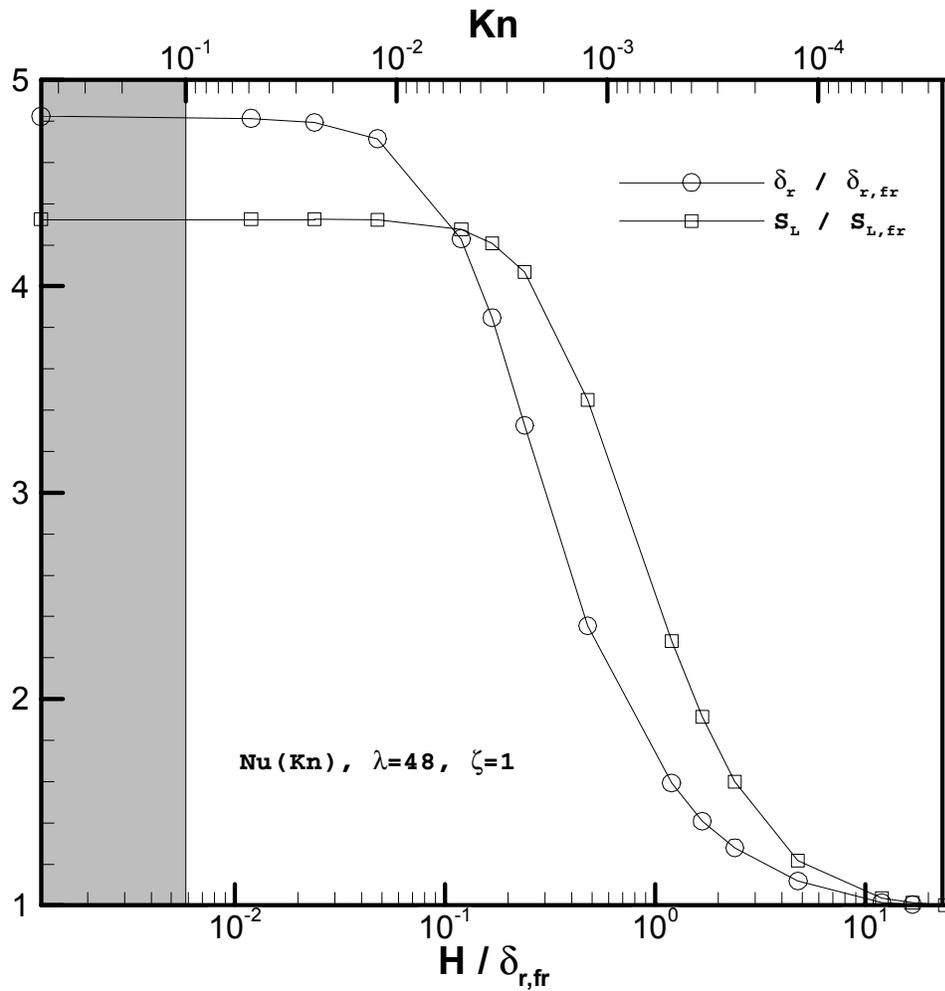
Figure 2-9: Comparison between the evolution of the normalized flame thickness, $\delta_r/\delta_{r,fr}$, and the normalized laminar flame speed, S_L. Results are from the 1D numerical model.

The results from the numerical model presented in figure 2-9 also suggest that maximizing power density may require a careful optimization over geometric (as well as thermophysical) properties of the structure. While the results of such an optimization are reported in the next chapter of this work, some insight can be gained

by computing the variation of power density with passage height for two different combustor lengths. The power density is computed from the numerical results using the following equation:

$$\dot{w}_D = \frac{\rho U \int_{T_0}^{T_f} C_p(T) dT}{L} \tag{2-23}$$

Note that the passage height and width appear in both the numerator and denominator and thus cancel each other out. As a result, the power density depends only on the enthalpy change per unit area across the flame and the passage length L.

Figure 2-10 shows the evolution of non-dimensional power density $\dot{w}_D$ as a function of normalized passage height $H/\delta_{r,fr}$ for two different values of the normalized passage length $L/\delta_{r,fr}$. The structure is assumed to be adiabatic, the values of Nu, ζ, and λ are fixed, and the power density is made non-dimensional by normalizing by the power density associated with an arbitrarily defined "macro-scale" configuration corresponding to $L=1$cm and $H=1$cm. The plot shows that reducing the passage height and reducing the passage length both increase the power density. The increase in power density with decreasing passage height is a direct consequence of the increased burning rate caused by enhanced heat transfer to the pre-flame at small passage heights while the increase in power density with decreasing combustor length is a consequence of miniaturization only.
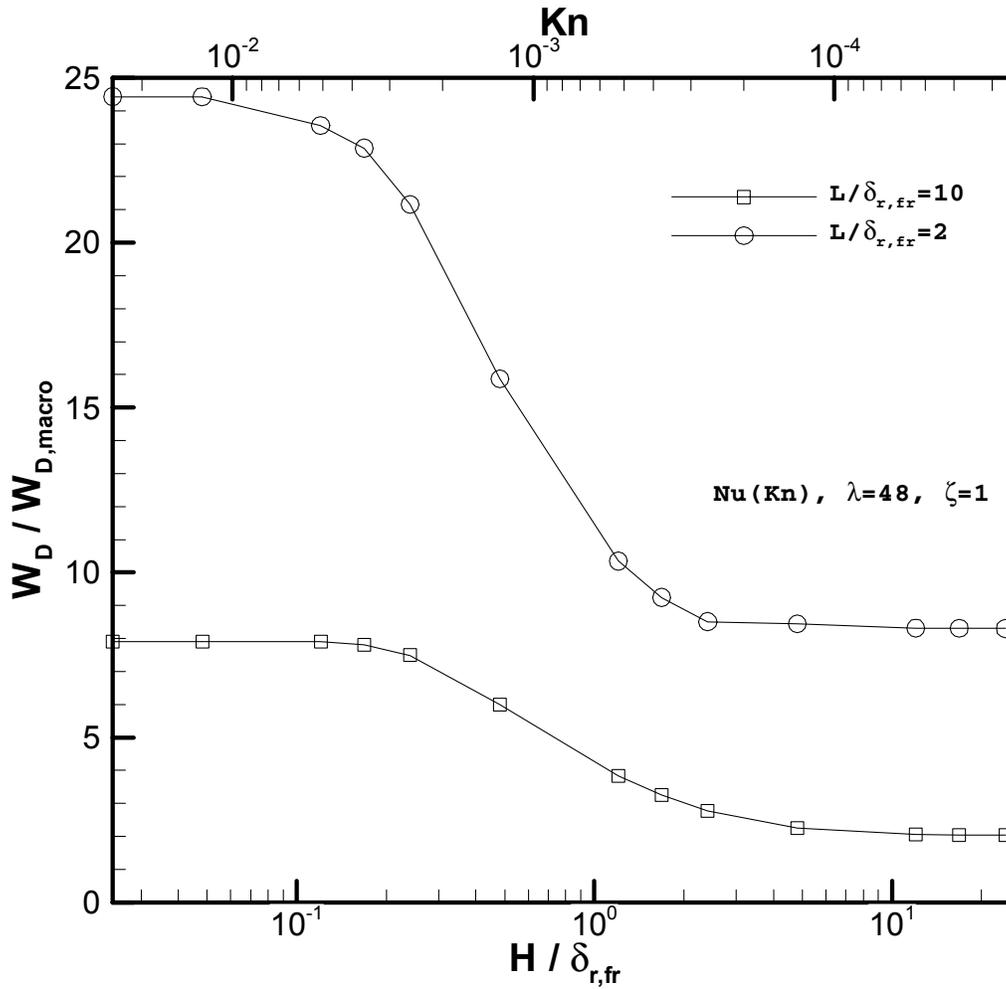
Figure 2-10: Normalized power density as a function of normalized passage height for two values of the normalized passage length. Results are from the 1D numerical model.

2.4.4. Pressure loss

Pressure loss is another important factor affecting the design, performance, and ultimate practicality of micro-combustors. A first order estimate of its magnitude in

the parallel plate geometry investigated here is made assuming that the flow is fully-developed[45]:

$$\Delta p = \frac{8\mu UL}{H^2} \qquad\qquad (2\text{-}24)$$

In this expression Δp is the pressure drop, μ is the dynamic viscosity ($\sim 50.10^{-6}$ kg/m.s for air at 1500K) and U is the velocity (taken to be the laminar flame speed S_L as an approximation). The pressure drop corresponding to the analytical model is estimated by taking the length L to be equal to the minimum combustor length (or the flame thickness) while the pressure drop corresponding to the numerical simulation is estimated by taking L to be equal to 1 cm (the length of the computational domain). The solid lines in figure 2-11 show pressure drop normalized by the pressure at the channel entrance (1 atm) as a function of non-dimensional passage height. The flame broadening results are also plotted (dashed lines) so that the passage height where the broadening phenomenon begins to occur can be compared to the passage height at which pressure losses start to become large. It is clear from the figure that the broadening phenomenon occurs well before the pressure losses between the plates become significant (i.e. greater than 5% of the total pressure). As a result, flame broadening appears to be a phenomenon that could be encountered in a 'practical' micro-combustor.
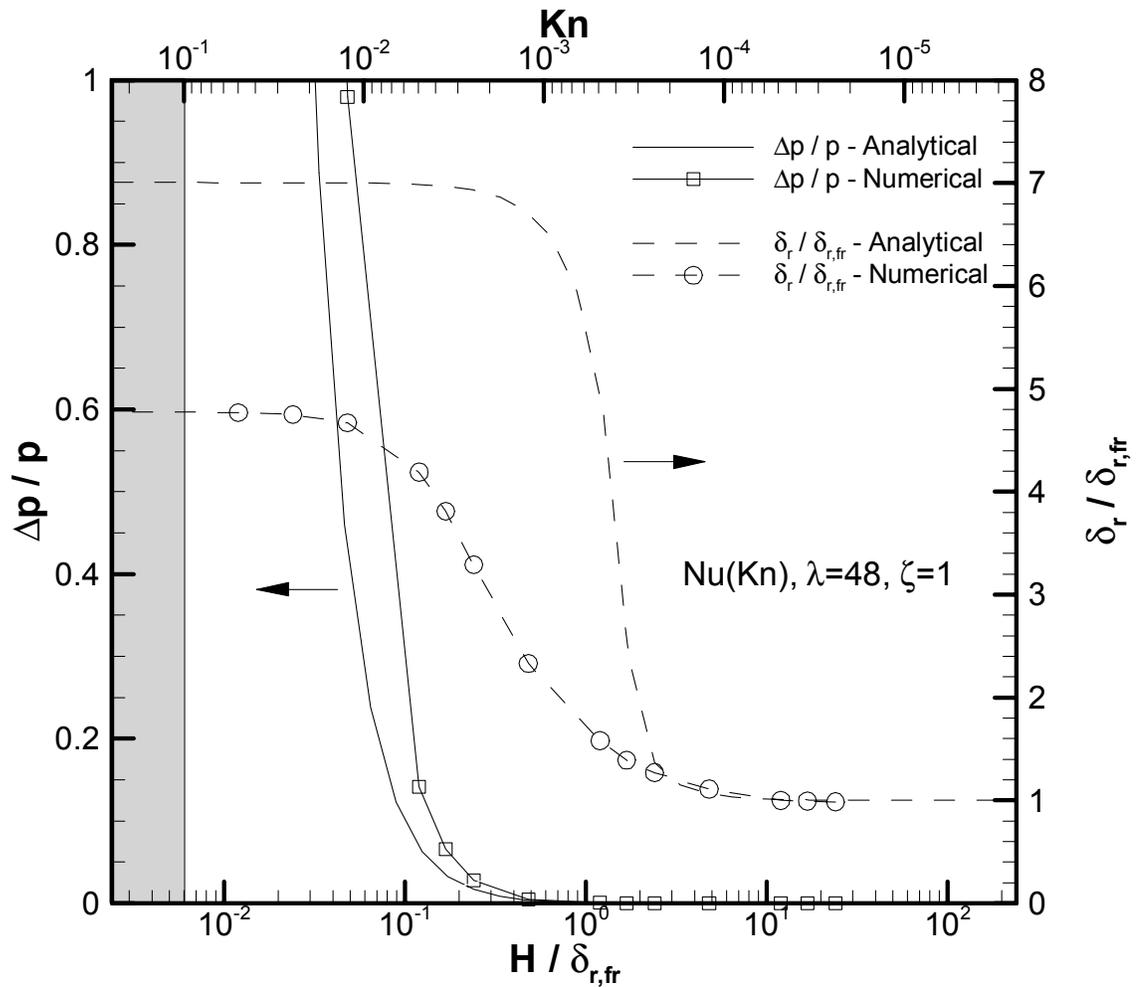
Figure 2-11: Normalized pressure drop as a function of normalized passage height. The evolution of the non-dimensional flame thickness is superimposed on the plot for comparison.

Finally, it should be noted that the increase in burning velocity with decreasing passage height is consistent with other work that uses somewhat different methods to model the chemical reaction and account for the effects of axial heat conduction in the structure. In particular, Ronney[46] used a perfectly stirred reactor (PSR) coupled

with a counter-current heat exchanger to show that higher mass flow rates were required to stable combustion when heat recirculation was present or, equivalently, when the thermal conductivity of the tubes was not small. This is qualitatively equivalent to the predictions made by the analytical model as well as those made by the numerical model where the distributed nature of the reaction zone is accounted for.

2.5. Conclusion

A simple model based on a thermal resistance network has been developed to extend the Mallard-Le Chatelier theory for a pre-mixed flame freely propagating into a reactant mixture, to a premixed flame propagating in and exchanging heat with a thermally conducting channel. In spite of its simplicity, comparisons to the results of more detailed numerical simulations that include axially distributed heat transfer and full chemistry indicate that the simple model captures many of the important features of a combustion wave stabilized in a micro-channel. Both the analytical and numerical models show that heat exchange between the reacting fluid and the structure tends to broaden the reaction zone. Both models predict that the passage height at which axial heat transfer becomes important depends on the Nusselt number, and for a given Nusselt number predict similar values for the transition passage height. Both models also predict limiting behaviors at large and small channel heights, and both indicate that increasing the conductance of the structure (either by increasing the thermal conductivity of the structure material or the structure thickness) increases the amplitude of the broadening phenomenon. The maximum

limit of flame broadening at very small heights is predicted within a factor of two by the analytical model in comparison to the numerical simulation. The simple model has been extended to include the effects of quenching via heat loss to the environment. The model extension does not predict quenching diameters well, however they still lie within a factor of 10 of the numerical simulations' predictions and show the same qualitative trends with passage height.

While the increase in flame thickness at micro-scale may initially appear to be a drawback for designing high power density combustors because it suggests that proportionally more combustor volume is required, the increase in burning rate associated with pre-heating the reactants more than compensates for this effect and the net result is an increase in power density greater than what one would expect as a result of miniaturization alone. Finally, it should be noted that mass transport to the walls as well as surface reactions there are other important aspects of the micro-combustion problem. These are not considered here and are excellent topics for future work.

Taken together, the results demonstrate the utility of the simple extension to the Mallard-Le Chatelier theory and the importance of fluid-structure coupling in micro-combustion. Experimental data is required to verify the predictions of the model and additional work in the modeling area is needed to explore optimum combustor configurations and the influence of the choice of the fuel on power density and the broadening phenomenon. The results of these investigations will provide valuable information to designers of microscale combustion systems. Work focused on identifying optimum combustor configuration is presented in the next chapter.

Chapter 3:   Power Density and Efficiency of Micro-Combustors

3.1. Introduction

In the previous chapter of this work, an analytical model was developed to explain the fact that reaction zones appear broader in small-scale combustors. This model also predicted that the burning velocity should increase because of axial heat conduction through the structure. The numerical simulations provided preliminary evidence that the net effect of miniaturization was an increase in power density.

However, the results presented were computed for only a few configurations of the combustor and the general behavior of power density as both the height and length of the micro-combustor were decreased was unclear. In addition, the effect of heat loss on power density was not included. Nevertheless, these preliminary results as well as intuition suggested the possibility for an optimum combustor configuration that maximizes power density.

The objective of the work reported in this chapter is to systematically investigate the dependence of power density on the combustor design which, in this case, is determined by its length and height. The overall combustion efficiency is also computed as it is another important performance metric. Finally, the influence of fuel type is considered by performing the calculations with both H_2 and CH_4 fuels and comparing the results.

The results shown for hydrogen combustion were presented at the 30th International Symposium on Combustion held at UIC in March 2004. They were published in *Proceedings of the Combustion Institute* 30 (2005) pp. 2437-2444.

The results for methane combustion were presented at the 43rd AIAA Aerospace Sciences Meeting and Exhibit, Reno, Nevada, January 10–13, 2005 and partly published as "Effect of Fuel Type on Optimum Micro-Combustor Design and Performance", AIAA Paper 2005-939.

3.2. Approach

The numerical model presented in Chapter 2 of this work is used to model micro-combustion between two parallel plates. A schematic diagram of the problem considered can be found in the previous chapter of this work (Figure 2-4). Surface reactions are not included and hence there is only thermal (no mass) exchange between the gas and the structure. The Nusselt number for heat transfer between the gas and structure is assumed constant at 8, the value for fully developed flow between two parallel plates[47].

Since a "realistic" combustor had to be considered in order for the results obtained to be of practical use, the plates were assumed to be made out of Silicon, a typical MEMS fabrication material. The use of silicon as a combustor material imposes two additional constraints on the simulation. The first is that the equivalence ratio be low enough so that the adiabatic flame temperature remains below the melting point of silicon (1680K). The second is that the temperature dependence of silicon's thermal

conductivity be included. This is important because silicon's thermal conductivity changes by more than a factor of five over the expected range of temperatures and is computed using a power law fit to tabulated data[48].

Using the numerical simulation it is then possible to compute the maximum inlet velocity for specific values of the geometric dimensions of the combustor L and H and the inlet velocity U. The maximum inlet velocity is chosen because we are interested in determining the maximum power density associated with a particular configuration.

3.3. Results and Discussion

3.3.1. Hydrogen Fuel

In this first part of the results section, we consider hydrogen-air combustion at equivalence ratio of 0.5. The gas-phase combustion chemistry is modeled using a nine-species, nineteen-reaction mechanism[49]. Table 4 in Appendix II shows the reactions considered in the mechanism.

Figure 3-1 is a plot of non-dimensional inlet velocity versus non-dimensional passage height for two non-dimensional channel lengths. First, note the increase in flame speed (burning velocity) as the channel height is reduced. Second, it shows that there are two limiting values of the flame speed at a particular design point. The minimum value corresponds to the flashback limit where a flame is stabilized near the channel entrance. The maximum value corresponds to the blow-off where the flame is stabilized near the channel exit. A continuum of flame speeds is possible in

between these limits.   Third, it shows that at large passage heights where the thermal

coupling with the structure is weak, the blow-off and flashback velocities converge to

the flame speed associated with a freely propagating flame. As the passage height is

reduced and the strength of the coupling between the reacting fluid and the micro-

channel structure increases, the blow-off and flashback limits diverge and it becomes

possible to stabilize a combustion wave over a range of inlet velocities. Fourth, and

finally, decreasing the passage length tends to decrease the magnitude of the flame

speed increase associated with decreasing passage height, and reduces the difference

between the blow-off and flashback limits.
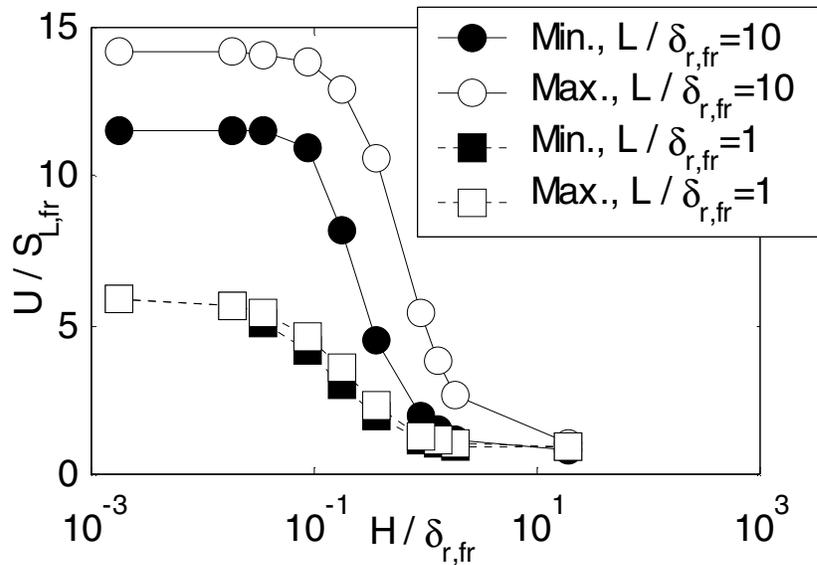
Figure 3-1: Non-dimensional flashback and blow-off limits for H_2-air combustion in a silicon micro-channel as a function of non-dimensional channel (combustor) height and for two values of the channel length *L*.   The equivalence ratio is 0.5 and the pressure is 1 atm.

The reasons for these observations can be inferred from figure 3-2 which shows axial profiles of non-dimensional temperature and major species mass fractions at inlet velocities corresponding to blow-off and flashback.
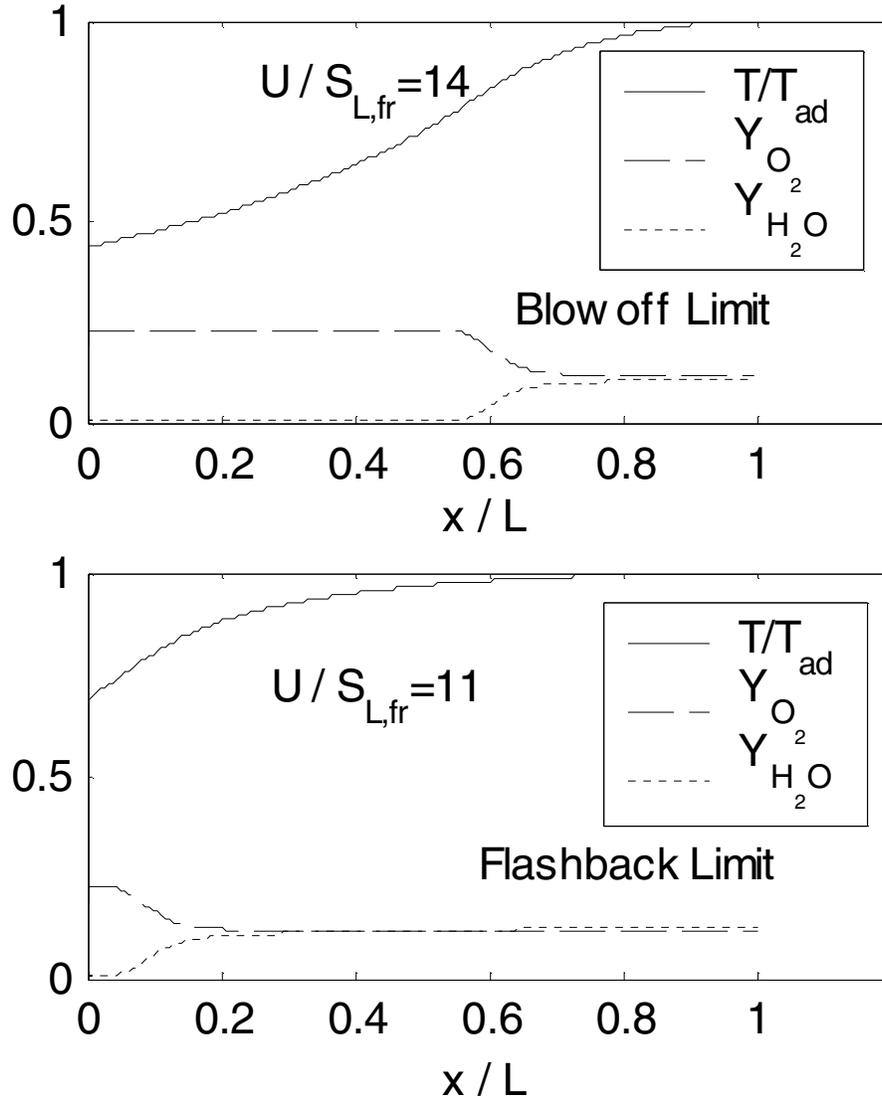
Figure 3-2: Axial profiles of temperature and major species concentration for a H₂-Air flame stabilized in a silicon micro-channel with $H/\delta_{r,fr} = 0.002$ **and** $L/\delta_{r,fr} = 9$. **The equivalence ratio is 0.5 and the pressure is 1 atm.**

The profiles indicate that the flame is stabilized near the channel exit at the blow-off limit while it is stabilized near the channel entrance at the flashback limit. The flame speed is higher when the flame is stabilized at the channel exit because there is more surface area for heat exchange between the structure and the reactants, and hence more pre-heating of the mixture before reaction occurs. Decreasing the overall length of the combustor reduces the surface area for heat exchange between the structure and the reactants, reduces the pre-heating of the mixture, and thus reduces the flame speed. The blow-off and flashback limits come together as the channel length is reduced because decreasing the length of the micro-channel decreases the range of possible stable flame locations within the channel. This, in turn, decreases the range of stable inlet velocities.

It is interesting to note that the temperature profiles presented in figure 3-2 do not show the temperature overshoot characteristic of excess enthalpy burners. This is because the profiles in figure 3-2 correspond to relatively small passage heights where the heat transfer coefficient is large and thermal equilibrium between the gas and the structure is established very quickly. This is consistent with the results of Takeno[50] which show a reduction in the thermal overshoot when the thermal coupling between the gas and the structure is strong. Thermal overshoot *is* observed at larger passage heights where the thermal coupling is weaker and thermal equilibrium takes longer to establish. The physical bases for the 'smoothing out' of temperature and species gradients in micro-scale systems have been discussed by Pello[51].

Thermal coupling between the reacting gas and the structure has important implications for the design of efficient, high power density combustors. The overall

efficiency of a micro-channel combustor can be written as the product of a chemical efficiency and a thermal efficiency:

$$\eta_o = \eta_{ch}\eta_{th} \tag{3-1}$$

The chemical efficiency is defined as the ratio of the total heat evolved in the reaction to the total heat available if the reaction were to go to completion. In this work, we assume that this is equivalent to the fraction of H_2 that gets consumed before the mixture exits the micro-channel:

$$\eta_{ch} = \frac{Total\ heat\ evolved\ by\ rxn.}{Maximum\ heat\ available} = 1 - \frac{Y_{H_2,out}}{Y_{H_2,i}} \tag{3-2}$$

The thermal efficiency is defined as the ratio of the total heat actually delivered to the flow exiting the channel divided by the total heat evolved by the reaction. This is computed from the axial temperature profile through the micro-channel, the heat loss to the environment, and the mass flow rate:

$$\eta_{th} = \frac{Total\ heat\ delivered\ to\ flow}{Total\ heat\ evolved\ by\ rxn}$$
$$= \frac{\displaystyle\int_{T_i}^{T_{out}} C_p(T)dT}{\displaystyle\int_{T_i}^{T_{out}} C_p(T)dT + \dot{q}_{loss}/\dot{m}} \tag{3-3}$$

The power density is defined as follows:

$$\dot{w}_D = \frac{\dot{W}}{V} \tag{3-4}$$

60

where $\dot{W}$ is the energy release rate due to combustion (computed as $\dot{m} \int_{T_i}^{T_{out}} C_p(T)dT$)

and V is the combustor volume.

The solid contours in figure 3-3 show maximum non-dimensional power density as a function of micro-channel length and height for H_2-air combustion at an equivalence ratio of 0.5, atmospheric pressure, and no heat loss to the environment. Channel height and length are non-dimensionalized by the reaction zone thickness of a freely propagating H_2-air flame. Power density is non-dimensionalized with respect to a reference value associated with combustion in a channel where L and H equal 1 cm. This reference channel is sufficiently large that there is essentially no influence of the structure on the combustion process. Note that the maximum power density associated with a particular combustor design (i.e. L and H) occurs when the inlet velocity is at the blow-off limit.

Figure 3-3 shows that there is an optimum micro-channel length where power density is maximized. The maximum is a direct consequence of thermal exchange within the structure. It arises from a competition between the decrease in channel volume and the decrease in flame speed (and hence energy release rate) as the length of the combustor is reduced. The figure shows that thermal exchange within the channel wall makes it possible to achieve power densities in excess of 60 times the maximum associated with the reference channel (H=1cm, L=1cm). Note that the power density also decreases as the channel height is increased. This is because increasing the channel height reduces the thermal coupling between the fluid and the micro-channel wall.
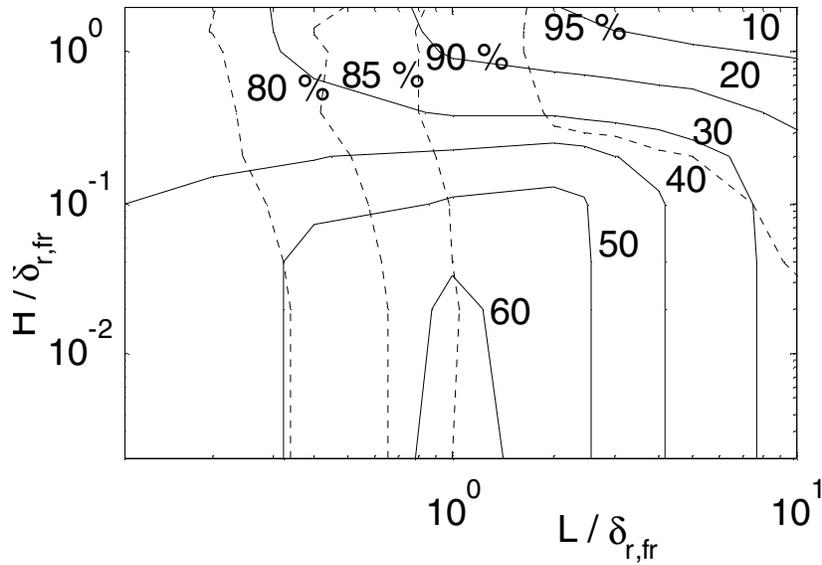
Figure 3-3: Adiabatic H₂-air combustion in a silicon micro-channel; Φ=0.5, P=1atm. Solid lines: Contours of non dimensional power density $\left(\dot{w}_D / \dot{w}_{D,ref}\right)$ as a function of non-dimensional channel height and length. Dashed lines: Contours of overall efficiency.

The dashed contours in figure 3-3 show the overall efficiency of the micro-channel combustor as a function of channel height and length. Since the combustor is adiabatic, the thermal efficiency is 100% and changes in overall efficiency are entirely the result of changes in chemical efficiency. The figure shows that power density and chemical efficiency trade against each other: Attempts to increase power density by decreasing the length of the channel reduce the degree of chemical conversion by decreasing the time available to complete chemical reaction. The figure also shows that heat exchange with the structure drives the configurations associated with maximum efficiency and maximum power density farther apart.

Thermal efficiency also changes with combustor configuration when heat loss to the environment is included. Figure 3-4 shows that heat loss, simulated by introducing a heat transfer coefficient of 1 W/m^{2}K between the micro-channel and the environment, eventually quenches reaction as channel height is reduced. One would expect similar behavior as channel length is reduced because of reduced chemical efficiency.
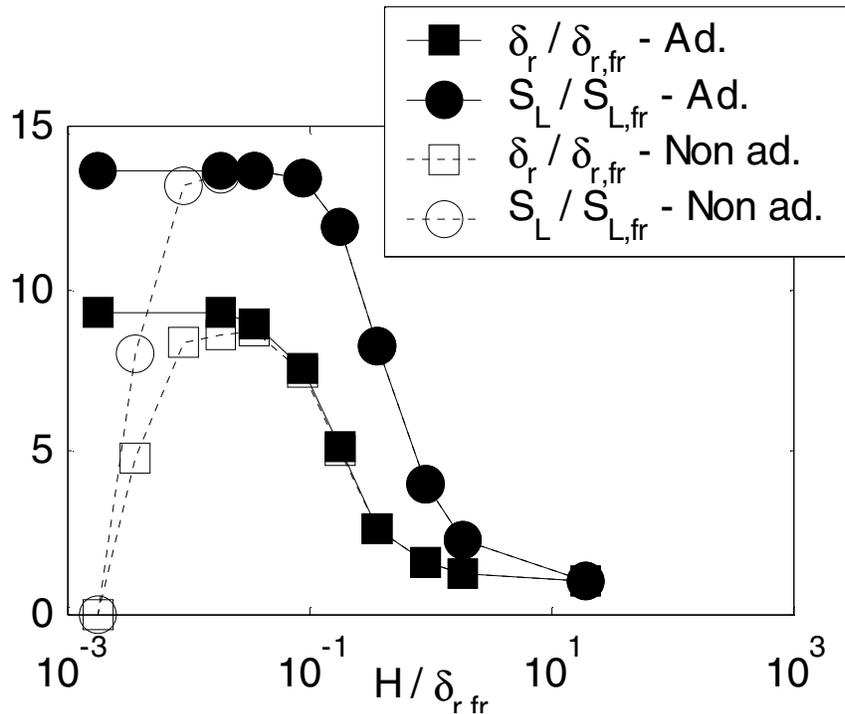
Figure 3-4: Adiabatic (solid lines) and non-adiabatic (dashed lines) H$_2$-air combustion in a silicon micro-channel; Φ=0.5, P=1atm, h_{env}=1 W/m^{2}K, $L/\delta_{r,fr}$=20. The circles show non-dimensional laminar flame speed as a function of non-dimensional channel height while the squares show non-dimensional reaction zone thickness.

These effects are observed in figure 3-5 as the contours of overall efficiency (dashed lines) shift upward and to the right. The subsequent reduction in overall efficiency that arises from heat loss at small passage heights reduces the power density and creates the global maximum in power density shown in the solid contours. There is now a single, optimum, combination of L and H that maximizes power density. Not surprisingly, the maximum power density and the efficiency at this point are somewhat lower than those in the adiabatic case. It is important to note that the non-adiabatic power density is only slightly less than the adiabatic value because the heat transfer coefficient between the combustor and the environment is very small. In practice, one would expect heat losses to be much larger and the maximum realizable power density to be much lower.
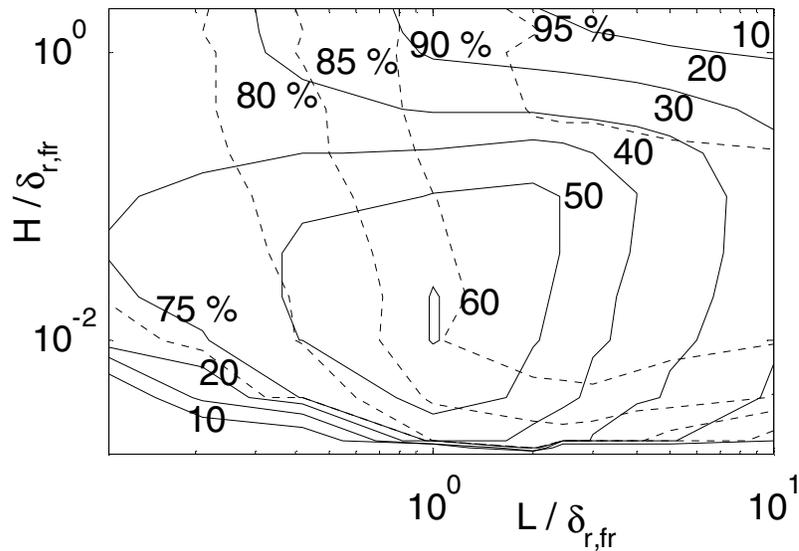
Figure 3-5: Non-adiabatic H$_2$-air combustion in a silicon micro-channel; Φ=0.5, P=1atm, h_{env}=1 W/m^{2}K. Solid lines: Contours of non dimensional power density $\left(\dot{w}_D / \dot{w}_{D,ref} \right)$ as a function of non-dimensional channel height and length. Dashed lines: Contours of overall efficiency.

Figure 3-6 is a plot of power density and efficiency at a combustor pressure of 5 atmospheres under non-adiabatic conditions.
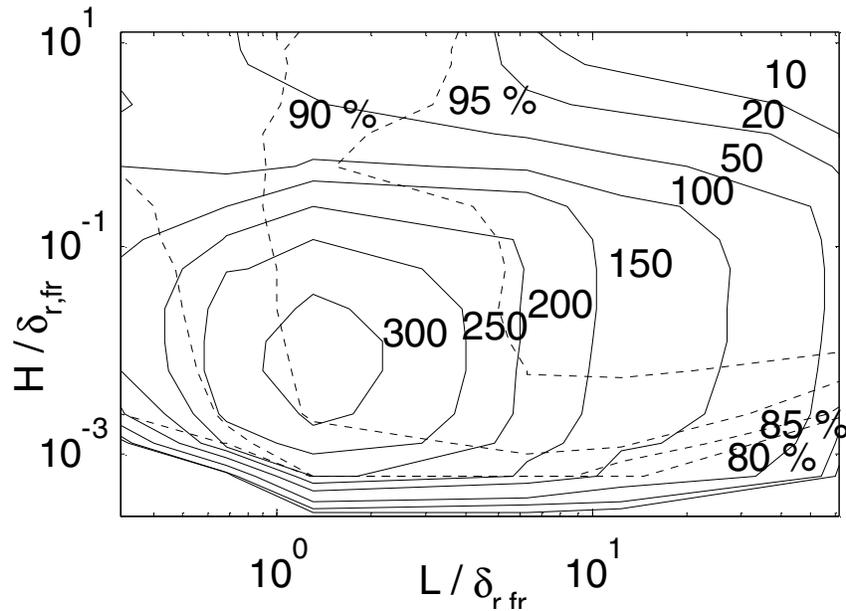
Figure 3-6: Non-adiabatic H$_2$-air combustion in a silicon micro-channel; Φ=0.5, P=5atm, h_{env}=1 W/m^{2}K. Solid lines: Contours of non dimensional power density $\left(\dot{w}_D/\dot{w}_{D,ref}\right)$ as a function of non-dimensional channel height and length. Dashed Lines: Contours of overall efficiency.

It shows that increasing the pressure increases the maximum power density and reduces the values of L and H associated with the optimum. The reason for this is that the reaction zone thickness decreases with increasing pressure. The power density increases because the flame speed is higher and because an acceptable level of chemical conversion can be achieved in a smaller volume. Note that an increase in

flame speed with pressure is consistent with mixtures having burning velocities greater than 50 cm/s[52]. In these flames, temperatures are high enough that dissociation is important. Increasing the pressure represses dissociation, steepens the temperature profile, and increases the burning velocity. Since thermal feedback to the pre-flame through the micro-channel structure tends to increase the mixture temperature, one would expect flames stabilized in micro-channels to be more sensitive to pressure than freely propagating flames.

Figure 3-6 also shows that increasing the pressure increases the overall efficiency at the maximum power density point. The reason for this is that the wall temperature, and hence the heat loss from the micro-channel to the environment, remains approximately constant as the pressure is increased. This increases the thermal efficiency by decreasing the ratio of the heat lost to the heat produced.

Figure 3-7 illustrates the general effect of pressure on the the performance of combustors at conventional scale and micro-scale. The figure shows that for our "reference" meso-scale combustor for which H=L=1cm, power density increases as $P^{1.2}$. This is to compare to the increase in maximum power density of a micro-scale combustor, which increases as P^2.
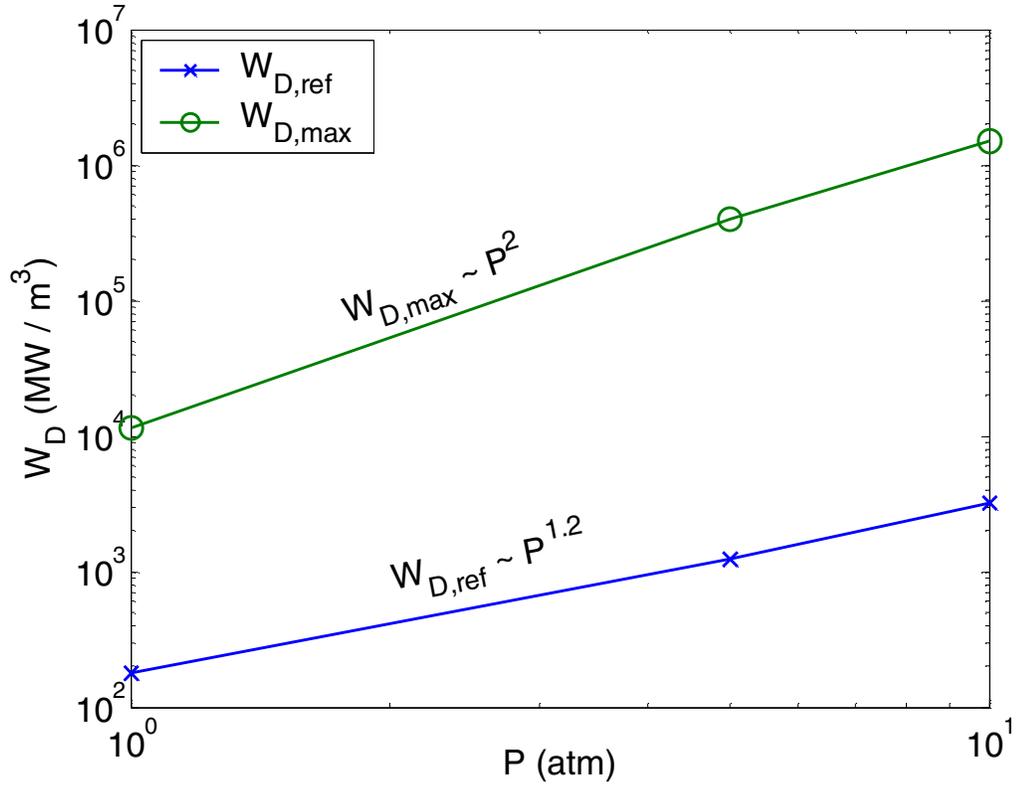
Figure 3-7: Evolution of power density with increasing pressure for a meso-scale combustor and a micro-combustor.

The results of the power density and efficiency calculations are summarized in Table 2 and show that the reaction zone thickness doesn't change much as pressure is increased from 5 to 10 atm. As a result, the optimum channel length and height associated with the maximum power density remains approximately constant. It is important to point out that the optimum values of L and H listed in table 2 are estimated using the contour plots and are not the result of an optimization in L and H. Since the peaks in power density are relatively flat, the uncertainty in the optimum values of L and H is relatively large. As a result, we are unable to make precise

estimates of the optimum combustor volume per unit channel depth and the values in the last row of table 2 are included only as general references.

Parameter	1 atm		5 atm		10 atm	
	Ad.	Non-Ad.	Ad.	Non-Ad.	Ad.	Non-Ad.
$\dot{w}_D/\dot{w}_{D,ref}$	64	60	326	323	475	471
$H/\delta_{r,fr}$	<0.002	0.01	<0.012	0.006	<0.1	0.016
$L/\delta_{r,fr}$	1	1	1.31	1.31	1.6	1.6
$U/S_{L,ref}$	5.44	5.16	4.44	4.42	5.06	5.01
Efficiency (%)	90	89	92	91	96	96
$\dot{w}_{D,ref}$ (MW/cm^3)	177	177	1230	1230	3180	3180
$\delta_{r,fr}$ (cm)	0.055	0.055	0.008	0.008	0.006	0.006
$S_{L,fr}$ (cm/s)	90	90	136	136	187	187
V (cm^3/cm)	<6x10^{-6}	30x10^{-6}	<1x10^{-6}	0.5x10^{-6}	<5.8x10^{-6}	0.9x10^{-6}

Table 2: Summary of optimum power density configurations for a silicon micro-combustor. The fuel is H2 burning in air and the equivalence ratio is 0.5.

Finally, is important to note there are other factors that are important to the design of optimum micro-combustors that have not been discussed here. The first is the conductance (the product of the thermal conductivity and the cross-sectional area) which limits upstream heat conduction through the structure. In this work, the ratio of

the wall thickness to the passage height is fixed at ½. If this value were made very small, no thermal feedback would occur and hence no optimum power density configuration would be observed. Similarly, making this parameter very large would increase the power density at the optimum until a limit imposed by the heat transfer coefficient between the gas and the structure is reached. The second factor is the pressure drop which is a very important consideration when integrating a combustor into a power cycle. The pressure drop cannot be determined using the present one-dimensional formulation that does not include the momentum equation. However, we have used a simple Poiseuille flow approximation to provide an estimate. Pressure drops near the optimum in figure 3-6 are about 10% or less. This indicates that combustors designed to be at or near the optimum power density configuration could be integrated into practical power systems.

3.3.2. Methane Fuel

The results presented in the previous part of this work considered hydrogen-air combustion. To determine how the results obtained change with fuel, methane-air combustion at an equivalence ratio of 0.5 is now considered. The Leeds mechanism[53], which includes 37 species and 175 reactions, is used to represent the gas phase chemistry. The Leeds mechanism was chosen because it does not include nitrogen chemistry, which is not of interest in the present study and greatly increases the speed of the calculations. Using a larger mechanism like GRI-Mech would have been computationally prohibitive. Table 5 in Appendix II shows the reactions considered in the mechanism.

Temperature overshoot is a well-known characteristic of heat recirculating burners[24]. Some of the enthalpy generated in the post-flame can be transferred to the pre-heat zone, allowing combustion to occur at a higher preheat temperature and thus increasing the flame temperature and burning velocity. A very comprehensive analysis of heat recirculating burners can be found in Weinberg[24].

A non-dimensional temperature overshoot is defined as:

$$\tau = \frac{T_{max} - T_{ad}}{T_{ad}} \qquad (3\text{-}5)$$

where T_{max} is the maximum temperature achieved within the flame, and T_{ad} is the adiabatic flame temperature. It is important to note that while temperature overshoot is observed in hydrogen-fueled heat recirculating burners, the effect is much stronger in methane-fueled burners.

Figure 3-8 shows the evolution of the non-dimensional temperature overshoot and non-dimensional burning velocity $S_L / S_{L,fr}$ as a function of non-dimensional passage height $H / \delta_{r,fr}$ for a fixed value of the non-dimensional passage length ($L / \delta_{r,fr} = 10$) and under adiabatic conditions. The figure shows that for large values of H, the thermal coupling between the gas and the structure is weak, and consequently the amount of heat recirculation is small. This leads to a small temperature overshoot as well as a burning velocity close to that of a freely-propagating flame.
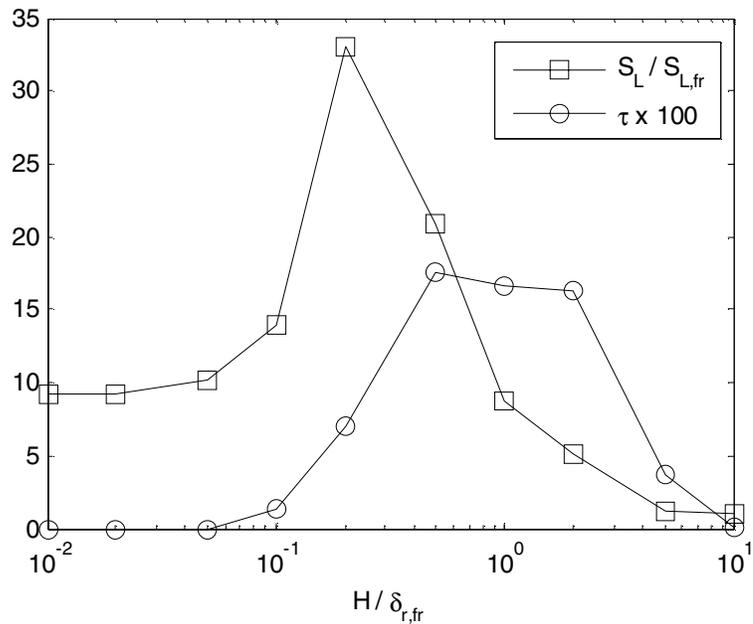
Figure 3-8. Evolution of normalized flame speed and non-dimensional temperature overshoot as a function of normalized passage height.

As the passage height is decreased, the thermal coupling becomes stronger and this creates a significant temperature overshoot. This, in turn, elevates the burning velocity. At some point, however, continuing to reduce the passage height starts to decrease the temperature overshoot again. This is a direct consequence of the fact that heat recirculation broadens the reaction zone: Broadening the reaction zone reduces the temperature gradient driving heat from the post-flame to the pre-flame, and decreases the overall heat transfer to the reactants. With less heat being transferred upstream, the chemical kinetics run slower again. However, since the flame speed is the reaction zone thickness divided by the overall reaction rate, the flame speed remains elevated. The limiting value of the flame speed as H becomes very small is set by the amount of heat that can be conducted through the structure, or

by its thermal conductance. The net result, however, is that the burning velocity is maximized for a certain value of the passage height. This maximum is a direct result of a tradeoff between the strength of the thermal coupling between the gas and the structure and the ability to support temperature gradients in the axial (streamwise) direction. Making the passage length shorter magnifies the effect of flame broadening on the axial temperature gradients responsible for the peak in flame speed and eventually causes the peak to disappear. This is illustrated in figure 3-9.
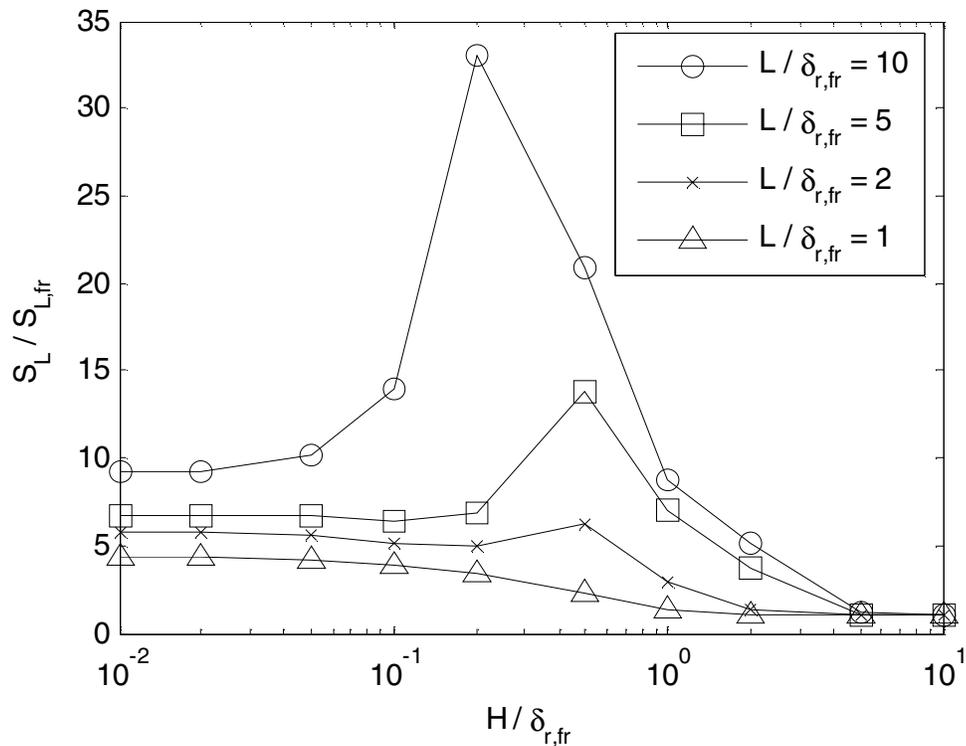
Figure 3-9: Evolution of normalized flame speed as a function of normalized passage height for different values of the normalized passage length.

Figure 3-10 shows contours of non-dimensional power density as a function of normalized passage height and length in the adiabatic case.

72
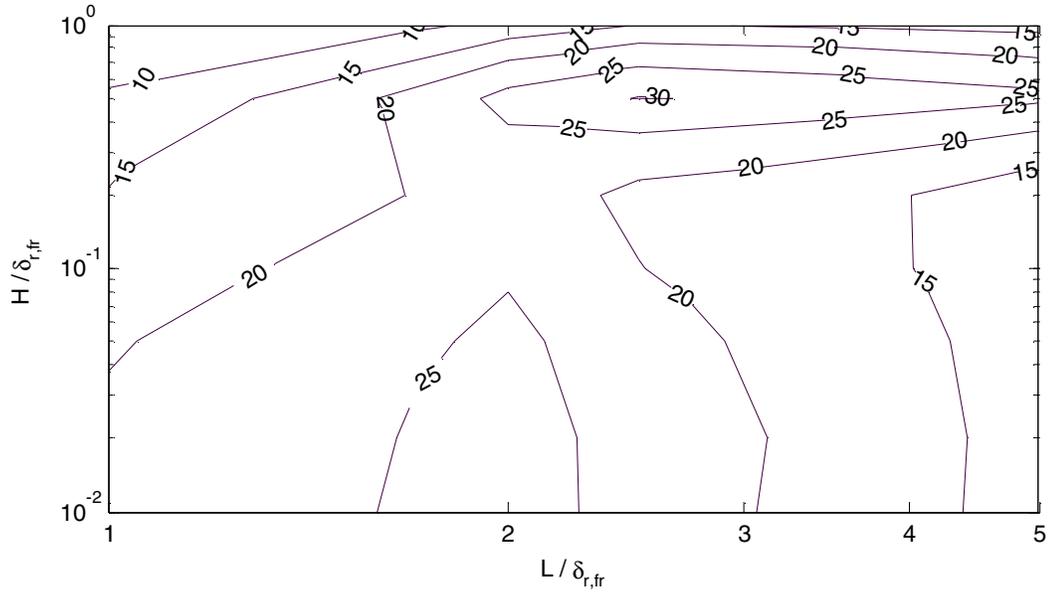
Figure 3-10. Adiabatic CH$_4$-air combustion in a silicon micro-channel; Φ=0.5, P=1atm. Contours of non dimensional power density $\left(\dot{w}_D \big/ \dot{w}_{D,ref}\right)$ as a function of non-dimensional channel height and length.

Since the flow is adiabatic, the overall efficiency is determined solely by the chemical efficiency. In the range of configurations considered in figure 3-10, the chemical efficiency is very close to 1. A possible explanation for this will be presented later in this section. The figure shows that there are actually two maxima in power density (as opposed to only one for H$_2$-air combustion). The first maximum is global and corresponds to a particular configuration of the combustor, more precisely H=0.5mm and L=2.5mm. It arises from the two phenomena identified earlier: the maximum in burning rate at a particular height, and the trade-off between compactness and heat recirculation potential as passage length decreases. The second maximum is analogous to the maximum observed in earlier work on adiabatic

hydrogen-air micro-combustors where there is a combustor length that maximizes power density for passage heights smaller than a particular value. It results from the elevation of burning rate at small passage heights and the increase in compactness as the passage length is reduced.

Heat loss to the environment imposes important additional constraints on the performance of micro-combustors. Figure 3-11 shows contours of non-dimensional power density as a function of normalized passage height and length when the structure of the combustor loses heat to the environment with a convective heat transfer coefficient of 1 W/m^2K. Contours of thermal efficiency are also superimposed on the graph.

Two distinct maxima are apparent. The first is similar to the first one discussed in figure 3-10 as it corresponds to the combined effects of temperature overshoot and axial gradient suppression. The second arises from the fact that heat loss and the resulting thermal quenching places a lower bound on the passage height where sustained combustion is possible. This is also analogous to the results obtained in previous analyses of hydrogen-air micro-combustors such as those presented in figure 3-5 of this work.
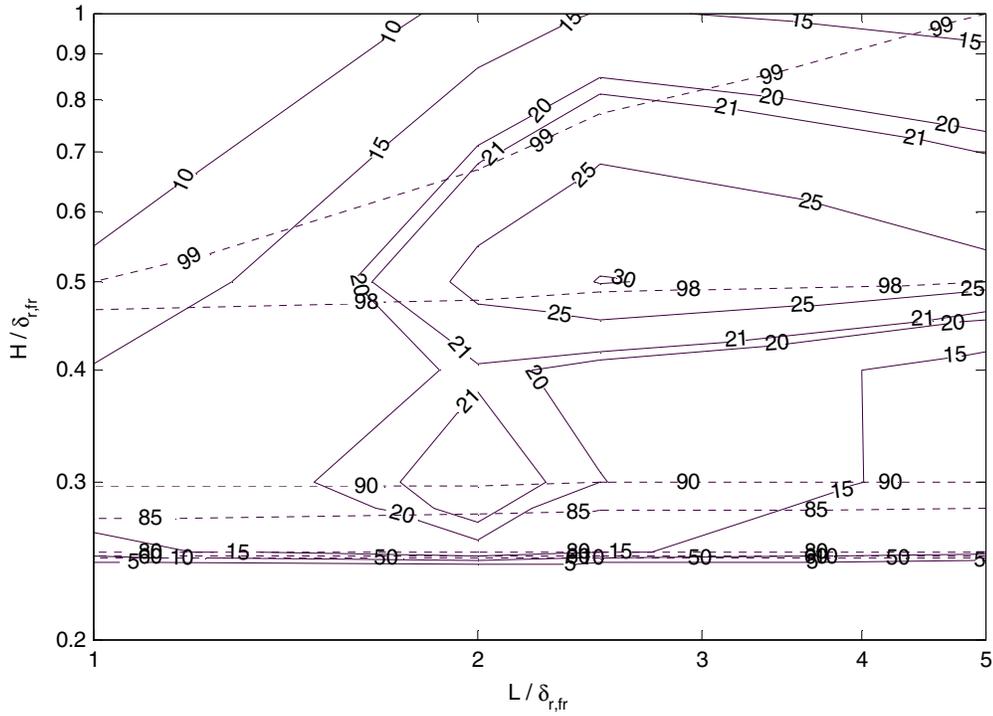
Figure 3-11: Non-adiabatic CH$_4$-air combustion in a silicon micro-channel; Φ=0.5, h_{env}=1 W/m^{2}K. Solid lines: Contours of non dimensional power density $\left(\dot{w}_D/\dot{w}_{D,ref}\right)$ as a function of non-dimensional channel height and length. Dashed Lines: Contours of overall efficiency.

The optimum power density configuration occurs at *H*=0.3mm and *L*=2mm (i.e. *H/$\delta_{r,fr}$*=0.3, *L/$\delta_{r,fr}$*=2 in non-dimensional units) and is associated with the temperature overshoot. The second maximum is not as beneficial as the first one for two reasons. First, the value for power density obtained at the second maximum is lower than that obtained at the first one (22 vs. 30). Second, since the passage height associated with the second maximum is lower than that for the first one, heat loss is more significant and consequently thermal efficiency is lower (90% vs. 98%).

75

Figures 3-12 and 3-13 show why there are two optimum configurations for a methane combustor whereas there is only one for a hydrogen combustor. First, the temperature overshoot is much higher for methane than for hydrogen. Second, for hydrogen, the flame thickness increases monotonically with decreasing H whereas it decreases then increases for methane.
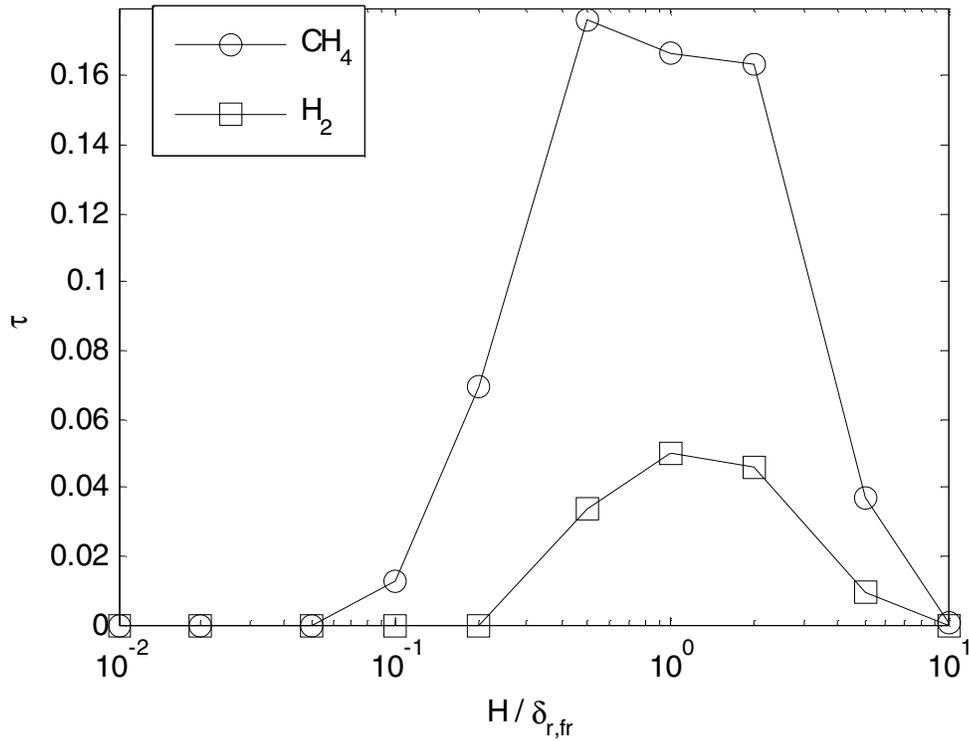
Figure 3-12: Comparison of normalized temperature overshoot for methane and hydrogen fuels.
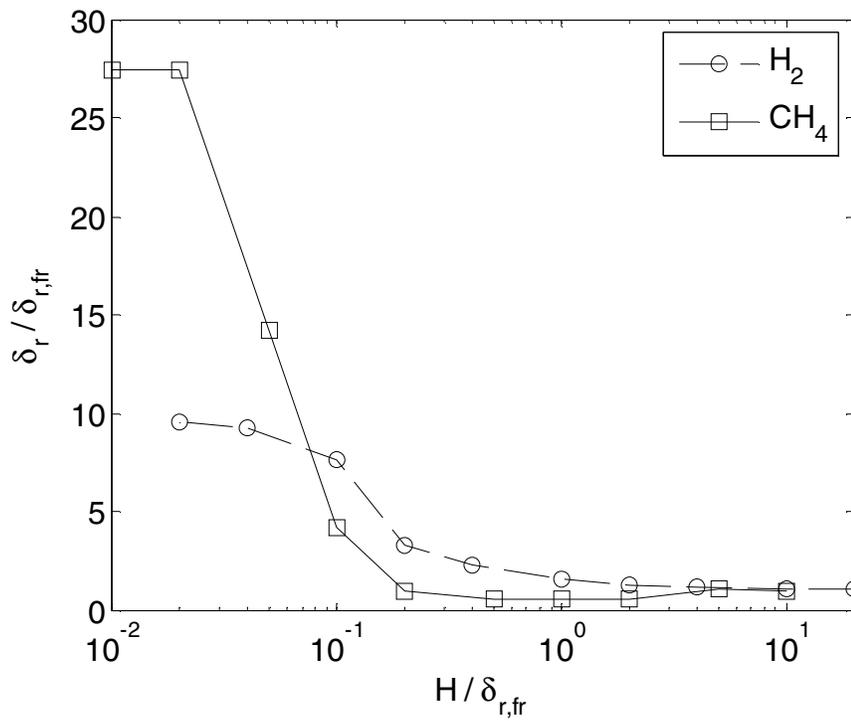
Figure 3-13: Comparison of the evolution of flame thickness for hydrogen and methane fuel as passage height is reduced.

The reasons for this difference remain unclear at this point, but one may speculate that it due either to differences between methane's and hydrogen's chemistries or differences in the thermal properties of the reactive mixtures.
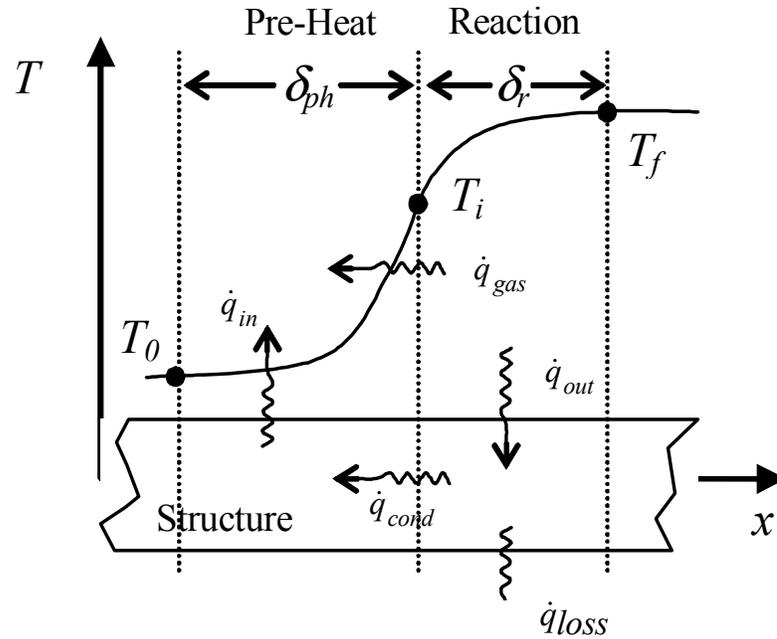
Figure 3-14: Thermal exchange in a flame in close contact with a structure. $\dot{q}_{gas}$ and $\dot{q}_{cond}$ **represent the heat conducted from the reaction zone to the pre-heat zone through the gas and through the structure respectively,** $\dot{q}_{out}$ **and** $\dot{q}_{in}$ **represent convective heat transfer between the gas and the structure, and** $\dot{q}_{loss}$ **represents the heat lost to the environment.**

Nevertheless, the fact that the temperature overshoot is larger for methane than hydrogen can be found to be a direct consequence of the non-monotone behavior of methane's flame thickness with decreasing passage height. Indeed, one of the consequences of the fact that flame thickness decreases can be found by computing an approximation of the total heat flux from reaction zone to pre-flame in the

situation shown in figure 3-14. Assuming perfect heat transfer between gas and structure, this can be written:

$$\dot{q}_{reaction \rightarrow pre-flame} = -k_g \frac{\partial T_g}{\partial x} - k_s \frac{\partial T_s}{\partial x} \propto \frac{1}{\delta_r} \tag{3-6}$$

The above expression shows that this heat flux is to first order inversely proportional to flame thickness. Thus, if flame thickness decreases, the amount of heat transferred to the pre-heat zone increases, thereby increasing the amount of pre-heating and contributing to a large temperature overshoot.

The second maximum shared by CH_4 and H_2 appears at different configurations. For methane, it occurs at H=300 μm and L=2 mm (i.e. $H/\delta_{r,fr}$=0.3, $L/\delta_{r,fr}$=2 in non-dimensional units), while for hydrogen the optimum configuration is H=5 μm and L=500 μm (i.e. $H/\delta_{r,fr}$=0.01, $L/\delta_{r,fr}$=1 in non-dimensional units). While the optimum non-dimensional passage length is similar for the two fuels considered, there is a large discrepancy between the optimum non-dimensional passage heights. This is due to the fact that quenching of the hydrogen flame occurs at a much smaller passage height than for the methane flame.

Another notable difference is that for CH_4, the chemical efficiency appears to be approximately constant and equal to 1 (i.e. 100%) over the range of configurations considered. This contrasts with the H_2 results that showed there were some regions of the design space where chemical efficiencies were less than 1. A possible explanation lies in the fact that while the flame thickness is of the same order of magnitude for both fuels, the burning velocity is much higher for hydrogen than for methane (~1 m/s vs. 7 cm/s). As a result, for a given configuration, the residence time in a micro-channel where a methane flame is stabilized is much larger than in a

channel where a hydrogen flame is stabilized. If the length of the combustor is reduced beyond the range covered in Fig. 3-11, the chemical efficiency eventually does decrease as illustrated in Fig. 3-15 but it does so at much smaller passage lengths than one would expect for hydrogen.
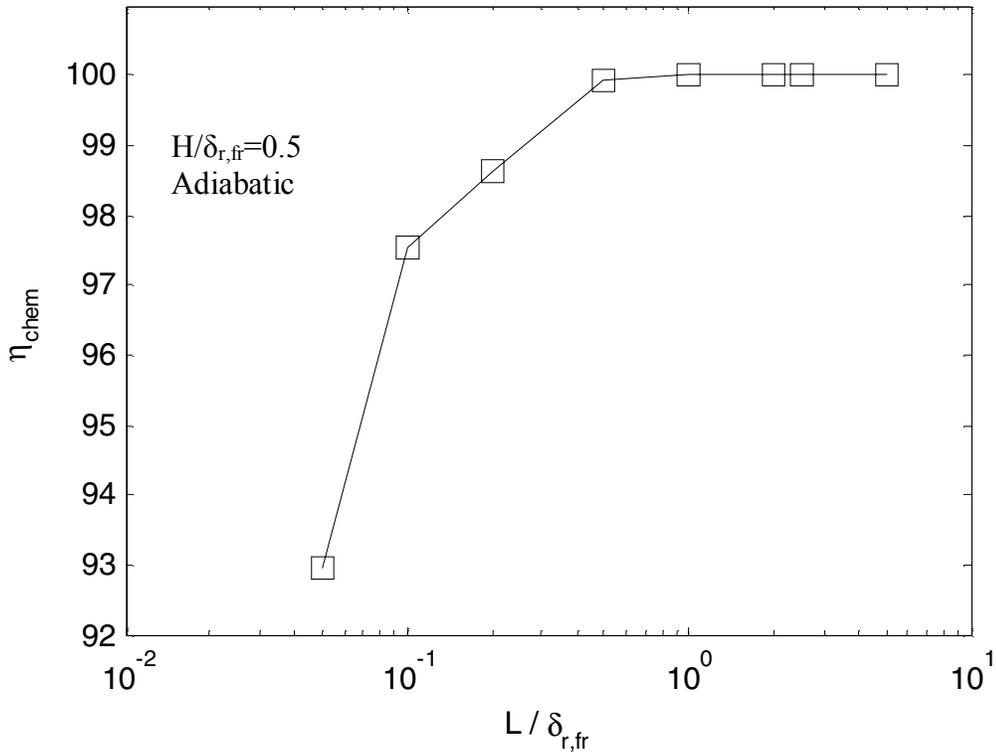
Figure 3-15: Evolution of chemical efficiency as the passage length is reduced at fixed passage height. The fuel is methane at equivalence ratio of 0.5.

Taken together, these results indicate that there may be some advantages to using methane as opposed to hydrogen in micro-combustors. First, since an optimum power density configuration is realized at a relatively large combustor size, optimized methane micro-combustors ought to be easier to construct and have smaller pressure losses. Second, the overall efficiency associated with this configuration is relatively

high so that one is not forced to trade chemical and thermal efficiency for power density as in hydrogen-powered micro-combustors. Third, the shapes of the efficiency contours indicate that it should be possible to construct smaller methane combustors that still have high chemical efficiency. The disadvantage, however, is that the maximum improvement in power density that can be achieved via miniaturization of a methane combustor is about half that of a hydrogen combustor: Peak normalized power density is on the order of 30 for methane as opposed to 60 for hydrogen.

3.4. Conclusion

A one-dimensional numerical model for reacting flow in a micro-channel has been developed to identify optimum configurations for micro-combustors. The model shows that as the size of a combustor is reduced, axial heat transfer through the structure from the post-flame to the pre-flame plays an increasingly important role in determining its performance. While axial heat transfer tends to broaden the reaction zone, it also increases the burning rate by pre-heating the incoming reactants. Since the increase in reaction rate is larger than the increase in reaction zone thickness, the net result is an increase in power density. Axial heat transfer through the structure also provides a mechanism for flame stabilization and the maximum power density for a particular combustor design (values of L and H) occurs at the blow-off limit. Heat transfer from the structure to the environment places a lower limit on the combustor volume that tends to decrease with increasing pressure. The combustor

design that maximizes power density generally does not maximize efficiency. However, operation at elevated pressures tends to improve overall efficiency by increasing the burning rate and decreasing the reaction zone thickness. Similar results were obtained when methane fuel was considered. However, the presence of a second optimum configuration in power density (at larger dimensions) suggests the importance of chemistry in the optimization process. In summary, axial heat transfer through the structure, in addition to heat loss to the environment, has important effects on the stability and performance of micro-combustors and should be included when estimating micro-combustor performance.

Chapter 4:   Micro-Thruster Design and Performance

4.1. Introduction

The results presented in the previous chapters have focused on an idealized problem - a parallel plate micro-combustor. They suggested that the configuration of a micro-combustor could be optimized for maximum power density, but at the price of lower combustion efficiency. The ultimate objective of the research project, however, is to evaluate the effect of structural heat conduction on the design and performance of micro-thrusters. Therefore, the objective of this chapter is to apply what we have learned from the study of the model micro-combustor problem to the design of a micro-thruster.

To do so the following approach is used: The idea is to couple an arbitrary geometry micro-nozzle to the idealized micro-combustor to simulate a complete micro-thruster. This is accomplished by using the results obtained in the previous chapter of this work to determine the flow conditions exiting the micro-thruster's combustion chamber, and the passing those results on to a simplified numerical model for the compressible flow within the micro-nozzle. The strategy is illustrated in figure 4-1.

Outlet flow conditions of combustion chamber
↔ Inlet conditions of micro-nozzle

Micro-thruster outlet
Computed using micro-
nozzle numerical code

L

H

Reactants
(entering at S_L)

Combustion chamber
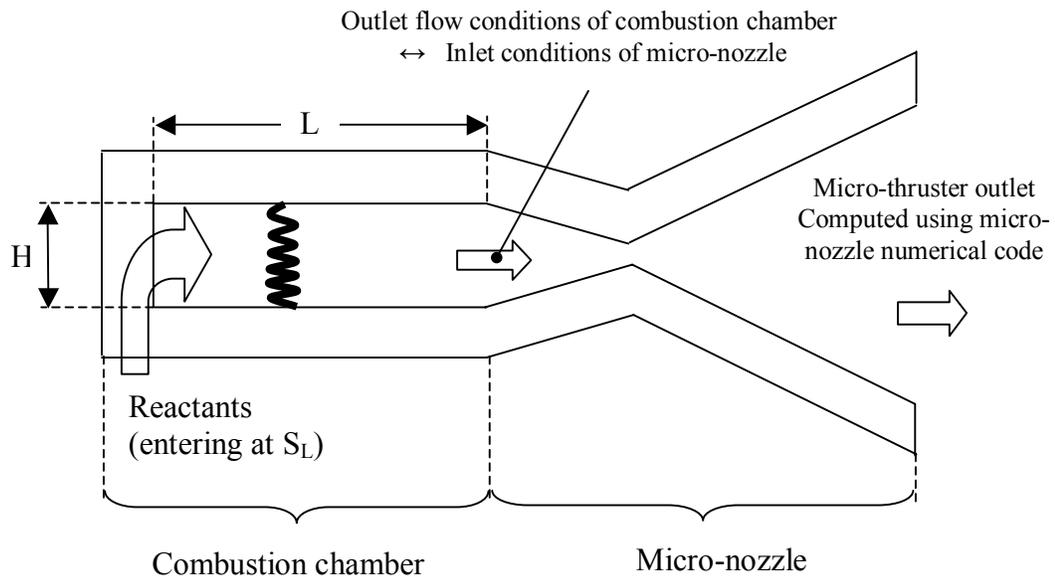
Micro-nozzle

Figure 4-1: Illustration of the strategy for estimating the performance of a micro-thruster.

4.2. Model for the micro-nozzle

For the purpose of this analysis, the arbitrary geometry illustrated in figure 4-2 is used to represent a planar converging-diverging nozzle. Since the geometry is pnar, the flow is assumed to be quasi-1D and the device is assumed to have unit width. The nozzle has an entrance height of H_0, a throat height of rH_0 and an exit height of $2H_0$. The thickness of the walls of the nozzle is $H_0/2$ to match the similar assumption made for the micro-combustor considered in Chapter 3. The length of the nozzle is $L_N=2H_0$ and the throat is located at $L_N/4$. $H(x)$ is the x-varying nozzle height. Since the problem considered is quasi-1D, $H(x)$ defines the nozzle area $A(x)$.
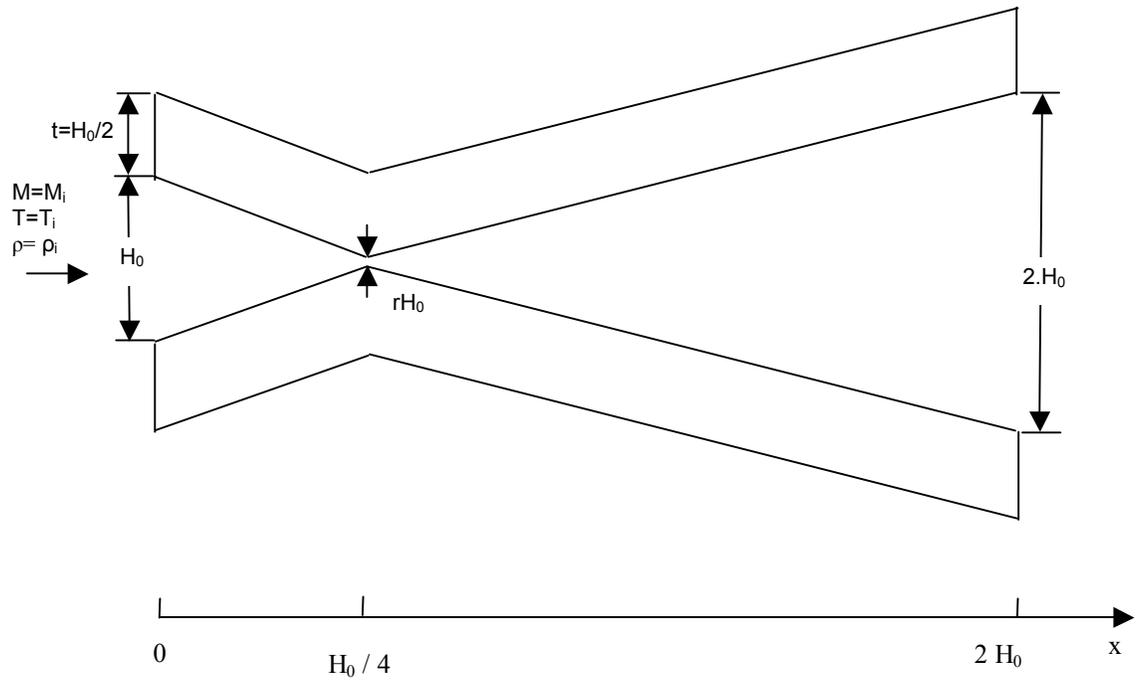
Figure 4-2: Schematic diagram of a model micro-nozzle.

The results reported in the previous chapter of this work are used to determine the conditions at the nozzle entrance. The exit temperature and velocity from the combustor define the Mach number of the flow entering the nozzle:

$$M_i = \frac{u_i}{\sqrt{\gamma R T_i}} \qquad (4\text{-}1)$$

Figure 4-3 shows the contours of Mach number as a function of L and H.
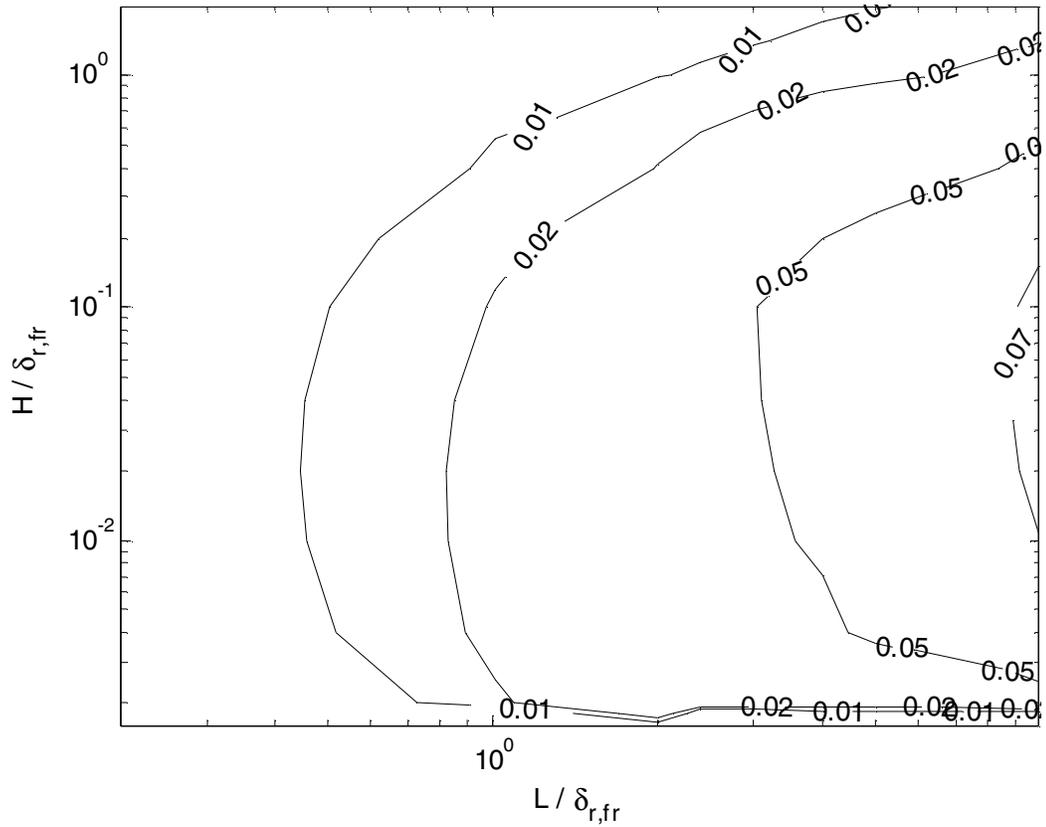
Figure 4-3: **Contours of nozzle inlet Mach number as a function of combustor configuration.**

The required value of r (throat to inlet height ratio) necessary to achieve a subsonic-supersonic isentropic flow is determined using the data presented in figure 4-3 and the well-known area-Mach number relationship[54]:

$$r = \left[\frac{1}{M_i^2} \left(\frac{2}{\gamma+1} \left(1 + \frac{\gamma-1}{2} M_i^2 \right) \right) \right]^{-0.5} \tag{4-2}$$

Figure 4-4 shows contours of r as a function of combustor configuration.
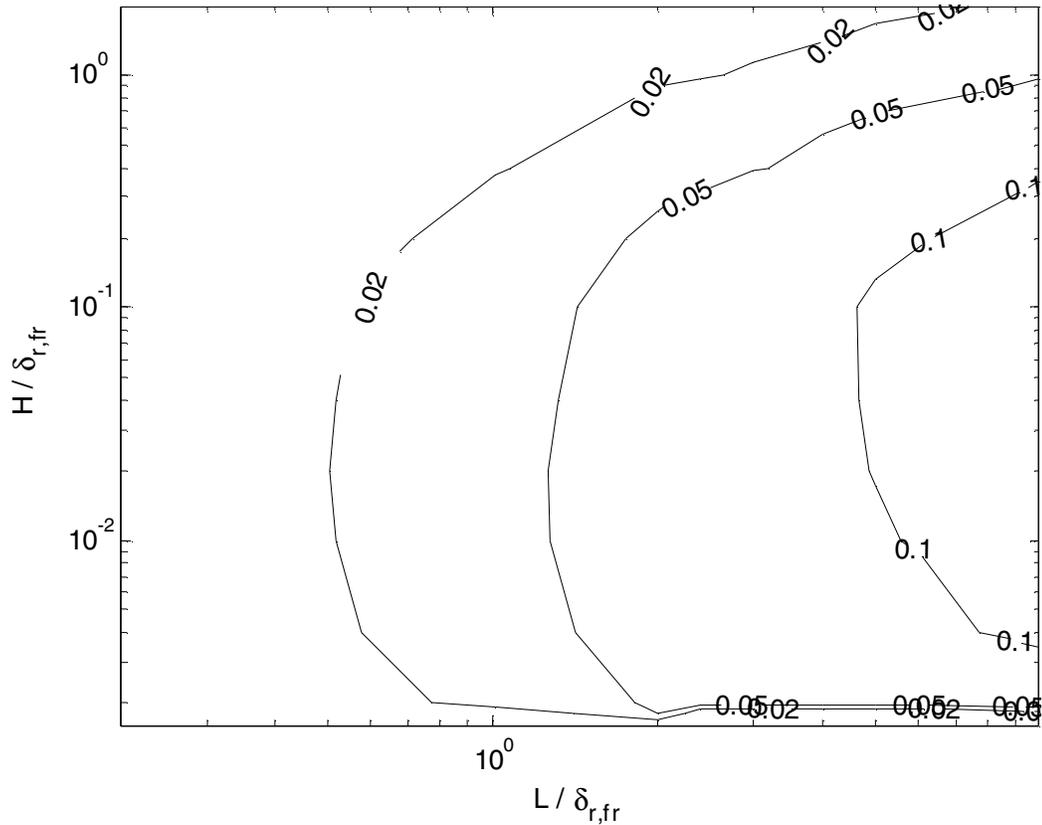
Figure 4-4: Contours of r, the required throat to inlet height ratio to achieve a subsonic-supersonic isentropic flow as a function of combustor configuration.

Once the value of r required to achieve proper subsonic to supersonic transition is determined, the geometry of the micro-nozzle is set and the area-Mach number relationship is used to determine the evolution of M with downstream distance. Knowledge of M and the assumption that the flow in the nozzle is isentropic allows the flow properties T, r, p and U to be determined using the following relationships:

$$T = T_i \left(1 + \frac{\gamma - 1}{2} M^2\right)^{-1} \qquad (4\text{-}3)$$

$$\rho = \rho_i \left(1 + \frac{\gamma-1}{2}M^2\right)^{-1/\gamma-1} \tag{4-4}$$

$$p = p_i \left(1 + \frac{\gamma-1}{2}M^2\right)^{-\gamma/\gamma-1} \tag{4-5}$$

$$u = M\sqrt{\gamma RT} \tag{4-6}$$

The thrust produced per unit width is:

$$T = \dot{m}(u_e - u_i) \tag{4-7}$$

where

$$\dot{m} = \rho_e 2 H u_e \tag{4-8}$$

However, a more appropriate performance metric is thrust-to-weight ratio. To evaluate this, the mass of the thruster is estimated using geometric considerations. The thruster mass per unit width is:

$$m = \rho_{Si}(2H + 3H^2) \tag{4-9}$$

where r_{Si} is the mass density of silicon (2330 kg/m³). The thrust-to-weight ratio becomes:

$$T/W = \frac{T}{mg} \tag{4-10}$$

Another important performance metric is the specific impulse. It is defined as:

$$I_{sp} = \frac{u_e}{g} \tag{4-11}$$

Another important performance characteristic of micro-scale systems is pressure losses. At small scales, wall velocity gradients are large, and these lead to large pressure loss. In order to estimate these losses, we assume that a fully-developped

Poiseuille flow is established in the nozzle. Thus, the relative pressure loss can be evaluated as:

$$\Delta p = \frac{1}{p_0} \int \frac{8\mu(x,T)u(x)}{H(x)^2} dx \qquad (4\text{-}12)$$

where x is the downstream distance, u is the velocity in the nozzle, μ is the temperature dependent viscosity of the gas (which is assumed to be N_2), H(x) is the distance between the nozzle walls, and p_0 is the combustion chamber pressure (1atm).

4.3. Results and discussion

Figure 4-5 is a contour plot of thrust-to-weight ratio as a function of combustor passage height H and passage length L. These dimensions have been normalized by $\delta_{r,fr}$, the flame thickness of a freely propagating flame. The thrust-to-weight ratio T/W has been non-dimensionalized by that of the space shuttle main engine for comparison. This value was evaluated from data found in[55]. The reactants are H_2 and air at an equivalence ratio of 0.5. While air is not a realistic rocket motor oxidizer, this mixture was selected so that the results from the previous part could be re-used.
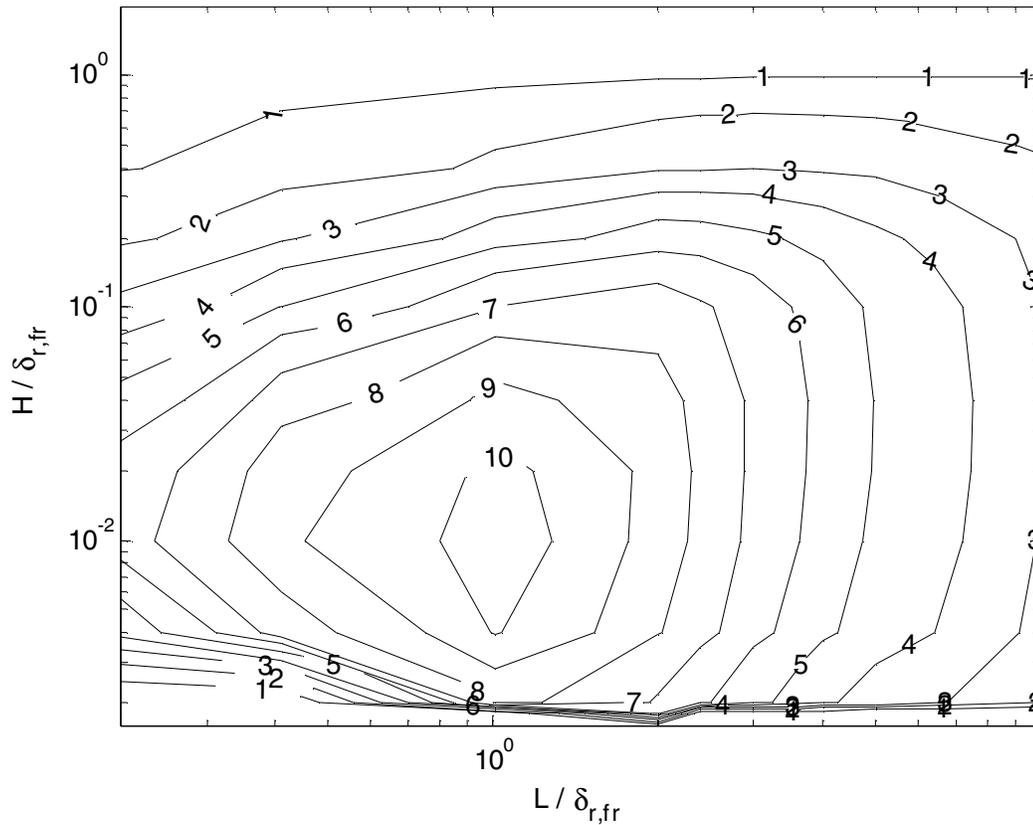
Figure 4-5: Normalized thrust-to-weight ratio as a function of normalized passage height and length.

Just like power density, figure 4-5 suggests that T/W is maximized for a specific configuration of the combustor. The optimum occurs at the same configuration corresponding to optimum power density and illustrates the strong influence combustor configuration can have on a micro-thruster's performance. The figure also suggests that the peak non-dimensional T/W is significantly greater than 1. This indicates that it may be possible to achieve significantly higher T/W using micro-thrusters than can be achieved in macro-scale devices. Since the actual fuel used in the reference engine (i.e. the space shuttle main engine) is high-pressure liquid

hydrogen and oxygen which is much more energetic than the atmospheric pressure H_2-air mixture considered in this study we might expect the maximum value of T/W to be much higher than 10 for realistic rocket propellants. Consequently the benefits of miniaturizing chemical thrusters could be even greater than what is described here.

While thrust-to-weight ratio is an important performance metric, specific impulse is also important as it reflects the efficiency of the combustion process. The solid lines in figure 4-6 show contours of specific impulse as a function of normalized passage height H and length L. The dotted lines are contours of thrust-to weight ratio which are superimposed on the plot for reference. The figure shows that at the optimum configuration with respect to T/W, the specific impulse is on the order of 140s. At large H and L where there is essentially no interaction between the reacting gas and the structure of the combustor, the specific impulse is larger than 180s. This suggests that, just like for the results presented in the previous chapter, it is possible to design micro-thrusters with large thrust-to-weight ratios, but that this comes at the price of specific impulse. However, as mentioned earlier, specific impulse would have been larger had we considered a more realistic oxidized for rockets.
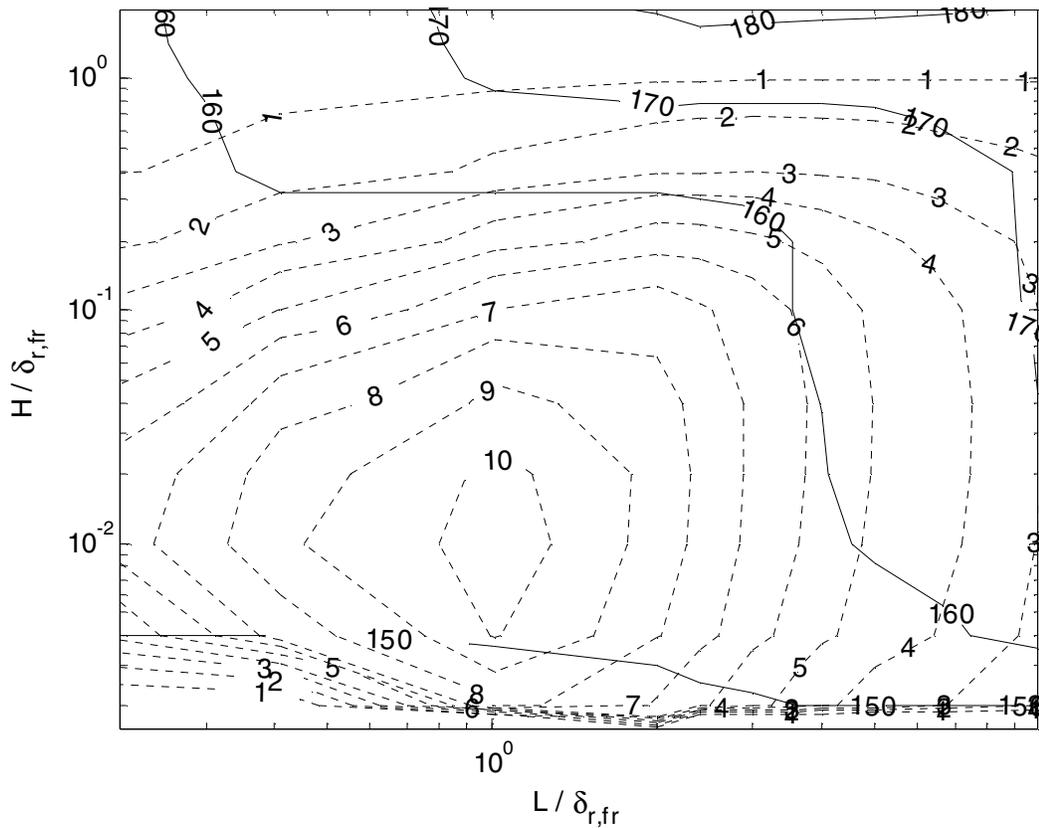
Figure 4-6: Solid lines: Specific impulse as a function of normalized passage height and length; Dotted lines: Normalized thrust-to-weight ratio as a function of normalized passage height and length.

One key limiter of miniaturization in these high-speed devices is pressure drop. Figure 4-7 is a contour plot of normalized pressure drop, defined by equation 4-12, as a function normalized passage height and length. Again, contours of normalized trust-to-weight ratio have been superimposed as dotted lines for the purpose of comparison. As the passage height decreases, the velocity gradient at the wall increases and thus so does the pressure drop. The variation with passage length is more complex. The figure shows that as the length of the combustion chamber

decreases, the conditions at the outlet of the combustor change: The combustion temperature decreases because the degree of conversion of the fuel decreases, and the flow velocity decreases because there is less pre-heating of the mixture via heat recirculation through the combustor structure. This leads to a decrease in Mach number at the outlet of the combustor (or the inlet of the nozzle) with L. Thus, the value of r required to reach sonic conditions at the throat increases, leading to a smaller throat height and larger pressure losses. Therefore, the least amount of pressure drop occurs at the largest passage height and length. As the configuration moves away from this optimum, pressure drop becomes significant. Beyond a normalized pressure drop of 100%, the device becomes totally unviable but this would really occur much earlier. The figure suggests that the range of possible configurations associated with relative pressure drops that are less than 100% is actually quite narrow. This limits the maximum achievable normalized thrust to weight ratio to 5. However the combustion chamber pressure considered in this study is 1atm which is very low for a rocket. Considering a higher pressure would reduce the significance of the pressure losses and expand the range of viable configurations.
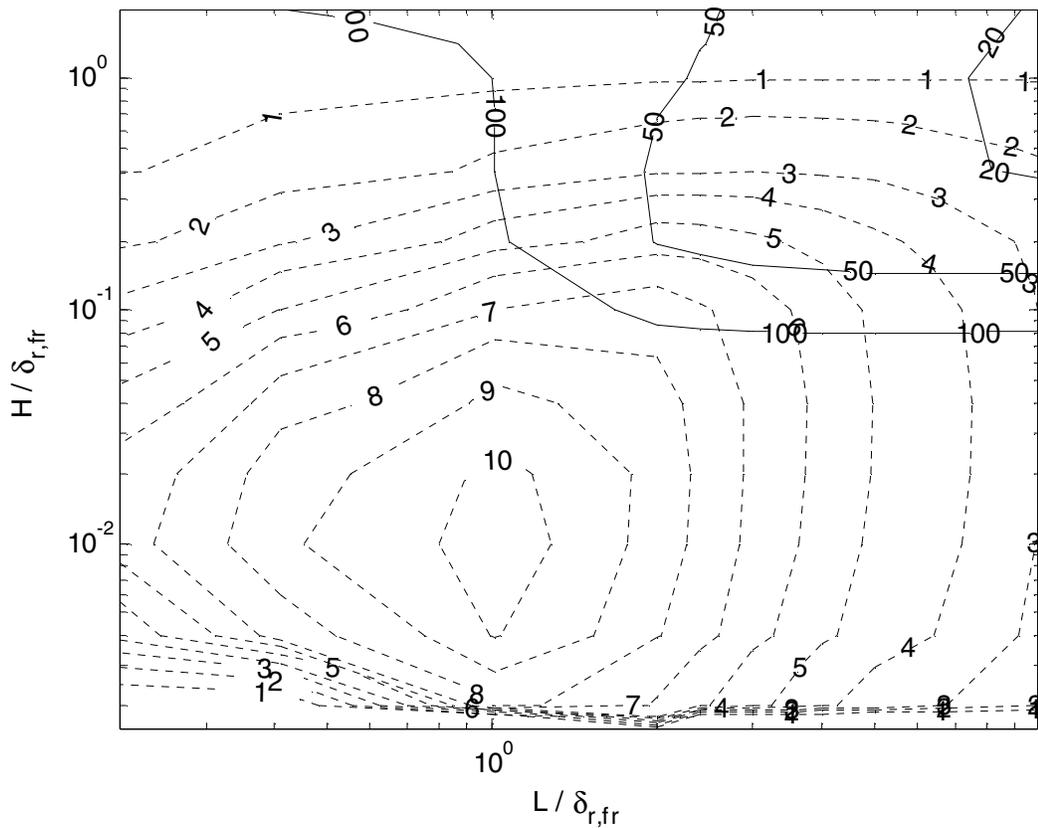
Figure 4-7: Solid lines: Relative pressure drop (in %) as a function of normalized passage height and length; Dotted lines: Normalized thrust-to-weight ratio as a function of normalized passage height and length.

4.4. Conclusions

The performance of hydrogen-air fueled micro-thrusters was investigated by appending a planar, ideal nozzle to the parallel plate micro-combustor geometry investigated in the previous chapter. This simulation took into account heat recirculation within the structure of the combustor. The results suggest that the combustion chamber configuration strongly affects the performance of the micro-

thruster. In particular, there exists a combustion chamber configuration which maximizes thrust-to weight ratio. However, the optimum configuration has low specific impulse and high pressure loss, making it unlikely that the "real" device could actually achieve the predicted T/W and I_{sp}. However, the results suggest that thrust-to-weight ratios much greater than those of macro-scale thrusters could be achievable, provided that good thermal management of the combustion chamber is achieved and that the devices can be operated at high pressures. This demonstrates the potential benefit of miniaturizing chemical thrusters

However, more work is required in order to evaluate the performance of more realistic thrusters. In particular, higher combustion chamber pressures and more realistic propellants ought to be considered. These more realistic thrusters should perform better than the ones described here. In addition, the effect of the thermal coupling between gas and structure of the micro-nozzle itself should be taken into account to obtain more realistic performance estimates.

Nevertheless, this chapter does provide some preliminary insight regarding the design and performance of micro-thrusters and the potential benefits of miniaturizing chemical thrusters. However, maximizing T/W would only be beneficial if the acceleration of the spacecraft considered is the driving design parameter. If, on the other hand, the lifetime/efficiency of the spacecraft is of greater importance, then conventional scale thrusters are more advantageous as they have greater specific impulse. In general, the optimum thruster configuration ultimately depends on the particular application.

Chapter 5: Flame Stability

5.1. Introduction

In the second chapter of this work, numerical and analytical models were developed for flames propagating in micro-channels. They showed that flames stabilized in micro-channels behaved differently than their conventional-scale counterparts: Reaction zones seemed to be broader and burning velocities seemed to be higher than what one would expect for freely propagating flames. It was shown that these behaviors are the result of heat recirculation from the post-flame to the pre-flame through a micro-combustor's structure that becomes more important as the size of the combustor is reduced. Some of the consequences of this behavior were explored in the third and fourth chapters of the thesis, which concentrated on predicting the performance of micro-combustors and micro-chemical thrusters. The flame broadening phenomenon and the increase in burning velocity of the mixture were shown to have a great impact on power density of micro-combustors and the thrust-to-weight ratio of micro-thrusters. Brief mention was also made of the fact that thermal coupling also seemed to widen the stability limits of the flame: Figure 3-2 showed that there seems to be a range of velocities over which stable combustion can be sustained. This observation is consistent with early analytical work which showed that the interaction between a flame and its surroundings can enhance its stability[56]. Subsequent experimental work confirmed this result, and the process was given the name 'Thermally Stabilized Combustion'[57]. This contrasts however with other

analytical theories for freely propagating flames that predict a single value of the burning velocity that is an eigenvalue of the gas-phase problem.

In this chapter, we attempt to improve our understanding of the basic physical mechanisms responsible for the enhancement of flame stability in micro-combustors. This is accomplished by developing a simple analytical model for flame propagation in a narrow channel and comparing its predictions to those obtained using more detailed numerical simulations and experiments. Both steady-state and transient stability are investigated. Note that combustion *instability* associated with the coupling of pressure and heat release oscillations is *not* under consideration here.

5.2. Analytical Model

Figure 5-1 is an idealized representation of a flame stabilized in a micro-channel formed by two closely-spaced parallel plates that extend to infinity in the directions normal to the plane of the drawing. The distance between the plates is H and their thickness t is $H/2$. This ensures that the respective cross-sectional areas for heat conduction in the gas and the structure remain constant as the distance between the plates is varied. The length of the micro-channel is L and the position of the flame from the flow entrance is x_{flame}. Premixed hydrogen fuel and air enter the combustor from the left at an equivalence ratio $\Phi=0.5$, pressure $P=1$ atm and velocity U. Since the plates are semi-infinite, the width of the channel does not have any effect on the problem and it is taken to be unity.
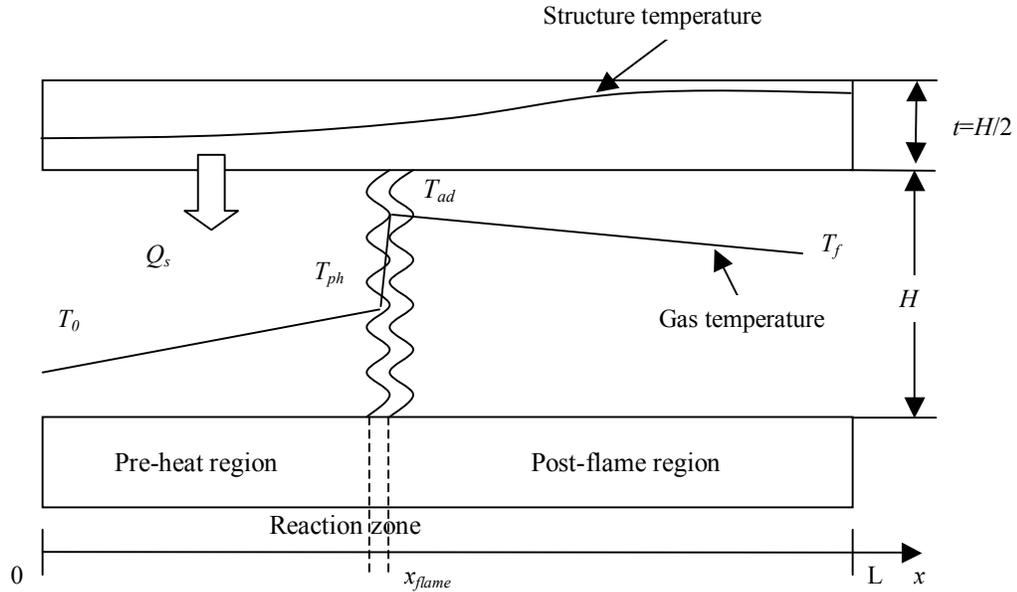
Figure 5-1: Schematic diagram of a parallel plate reactor in which a flame is stabilized showing structure and gas temperatures, the three zones described in the text and the heat flux from the structure to the preheat zone.

A one-dimensional approach is used to model exchange processes in the flow direction. The channel is divided into three parts: the preheat zone, in which the gas temperature is raised from the inlet temperature T_0 to a preheat temperature T_{ph}, the reaction zone in which gas temperature increases sharply from the preheat temperature to the flame temperature T_{ad}, and the post-flame zone, where the gas temperature decreases because heat is lost to the passage walls and possibly to the environment. The final exit temperature is T_f which can be written using energy conservation as

$$T_f = T_{ad} - \frac{Q_{loss}}{\rho H U C_p} = T_{ad} - \frac{Q_{loss}}{M} \qquad (5\text{-}1)$$

where T_{ad} is the adiabatic flame temperature (1680K in this study) and Q_{loss} is the heat loss to the environment per unit width of the plate.

It is possible to represent thermal exchange processes between gases and solid structures using thermal resistance networks[58]. Figure 5-2 shows the network used to represent thermal exchange between the gas, the structure, and the environment in this problem. Note that it is only necessary to represent the upper half of the micro-channel.
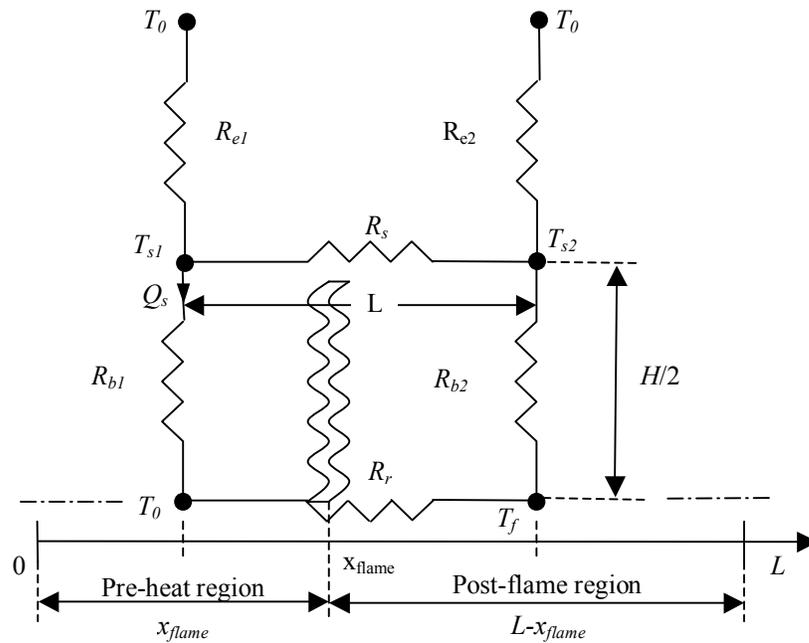
Figure 5-2: Thermal resistance network associated with the flame stabilization problem.

In the network, R_s is the resistance to conductive heat transfer in the combustor structure, R_{b1} and R_{b2} are the resistances to convective heat transfer in the boundary layers in the pre-heat and post-flame regions respectively and, R_{e1} and R_{e2} are the resistances to convective heat transfer from the structure to the environment in the pre-heat and post-flame regions respectively. These resistances can be written as:

$$
\begin{cases}
R_s = \dfrac{L}{k_s \, A_s} = \dfrac{L}{k_s \, t} \\[2mm]
R_r = \dfrac{\delta_r}{k_{g,pre} \, A_g} = \dfrac{\delta_r}{k_s \, H} \\[2mm]
R_{b1} = \dfrac{1}{h_{T,pre} \, A_{pre}} = \dfrac{2 \, H}{Nu \; k_{g,pre} \; x_{flame}} \\[2mm]
R_{b2} = \dfrac{1}{h_{T,post} \, A_{post}} = \dfrac{2 \, H}{Nu \; k_{g,post} \left(L - x_{flame}\right)} \\[2mm]
R_{e1} = \dfrac{1}{h_{T,e} \, A_{pre}} = \dfrac{1}{h_{T,e} \, x_{flame}} \\[2mm]
R_{e2} = \dfrac{1}{h_{T,e} \, A_{pre}} = \dfrac{1}{h_{T,e} \left(L - x_{flame}\right)}
\end{cases}
\tag{5-2}
$$

where k_s, $k_{g,pre}$, and $k_{g,post}$ are respectively the thermal conductivities of the structure, the gas in the pre-heat region, and the gas in the post-flame region. A_s, $A_{g,pre}$, and $A_{g,post}$ are the corresponding cross-sectional areas for conduction, Nu is the Nusselt number for heat transfer between the gas and the structure, and δ_r is the flame thickness.

While it has been shown earlier that δ_r can increase due to structural heat conduction, in this work we assume that δ_r is fixed to 0.5mm – the value for a freely propagating flame. This is justified for two reasons. First, we are most concerned with the position of the flame which is taken to be the middle of the reaction zone in this work. Second, the thermal resistance of the gas column is already so much larger

than that of the structure and boundary layers that it passes a small portion of the total heat flux in the system. As a result, any changes in the thermal resistance of the gas column that arise from changes in the reaction zone thickness should have a negligible impact on the solution of the thermal network problem. Third, flame broadening is not expected to occur at the lengths scales considered here.

The structure temperatures T_{s1} and T_{s2} are computed by performing heat flux balances at the nodes of the thermal resistance network. This leads to:

$$T_{s1} = \frac{T_0 R_L \left(\frac{1}{R_{e1}} + \frac{1}{R_{b1}} + \frac{R_R}{R_s R_{e2}} \right) + T_f \frac{R_R R_L}{R_{b2} R_S}}{1 - \frac{R_R R_L}{R_s^2}} = \frac{T_0 A_1 + T_f B_1}{C} \tag{5-3}$$

$$T_{s2} = \frac{T_0 R_R \left(\frac{1}{R_{e2}} + \frac{R_L}{R_{e1} R_s} + \frac{R_L}{R_{b1} R_s} \right) + T_f \frac{R_R}{R_{b2}}}{1 - \frac{R_R R_L}{R_s^2}} = \frac{T_0 A_2 + T_f B_2}{C} \tag{5-4}$$

where

$$R_R = \frac{1}{\frac{1}{R_{e2}} + \frac{1}{R_{b2}} + \frac{1}{R_s}} \tag{5-5}$$

$$R_L = \frac{1}{\frac{1}{R_{e1}} + \frac{1}{R_{b1}} + \frac{1}{R_s}} \tag{5-6}$$

$$A_1 = \frac{1}{R_{e1}} + \frac{1}{R_{b1}} + \frac{R_R}{R_s R_{e2}} \tag{5-7}$$

$$A_2 = \frac{1}{R_{e2}} + \frac{R_L}{R_{e1} R_s} + \frac{R_L}{R_{b1} R_s} \tag{5-8}$$

$$B_1 = \frac{R_R R_L}{R_{b2} R_S} \tag{5-9}$$

$$B_2 = \frac{R_R}{R_{b2}} \tag{5-10}$$

$$C = 1 - \frac{R_R R_L}{R_s^2} \qquad (5\text{-}11)$$

The heat loss to the environment is written as:

$$Q_{loss} = 2\, h_{T,e} \left[(T_{s1} - T_0) x_{flame} + (T_{s2} - T_0)(L - x_{flame}) \right] \qquad (5\text{-}12)$$

where $h_{T,e}$ is the heat transfer coefficient between the structure and the environment.

We now have four equations (1, 3, 4 and 12) with 4 unknowns (T_f, T_{s1}, T_{s2}, and Q_{loss}).

A closed form solution can be found for T_f:

$$T_f = \frac{T_{ad} - T_0\, A/M}{1 + B/M} \qquad (5\text{-}13)$$

where

$$A = \frac{A_1}{CR_{e1}} + \frac{A_2}{CR_{e2}} - \frac{1}{R_{e1}} - \frac{1}{R_{e2}} \qquad (5\text{-}14)$$

$$B = \frac{B_1}{CR_{e1}} + \frac{B_2}{CR_{e2}} \qquad (5\text{-}15)$$

Note that T_f depends on x_{flame} through the different resistances R_{e1}, R_{e2}, R_{b1} and R_{b2}. Now that T_f is known, T_{s1}, T_{s2} and Q_{loss} can subsequently be evaluated using equations 5-3, 5-4 and 5-12. An additional constraint is imposed by requiring that the heat generated by combustion must be higher than the heat loss to the environment. This is written:

$$\rho S_L C_p H(T_f - T_0) > Q_{loss} \qquad (5\text{-}16)$$

The net heat flux from the post-flame to the pre-heat zone is determined using:

$$Q_s = 2\frac{T_{s1} - T_0}{R_{b1}} + \frac{T_f - T_0}{R_r} \qquad (5\text{-}17)$$

Assuming that heat transfer from the structure to the pre-heat zone occurs uniformly, the heat flux per unit area can be written as:

$$q_s = \frac{Q_s}{x_{flame}}$$ (5-18)

If the heat flux is uniform, it can be shown that the temperature rises linearly in the preheat region[59] so

$$T_{ph} = T_0 + \frac{dT}{dx} x_{flame}$$ (5-19)

where

$$\frac{dT}{dx} = \frac{q_s}{\rho\, U\, C_p\, H}$$ (5-20)

Heat recirculation increases the unburned (or preheat) gas temperature by transferring a certain amount of enthalpy from the post-flame to the pre-heat zone. This, in turn, increases the burning velocity of the mixture. At the same time, however, heat loss to the environment decreases the flame temperature and thus the burning rate. To account for these dependencies, we use the following simplified expression for the flame speed that includes the effects of pre-heating[60]:

$$S_L \propto \overline{T}^{0.375} T_{ph} T_f^{-n_r/2} \exp\left(-E_A \middle/ 2RT_f\right)$$ (5-21)

where

$$\overline{T} = \frac{T_{ph} + T_f}{2}$$ (5-22)

The global order of the reaction, n_r, is 3 for the hydrogen-air reaction considered here and the activation energy E_A is 12.5kcal/mole[61].

In order to investigate the stability limits of the combustor, we look for values of the flame position x_{flame} that lead to burning velocities that are equal to the inlet velocity. Figure 5-3 shows a sample plot of non-dimensional burning velocity for hydrogen fuel at Φ=0.5 computed using equation (5-21) as a function of non-dimensional flame position for H=0.5mm, L=1cm, U=1.8m/s, $h_{T,e}$=50 W/m^{2}K and for three different values of the thermal conductivity of the structure (0 W/mK, 5 W/mK, and 50 W/mK). In the figure, the flame position is non-dimensionalized by the combustor length and the flame speed is non-dimensionalized by the speed of a freely propagating flame – i.e. one that propagates without exchanging heat with the structure (S$_{L,fr}$=0.9 m/s).
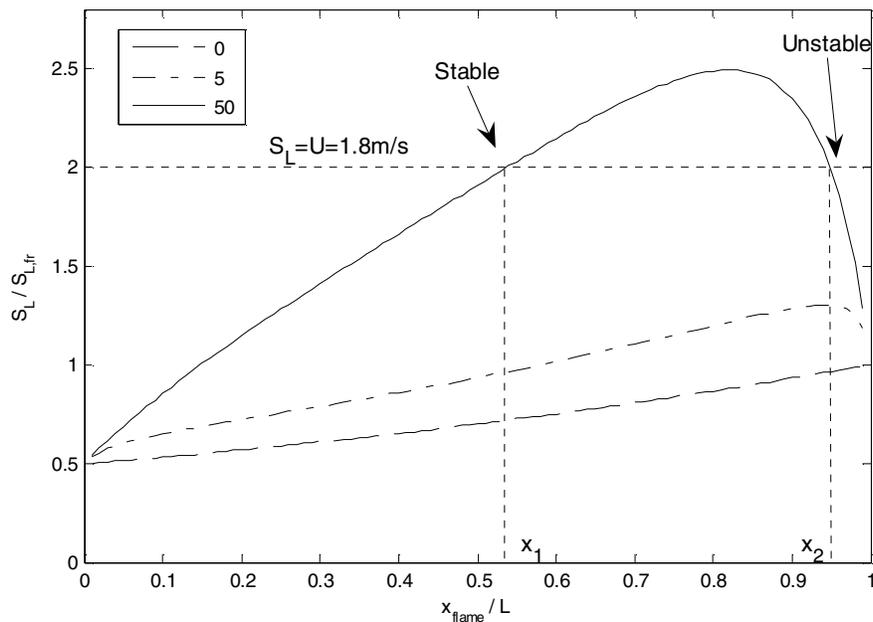
Figure 5-3: Burning velocity as a function of flame position for different values of the thermal conductivity of the structure in W/mK. The families of curves correspond to solutions of the thermal network where h_{Te}=50 W/m^{2}K and U=1.8 m/s.

Figure 5-3 shows that if the thermal conductivity of the structure is high enough, the horizontal dashed line corresponding to the inlet velocity of 1.8 m/s intersects the plot of S_L vs. x_{flame} in two places indicating that two solutions for the flame position are possible. Of these, only the upstream one is stable: This can be seen by realizing that if x_{flame} increases at constant U, the burning velocity increases. Since the burning velocity now exceeds the inlet velocity U, the flame tends to move upstream thereby returning to its original position. Similar lines of reasoning show that the upstream solution is also stable if x_{flame} decreases at constant U, and that the downstream solution is unstable. It should be noted that this stabilization mechanism is similar to that found in Bunsen burner flames[62]. Figure 5-3 also shows that there is a minimum threshold value for the structure thermal conductivity below which no solution is possible. This illustrates the stabilizing role played by structural heat conduction. When the thermal conductivity of the structure is zero and in the absence of heat loss, the non-dimensional flame speed is 1 and the only possible inlet velocity is the freely propagating flame speed. This is consistent with earlier theories for flame propagation that do not account for heat transfer to the structure.

While the behavior described above is observed for inlet velocities larger than the freely propagating flame speed $S_{L,fr}$, a rather different behavior is observed at small velocities. This is because as the inlet velocity is reduced the importance of heat loss becomes more significant. Figure 5-4 is similar to Figure 5-3 in that it shows a sample plot of non-dimensional burning velocity as a function of non-dimensional flame position for H=0.5mm, L=1cm, $h_{T,e}$=50 W/m^{2}K and for three different values of

105

the thermal conductivity of the structure (0 W/mK, 5 W/mK, and 50 W/mK). However the inlet velocity considered is now 0.8m/s, compared to 1.8m/s in Figure 5-3.
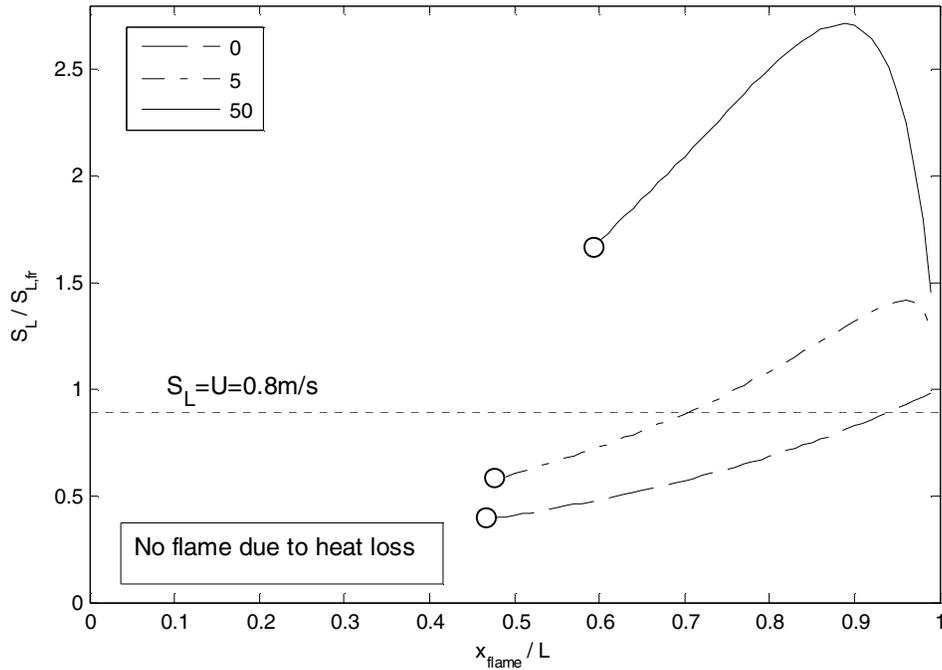
Figure 5-4: Burning velocity as a function of flame position for different values of the thermal conductivity of the structure. The families of curves correspond to solutions of the thermal network where h_{Te}=50 W/m^{2}K and U=0.8 m/s.

Figure 5-4 shows that there is a domain of x_{flame} for which no solutions of the set of equations described above is possible because of the heat loss constraint expressed in equation (5-16). For small values of x_{flame}, there is a large part of the structure downstream the flame and whose temperature is relatively high. Thus heat loss is significant. The figure also shows however that a stable solution does exist if the

thermal conductivity of the structure is small (0 or 5 W/mK). This contrasts with the sample case described above where the inlet velocity is high.

Finally, the degree of heat recirculation is controlled in this work by varying the thermal conductivity of the structure. The reason that thermal conductivity is chosen as the design parameter is that it is convenient both for understanding how the choice of combustor structural material affects flame stability and for comparing our results to those of others. However, it should be reiterated that this is also somewhat misleading as the degree of heat recirculation also depends on the relative thickness of the structural material to the gas column. As a result, the *conductance* – which is the product of the thermal conductivity and the cross-sectional area for conduction in the structure – is a more physically appropriate parameter to vary in order to understand the effect of heat conduction in the structure on the stability of the flame.

5.3. Numerical Model

The numerical model introduced in Chapter 2 of the thesis can be used to check the predictions of the analytical model regarding steady-state stability. In addition the transient capability of the code allows the study of unsteady stability, i.e. the response of the flame to external time-dependant perturbations. For the purposes of this analysis, flame position in the numerical model is defined as the axial position when the H radical mass fraction peaks. This is justified by the fact that the presence of a large H radical concentration typically indicates that combustion is taking place within the mixture.

5.4. Steady Stability: Results and Discussion

5.4.1. Analytical model results

Figure 5-5 shows the evolution of the normalized flame position as a function of the normalized inlet velocity computed using the analytical model presented in section 5.2.. In the figure, the flame position is non-dimensionalized by the combustor length L and the burning velocity is non-dimensionalized by the freely propagating flame speed $S_{L,fr}$=0.9 m/s.
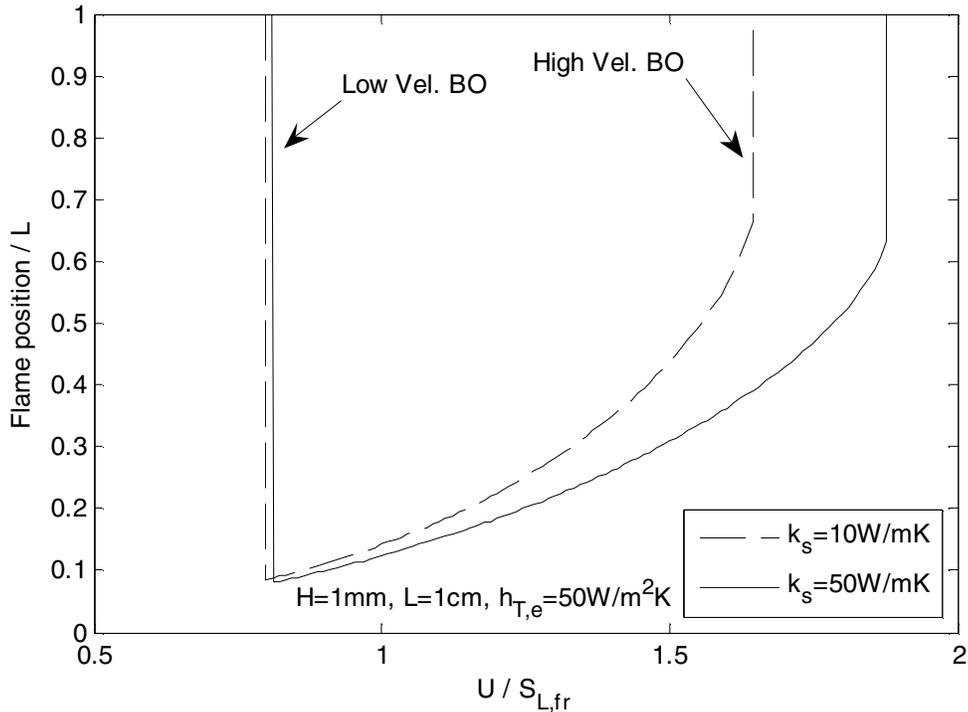
Figure 5-5: Flame position as a function of inlet velocity for different values of the thermal conductivity of the structure computed using the analytical model. The fuel considered is hydrogen at Φ=0.5.

The results in the figure correspond to H=1mm, L=1cm and $h_{T,e}$=50W/m^{2}K and to two different values of the thermal conductivity of the structure (10 W/mK and 50 W/mK). The figure shows that as the inlet velocity increases, the flame monotonously moves farther downstream the combustor, as intuitively expected. The U-shaped curves show that there are two stability limits corresponding to high and low-velocity blow-off. The high velocity blow-off limit occurs when heat recirculation through the structure is unable to provide adequate preheating of the mixture to yield a burning velocity equal to the inlet velocity.

The low velocity blow-off limit is a consequence of the fact that the total heat release in the combustor is directly proportional to the inlet velocity whereas the heat loss to the environment scales with the structure temperature which remains approximately constant as the inlet velocity is reduced. As a result, reducing the inlet velocity U reduces the amount of heat available for pre-heating and this, in turn, reduces the burning velocity. At some point, U exceeds the burning velocity for all possible flame positions and the flame blows off.

Figure 5-5 also illustrates the effect of changing k_s, the thermal conductivity of the structure. Increasing k_s shifts the stability limits to the right or to higher velocities. This makes sense because a larger structure thermal conductivity allows for greater heat recirculation from the post-flame to the pre-flame and thus facilitates the pre-heat of incoming reactants. This observation is consistent with the effect of k_s described in Chapter 2 of this work. However, a higher structural thermal conductivity also provides less thermal insulation by allowing less structure temperature to reach a high temperature, thus increasing heat loss to the environment and causing the flame's low velocity blow-off limit to also shift to higher velocities.

Figure 5-6 illustrates the general effect of structural thermal conductivity on the stability limits of the flame.
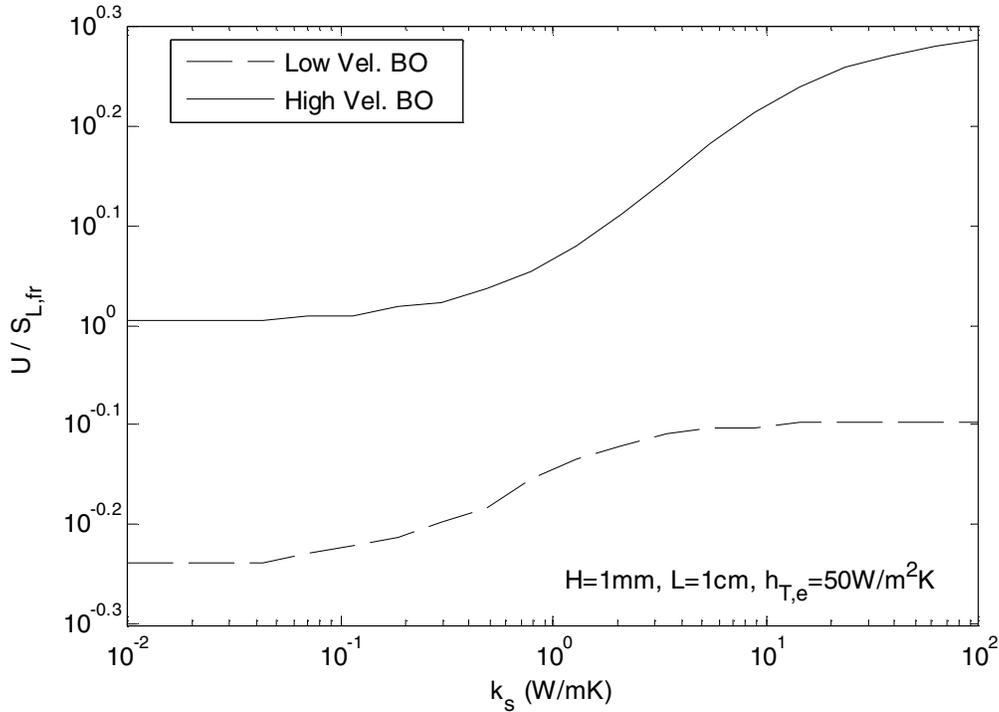
Figure 5-6: Effect of the thermal conductivity of the structure on the stability limits of the flame for _H_=1mm and _L_=1cm computed using the analytical model.

The figure shows that for the reasons identified above increasing the thermal conductivity of the structure shifts both the high and low-velocity blow-off limits to higher velocities. The change in burning velocity shows a limit-cycle behavior as k_s becomes very large or very small. The explanation of this behavior is similar to that of Figure 2-7: At large thermal conductivities of the structure, thermal feedback from post-flame to pre-flame becomes limited by convective heat transfer from gas to the

structure, i.e. by resistances R_{b1} and R_{b2} in figure 5-2. Conversely, for small k_s there is no more thermal feedback through the structure and the behavior of the flame is governed entirely by heat loss to the environment.

Figure 5-7 illustrates the effect of reducing the length of the combustor on the low and high-velocity stability limits.
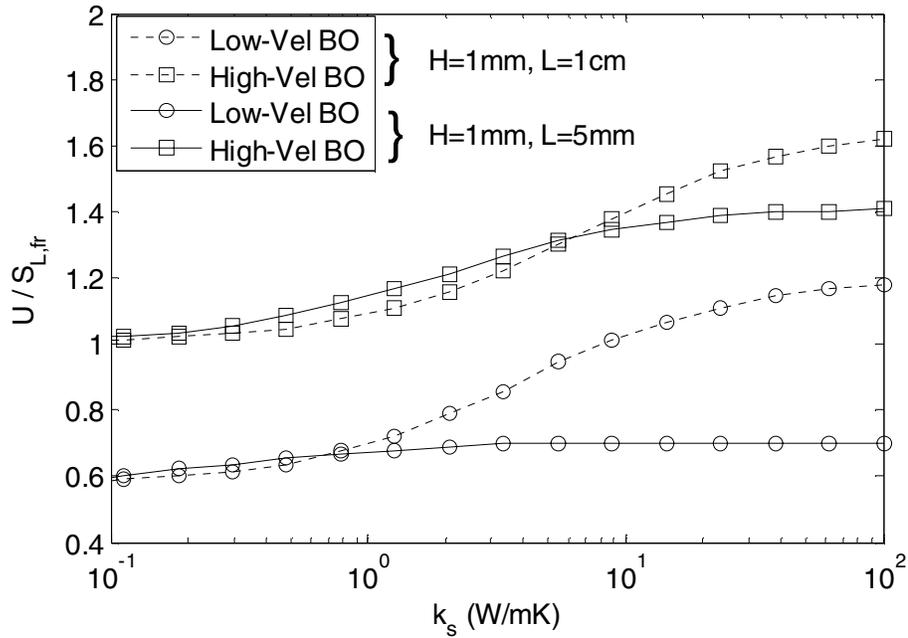
Figure 5-7: Effect of combustor length on the stability limits of the flame computed using the analytical model.

It shows that decreasing the length of the combustor shifts both blow-off limits to lower velocities when the thermal conductivity of the structure is relatively high. This makes sense because decreasing the combustor's length reduces the passage length available for preheat. When the thermal conductivity of the structure is relatively low, heat recirculation is less important and heat loss is more important as

the structure becomes a heat sink for the flame. A longer structure increases heat loss to the environment so decreasing the structure's length reduces heat loss and raises the blow-off limits.

Figure 5-8 illustrates the effect of combustor height on the stability limits of the flame. It shows that decreasing the height of the combustor raises both stability limits. A smaller gap between the plates enhances thermal coupling and preheating of the mixture, thereby increasing the high-velocity blow-off limit. On the other side, a smaller gap also increases the relative importance of heat loss to the environment and as a consequence the minimum velocity required to obtain a stable flame, or the low-velocity blow-off limit, also increases.
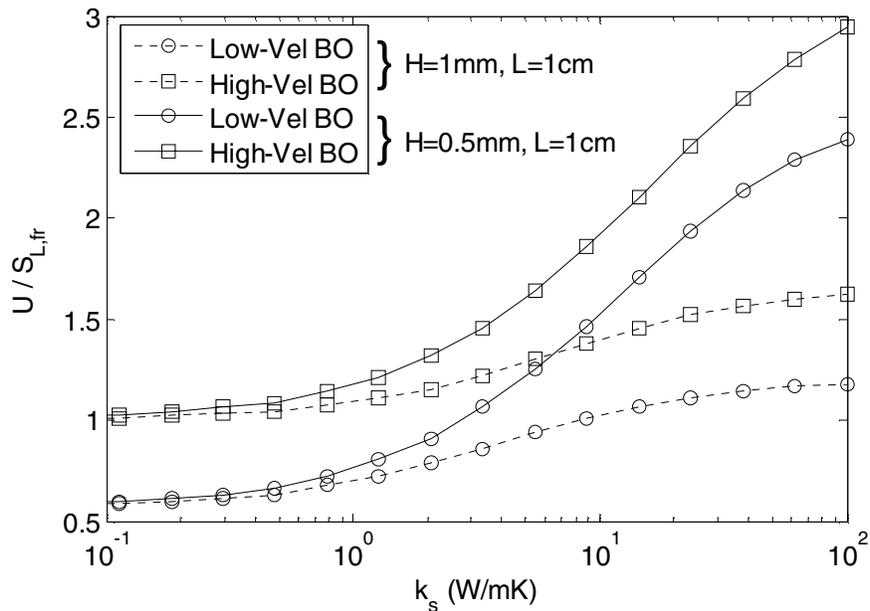
Figure 5-8: Effect of combustor height on the stability limits of the flame computed using the analytical model.

5.4.2. Numerical model results

Figure 5-9 is similar to figure 5-5, except that the curves were generated using the 1D numerical model described earlier. The conditions considered are the same as in the analytical model (H=1mm, L=1cm, $h_{T,e}$=50W/m^{2}K, k_s=10 W/mK or 50 W/mK)
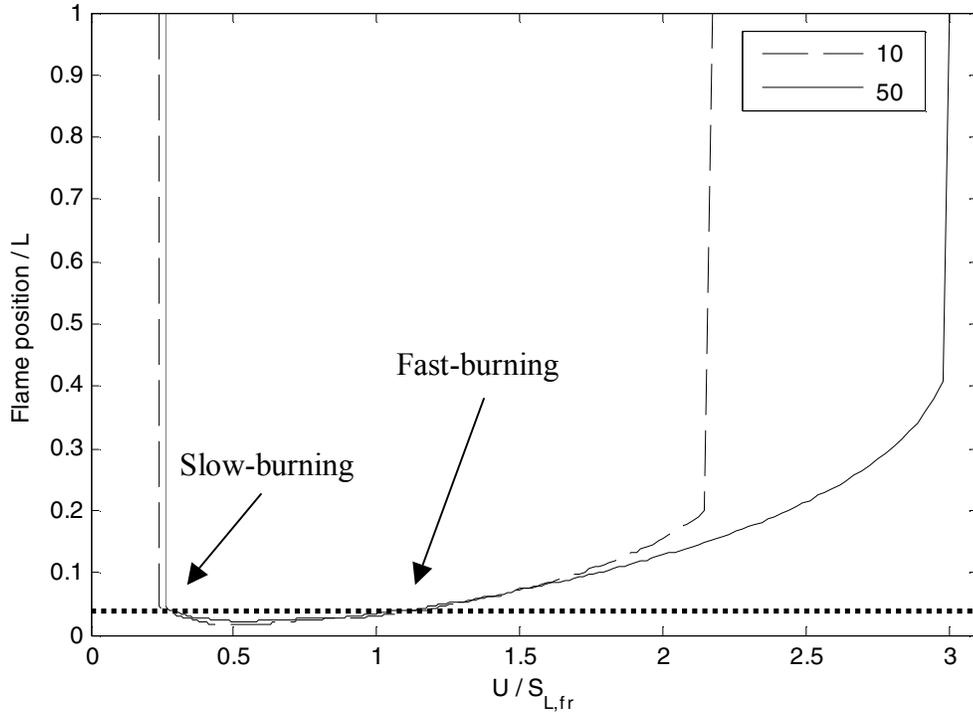

Figure 5-9: Flame position as a function of inlet velocity for different values of the thermal conductivity of the structure computed using the numerical model.

The figure shows qualitative behaviors that are similar to those predicted by the simple analytical model. Both the model and the simulation predict similar shaped curves that shift in a similar way when the thermal conductivity of the structure is increased. However, there is a discrepancy near the low-velocity blow-off limit

113

where the numerical model shows that the flame position increases slightly as U decreases and approaches the low-velocity blow-off limit. This indicates that there are two distinct values of the inlet velocity U that are associated with a single flame position, as illustrated in figure 5-9. These two flame regimes will be called the "fast-burning" and "slow-burning" regimes, in order to be consistent with the work of other researchers[63]. This behavior is not observed in the analytical model which predicts a single value for the burning velocity at each flame position. This value corresponds to the fast burning regime.

Since figure 5-9 was generated using the numerical simulation, temperature profiles in the channel are available. Figure 5-10 shows gas and structure temperatures non-dimensionalized by the adiabatic flame temperature of the mixture (1646K) as a function of non-dimensional downstream distance x/L.
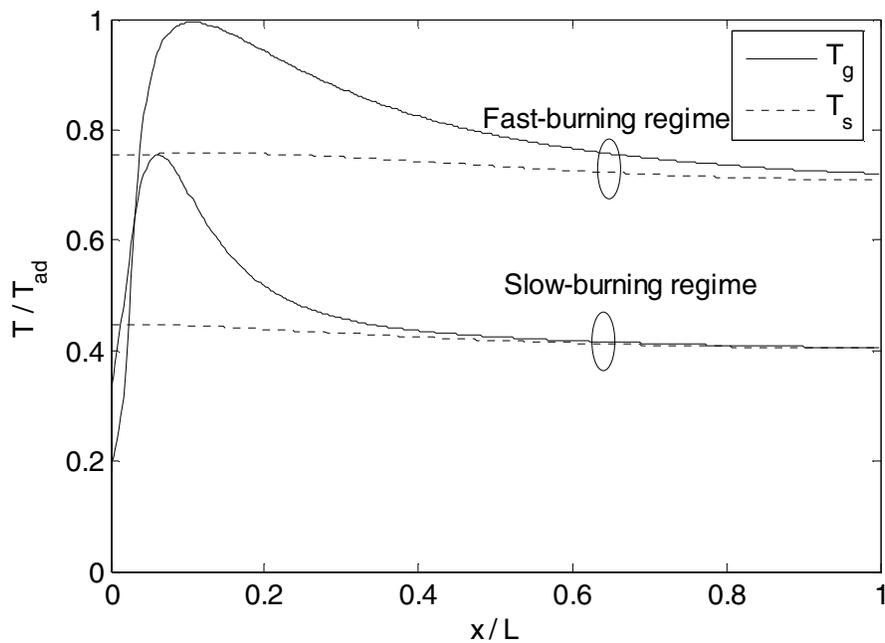
Figure 5-10: Gas and structure temperature profiles in the fast-burning and slow-burning regimes identified above.

The figure shows that both gas and structure temperatures are much higher in the fast-burning regime than in the slow-burning regime. This is a because the inlet velocity of the fast-burning regime is much higher than that of the slow-burning regime. This, in turn, means that heat loss to the environment is less significant in comparison to the overall heat release rate.

Figure 5-11 illustrates the fundamental difference between the fast and slow burning regimes. It is a plot of the axial temperature gradient in the structure non-dimensionalized by an arbitrary reference temperature gradient $(T_{ad}-T_0)/L$.
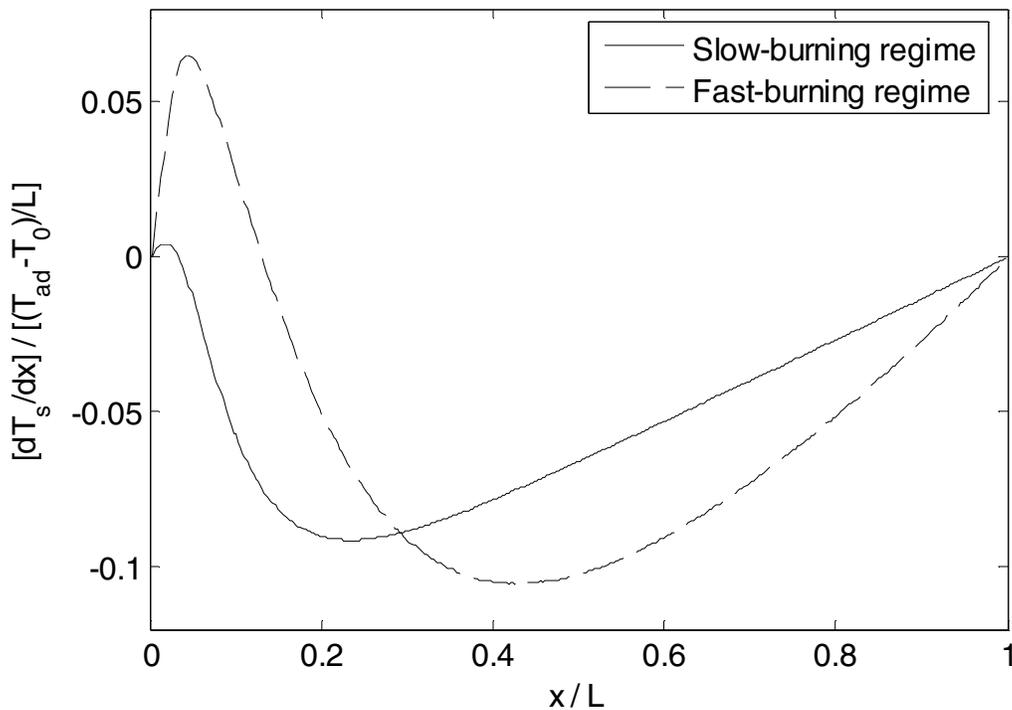
Figure 5-11: Profile of normalized structural temperature gradient for the fast-burning and slow-burning regimes.

The figure shows that the temperature gradient in the structure is positive over a much larger portion of the channel in the fast burning regime compared to the slow-burning regime. This shows that more heat is transferred to the pre-heat zone of the flame in the fast burning regime, and this leads to an increased burning velocity. Thus, the main difference between the two regimes is the degree of thermal feedback upstream through the structure. This feedback is small to non-existent in the slow burning regime and considerably larger in the fast burning regime. These observations are consistent with those made by other researchers who considered moving flames as opposed to stationary flames[64].

Figure 5-12 compares the influence of the structure thermal conductivity on the stability of the flame computed using the analytical model and the numerical simulation for *H*=1mm and *L*=1cm. While the stability limits predicted by the numerical simulation are much wider than those predicted by the analytical mode, the qualitative behaviors are similar. This indicates that the basic physical processes represented in the analytical model are the principal ones governing flame stability at the micro-scale. Furthermore, the discrepancy between the model and the simulation occurs in a direction that should be expected: The distributed nature of the heat transfer between the gas and the structure captured in the numerical simulation should increase thermal coupling between the gas and the structure and lead to greater pre-heating of the reactant mixture than would be possible via the single-zone heat transfer processes included in the analytical model. Therefore, one would expect the numerical simulation to produce wider stability limits than predicted by the analytical model.
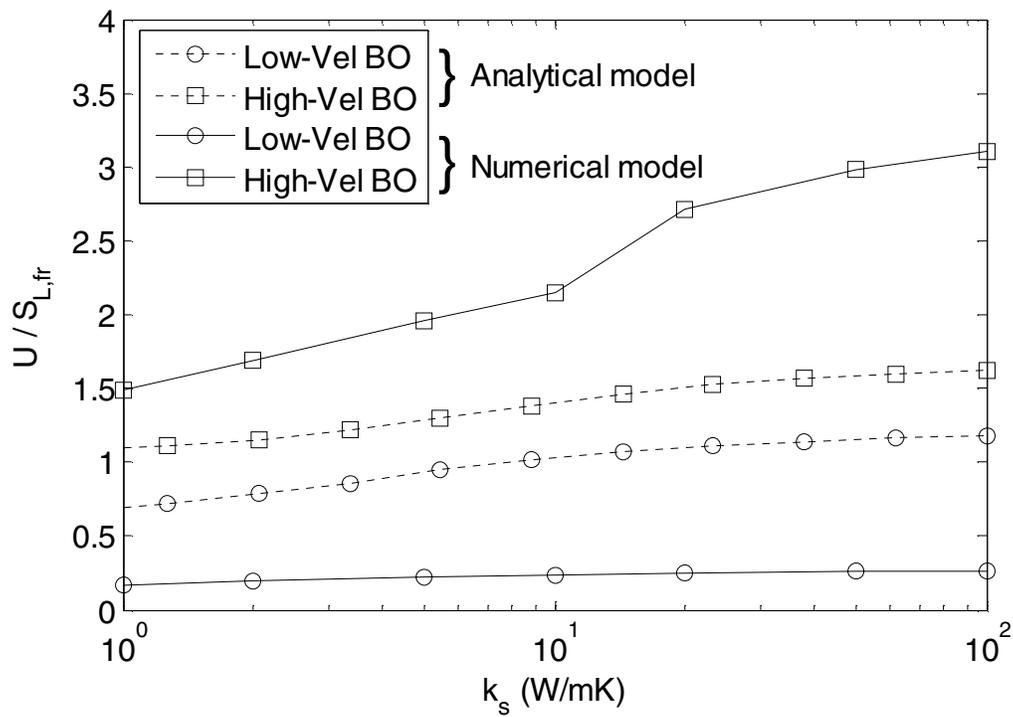
Figure 5-12: Comparison of the results of the analytical and numerical approaches: effect of thermal conductivity for *H*=1cm and *L*=1cm.

Figure 5-13 illustrates the effect of changing the length of the combustor on the stability limits of the flame computed using the numerical simulations. The results are also qualitatively similar to the predictions of the analytical model presented in figure 5-7.
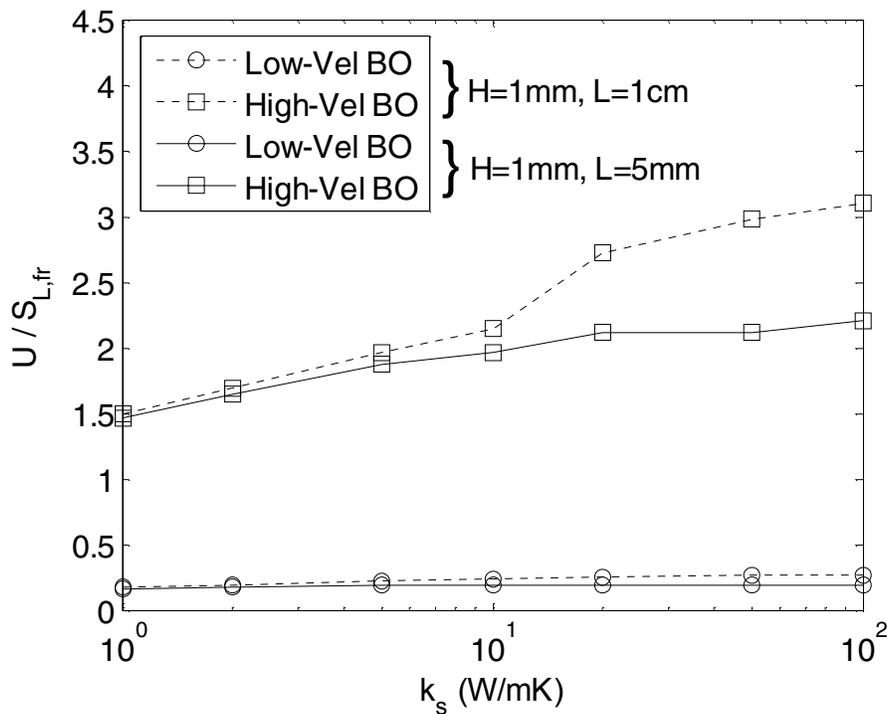
Figure 5-13: Effect of combustor length on the stability limits of the flame computed using the numerical model.

Figure 5-14 illustrates the effect of reducing the height of the combustor on the stability limits of the flame computed using the numerical model. Again, the numerical model is in qualitative agreement with the predictions of the analytical model presented in figure 5-8 although the low-velocity blow off limit computed using the numerical simulation appears to be much less sensitive to the thermal conductivity of the structure.
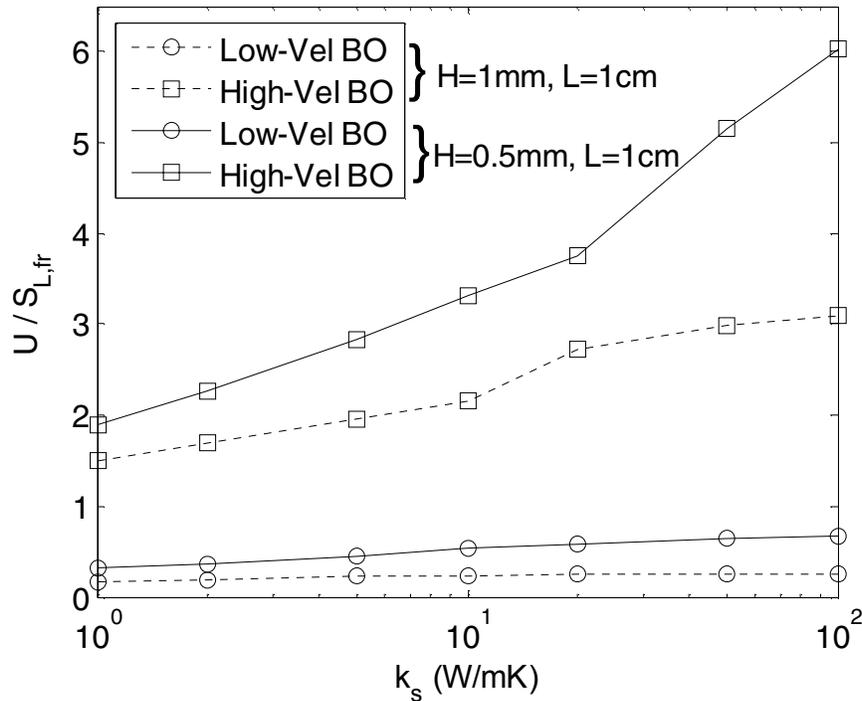
Figure 5-14: Effect of combustor height on the stability limits of the flame computed using the numerical model.

5.4.3. Comparison to results of other researchers

The topic of flame stabilization via structural heat recirculation has also been investigated by Norton and Vlachos[65] recently. They considered a propane-air flame stabilized in a channel and investigated effects of the thermal conductivity of the structure and heat loss to the environment on the stability limits of the flame. Their approach was to use a two-dimensional CFD simulation with one-step chemistry and fluid-structure interaction. Their predictions for the flame position as a function of inlet velocity for structures with different thermal conductivities are presented in figure 5-15. The shapes of the curves and their trends with increasing the thermal

conductivity of the structure are very similar to our predictions made using the analytical model (figure 5-5) and the 1D numerical simulation (figure 5-9).
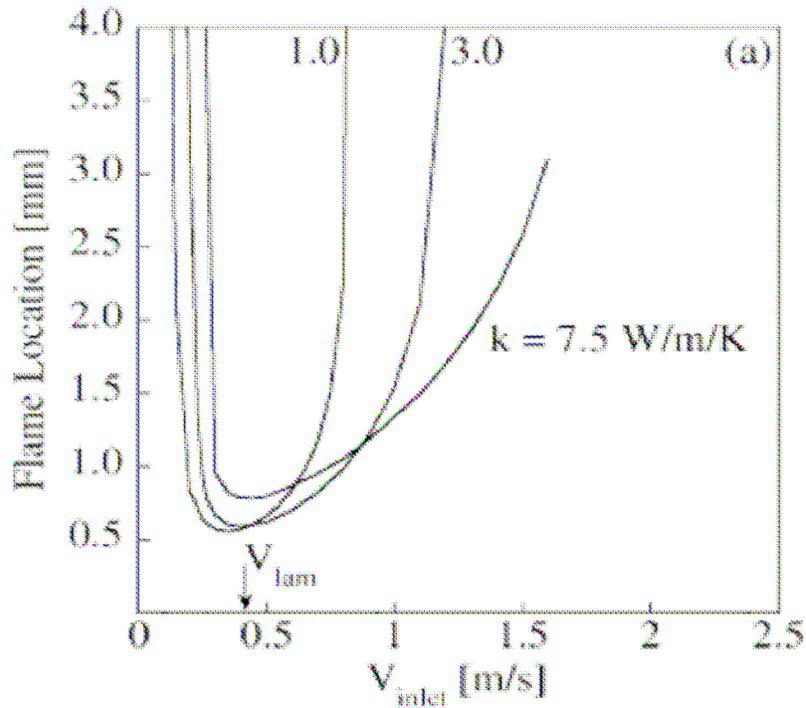
Figure 5-15: Flame position as a function of inlet velocity for different values of the thermal conductivity of the structure from[15]

Their predictions of how thermal conductivity of the structure generally influences the stability limits (presented in figure 5-16) are also similar to the predictions of the analytical model (figure 5-6) and the 1D numerical simulation (figure 5-12).
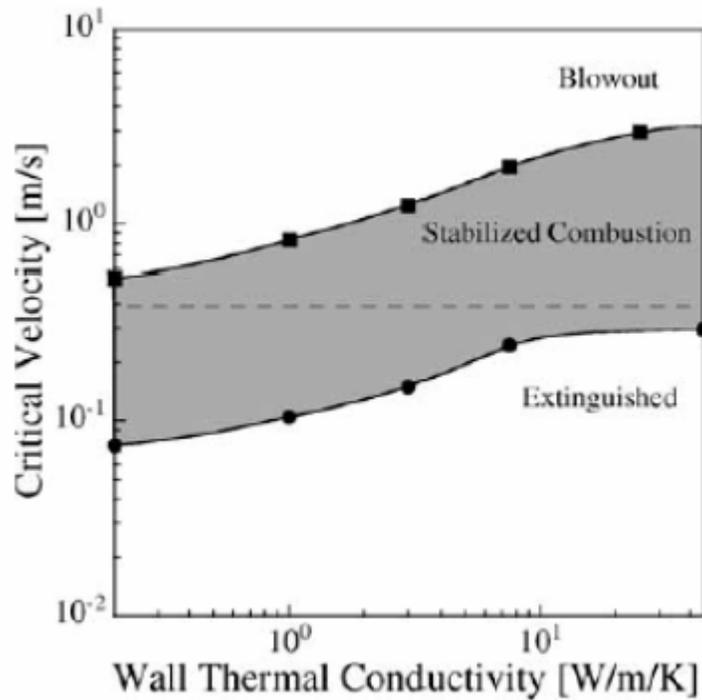
Figure 5-16: Effect of the thermal conductivity of the structure on the stability limits of the flame from[15]

This gives us confidence that the basic physical processes represented in the simple analytical model are the ones that govern micro-scale combustion. This also demonstrates the vale of simple modeling in developing fundamental understanding of complex combustion processes. In addition, and as a practical matter, it should be noted that Figure 5-5 was generated on a desktop computer (Pentium IV processor, 2.4GHz, 512Mb RAM) in less than 10 seconds, whereas the results of the 2D simulations shown in Figure 5-15 required lengthy computations on a PC cluster consisting of 58 Pentium IV processors and 58 GB of RAM. Therefore, considering the gross disparity in complexity between the two approaches, the analytical model

predicts flame stability remarkably well and has the advantage of being fast enough to be used as a tool to investigate wide parameter spaces as part of the preliminary design process.

5.4.4. Experimental validation

A simple burner consisting of two parallel silicon plates between which a flame is stabilized is used to test the predictions of the model and simulation. The burner and diagnostic technique have been developed by Scott Heatwole[66, 67] and Anand Veeraragavan and only a brief description is provided here. Figure 5-17 is a 3D drawing of the silicon-walled micro-burner. Methane is the fuel, air is the oxidizer, and the equivalence ratio is 0.5. The distance between the parallel plates is 2 mm, the thickness of the plates is 500 μm and their length is 55 mm.

The silicon walls of the micro-burner are transparent in the infrared region near well known absorption features of CH_4 and CO_2. As a result, it is possible to interrogate the flow non-intrusively for these species by passing the beam from a Fourier Transform Infra-Red (FTIR) spectrometer through the walls of the burner. Methane and CO_2 spectra are collected from which flame position and flame temperature are computed using methods reported elsewhere[68, 69]. An infrared camera is also used to measure the surface temperature of the parallel plates. This enables the determination of the surface temperature, an estimate of heat loss to the environment via a published correlation for natural convection from a vertically oriented plate, and provides a visual indication of the position of the flame.
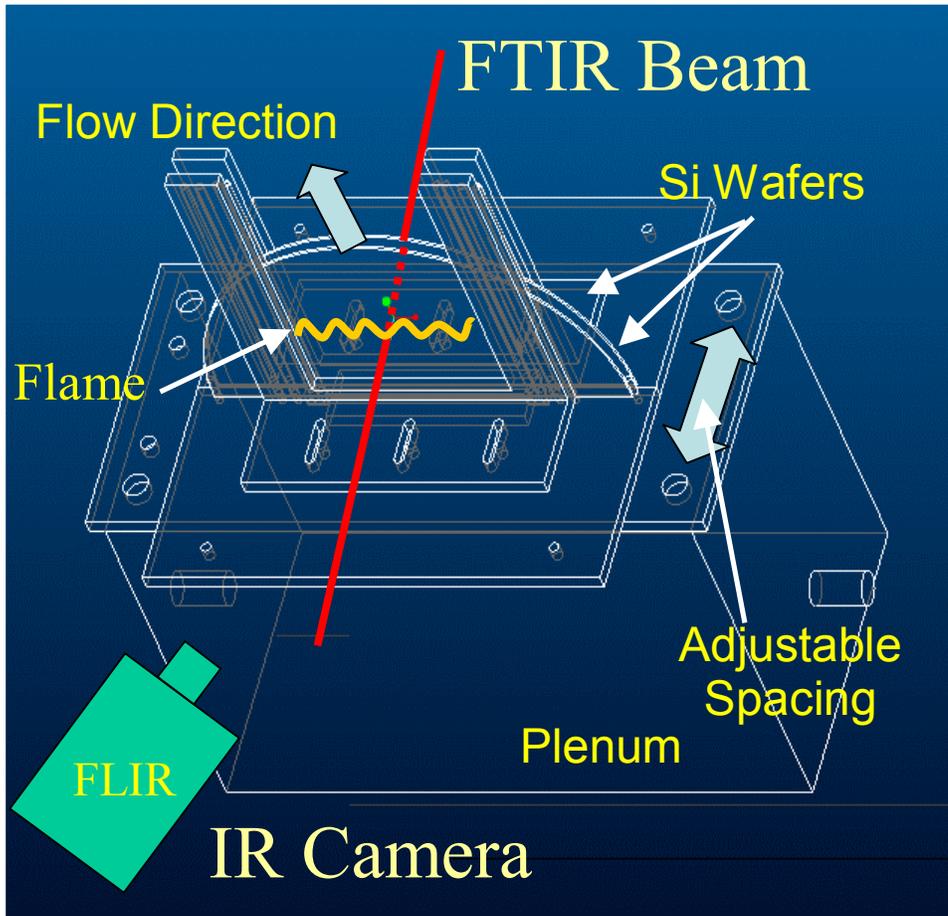
Figure 5-17: Schematic diagram of the silicon-walled micro-burner.

Figure 5-18 is a series of infrared images of the silicon plate surface temperature for different values of the inlet velocity.

U=1.1m/s   U=1.2m/s

U=1.25m/s   U=1.275m/s

247.8°C

<48.4°C
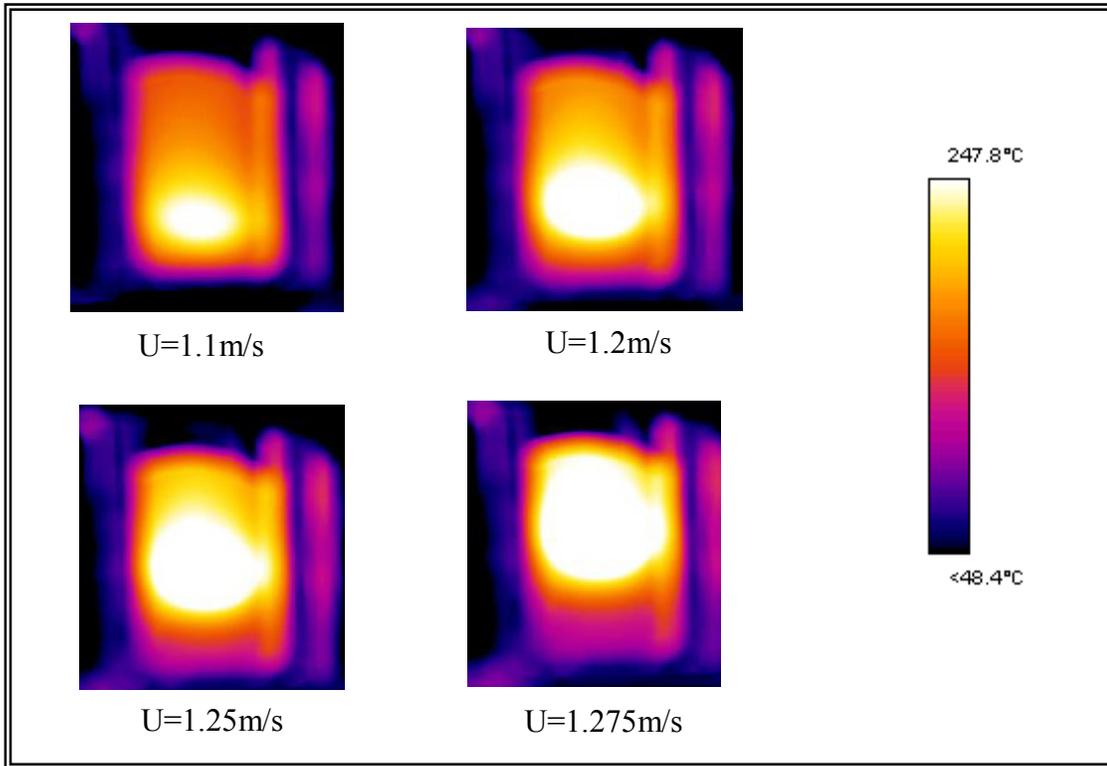
Figure 5-18: Infrared images of the plates for different values of the inlet velocity of the fuel-air mixture. The reactants are methane and air at Φ=0.5.

First, all of the flow velocities are in excess of 1m/s whereas the laminar flame speed for Methane-Air at an equivalence ratio of 0.5 is 0.4m/s. This is a strong indication that burning velocity enhancement via heat recirculation through the silicon plates is occurring as predicted in Chapter 2. Second, the images show that there is a range of inlet velocities for which a stable flame is obtained between the plates. This demonstrates the shows the enhancement in steady-state flame stability discussed earlier in this chapter.

Two methods are used to measure the flame position in the experiment. The first uses the FTIR to obtain species concentration profiles where the flame location is defined as the position where the methane concentration drops sharply. The second uses the infrared images of the structure temperature where the flame position is taken to be the point where the structure temperature is reaches a maximum.

Figure 5-19 compares the dependence of flame location on inlet velocity determined using analytical, numerical, and experimental methods. In the three approaches, the different parameters characterizing the burner ($L, H, h_{T,e}$, and k_s) have been set to the same value such that comparable results could be obtained. The flame position x_{flame} is non-dimensionalized using the length of the combustor (L=55mm) and the flame speed is non-dimensionalized using the freely propagating flame speed $S_{L,fr}$ which is 40 cm/s for CH_4 and 90 cm/s for H_2. This non-dimensionalization is performed so that results from computationally-tractable numerical simulations using hydrogen as a fuel can be compared to experimental measurements in methane flames. The geometric parameters in the analytical and numerical model are chosen to match the experiment (L=55mm, H=2mm, t=0.5mm). The equivalence ratio of the H_2 results is 0.5 and the equivalence ratio of the CH_4 results is 0.8.
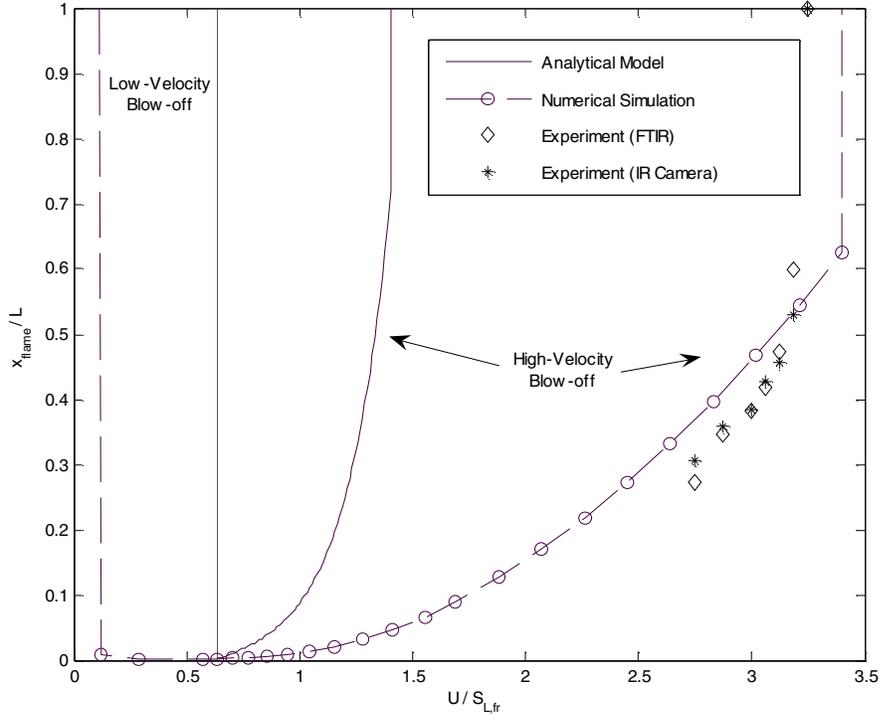
Figure 5-19: Dependence of flame location on inlet velocity predicted using analytical, numerical and experimental methods.

The results show that the FTIR and IR camera measurements of flame position are consistent with each other and are reasonably close to the predictions of the 1D numerical simulation in spite of the fact that the simulations use H_2 as a fuel whereas the experiment uses CH_4. This suggests that flame stabilization in this micro-channel is governed primarily by heat transfer and less by gas or surface chemistry. Finally, the fact that the flame locations determined using the two experimental techniques (IR camera and FTIR spectrometer) agree with each other well suggests that flame location can be determined using structure temperature. This is encouraging as it indicates that it will be possible to investigate combustion between plates made of materials like ceramics that are not transparent in the infrared.

5.5. Transient Stability: Results and Discussion

5.5.1 Introduction

The previous section investigated the steady-state stability of flames stabilized in micro-channels with conductive walls. However, another important issue in combustion systems is transient stability. This is especially true in micro-combustors because low Reynolds numbers and short residence times may not allow efficient mixing. Poor mixing can cause large fluctuations in the fuel-air composition at the entrance of the combustor and potentially lead to large disturbances in the flame position. To investigate this, we sinusoidally perturb the inlet velocity and equivalence ratio in the numerical simulation and observe the temporal response of the flame. This is illustrated schematically in figure 5-20. The perturbation process only begins after steady-state has been reached (typically after 100 s).
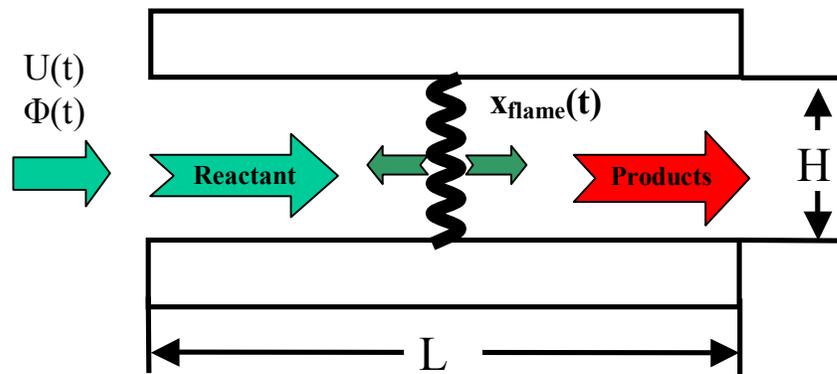
Figure 5-20: Schematic diagram illustrating the response of a flame stabilized in a micro-channel to perturbations in inlet velocity and equivalence ratio.

Figure 5-21 shows the transient behavior of a flame subjected to sinusoidal inlet velocity perturbations. The upper plot shows the non-dimensional inlet velocity as a function of non-dimensional time where $S_{L,fr}$ is the freely propagating flam speed and T is the oscillation period. For this case, T=0.1s (f=10Hz) and the length of the combustor is 1cm. The lower plot shows the temporal response of non-dimensional flame position (L is the length of the passage) as a function of non-dimensional time for two values of the distance between the plates. The figure shows that the fluctuations in flame position are much larger at H=5mm than at H=1mm. Therefore, the increased thermal coupling at small passage height seems to enhance transient flame stability (just like it enhanced steady-state stability) by suppressing the response of the flame to perturbations in inlet velocity
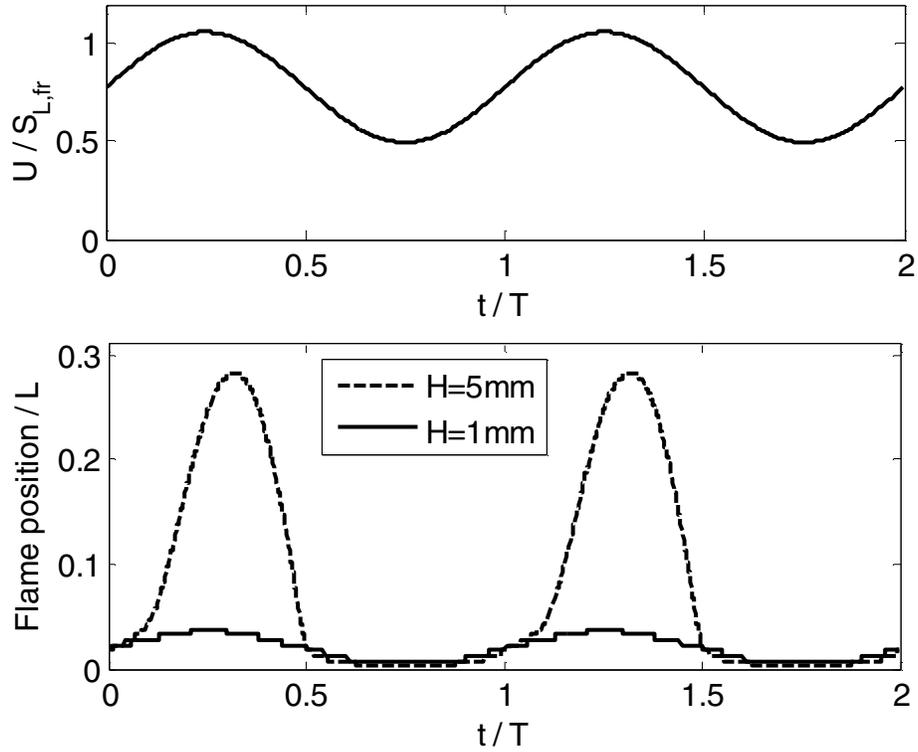
Figure 5-21: **Transient behavior of H₂-Air flames (F=0.5) subjected to perturbations in inlet velocity. The upper figure shows the velocity perturbation and the lower figure shows the response of the flame for two different passage heights.**

Figure 5-22 shows the effect of sinusoidal oscillations in equivalence ratio where the equivalence ratio is defined as:

$$\Phi = \frac{m_{fuel}/m_{air}}{\left(m_{fuel}/m_{air}\right)_{stoic.}} \qquad (5\text{-}23)$$
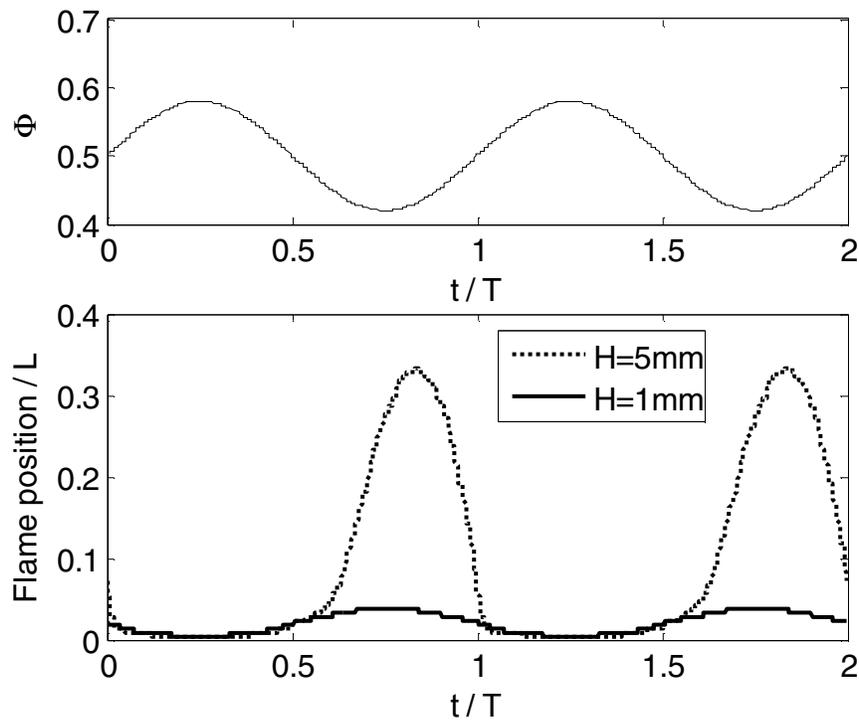
Figure 5-22: Transient behavior of H₂-Air flames subjected to perturbations in equivalence ratio. The upper figure shows the velocity perturbation and the lower figure shows the response of the flame for two different passage heights.

The figure shows that the flame stabilized in the smaller channel is also more stable with respect to oscillations in inlet mixture compositions. This is consistent with the steady modeling and simulation results that show that axial heat transfer through the structure broadens the range of stable burning velocities. The figure also shows that there is a 180° phase difference between the oscillation in equivalence ratio and the oscillation in the flame position. This is because as the equivalence ratio

decreases, the burning velocity of the mixture does also. Since the inlet velocity remains constant, this causes the flame position to shift downstream.

5.5.3. Effect of passage height

While the sample cases shown in the previous section provide some qualitative insight regarding the influence of the passage height on the transient stability of flames in micro-channels, a more systematic approach needs to be undertaken to understand the phenomenon in greater detail. To this end, the sinusoidal oscillation of inlet velocity is defined as:

$$U(t) = U_0\left(1 + a\,\sin\left(\frac{2\pi}{T}t\right)\right)$$

(5-24)

In equation 5-15, U_0 is the mean velocity of the flow, T is the oscillation period, and a is a non-dimensional parameter reflecting the amplitude of the perturbation. Note that $|a|>1$ U(t) becomes negative. To overcome this limitation, it is arbitrarily decided that

$$U(t) = \max\left(U_0\left(1 + a\,\sin(\frac{2\pi}{T}t)\right),\ \varepsilon\right)$$

(5-25)

where ε is a small velocity (1cm/s).

Figure 5-23 shows how the maximum flame position varies with the amplitude of the velocity perturbation for U_0=0.7m/s and for two values of H.
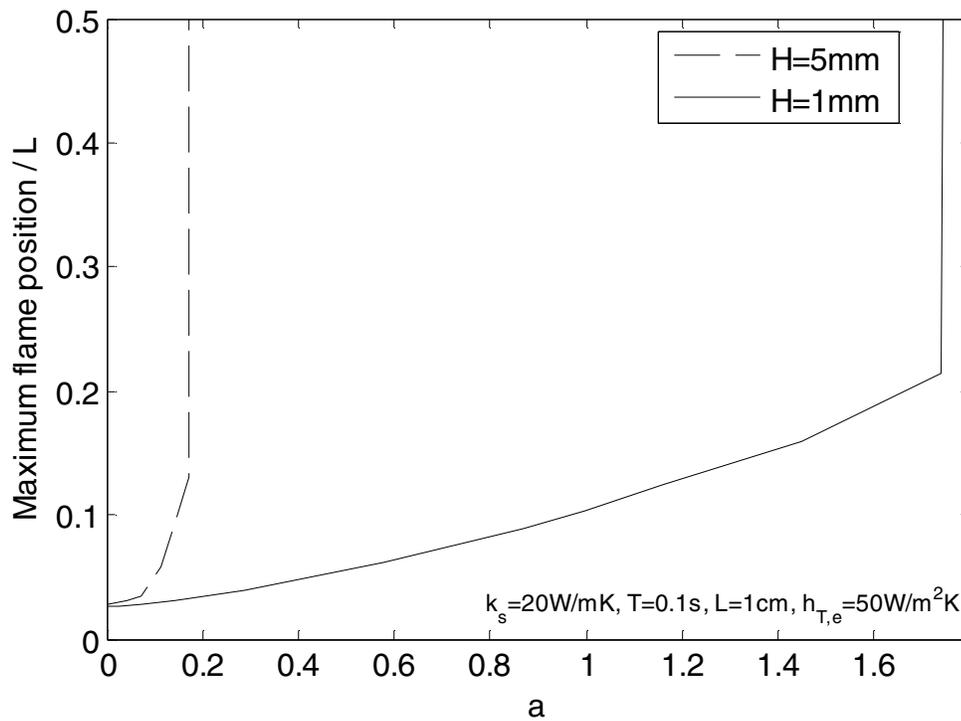
Figure 5-23: Evolution of normalized maximum flame position with normalized perturbation amplitude for different passage heights.

Again, the figure shows that flames stabilized in channels with smaller gaps can sustain larger inlet velocity perturbations. This greater stability can be attributed to the enhanced thermal coupling that occurs at small scale.

5.5.3. Effect of oscillatory period

Figure 5-24 shows the evolution of normalized maximum flame position as a function of normalized oscillation amplitude for different values of the oscillation period.
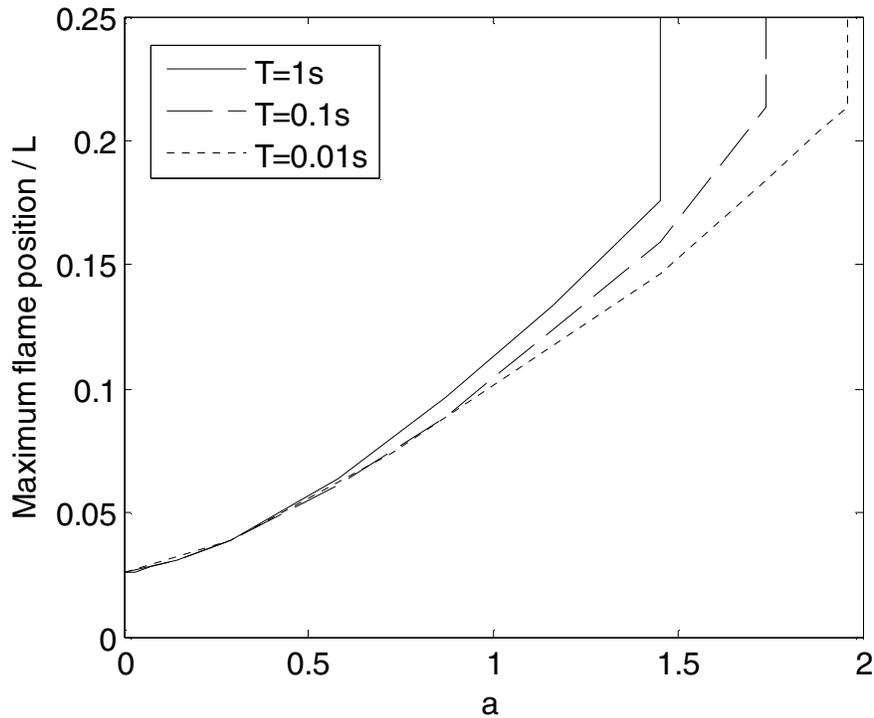
Figure 5-24: Evolution of normalized maximum flame position with normalized perturbation amplitude for different oscillation periods.

The figure shows that decreasing the period of the oscillation (or increasing its driving frequency) enables operation at higher velocity perturbation amplitudes. This is because there is a delay in the response of the flame due to the finite timescale for conduction within the structure of the combustor.

5.6. Conclusions

A simple model has been developed to understand and characterize the steady-state stability of flames in micro-channels. The predictions of the model are in good

qualitative agreement with those of more detailed 1D and 2D numerical simulations, as well as with experimental data. The enhanced stability was shown to depend on passage height, length, and the thermal conductivity of the structure. In general, decreasing the passage height and increasing the passage length and thermal conductivity of the structure tend to improve steady-state stability, and these improvements are caused by axial heat transfer through the combustor structure. The 1D numerical model was also used to investigate transient stability and the results also showed that smaller passage heights improved stability with respect to oscillations in inlet velocity and equivalence ratio. Taken together, the results described in this section demonstrate that another advantage of micro-burners is enhanced steady-state and transient stability.

Chapter 6:   Effect   of   Flame-Structure   Thermal Interaction on Chemistry

6.1. Introduction

In Chapter 2, enhanced thermal coupling between the reacting gas and the micro-combustor walls was shown to broaden the flame. In the numerical study, flame thickness was determined based on the spatial evolution of gas temperature:

$$\delta_r = \frac{T_f - T_0}{\left(\dfrac{dT}{dx}\right)_{max}}$$

(6-1)

However, one would also expect the broadening effect to be reflected in the spatial evolution of chemical species concentrations.   This is important for understanding the effect of thermal coupling on a micro-combustor's chemical efficiency: if species concentration profiles become broader, micro-combustors will have to be proportionally longer than their conventional-scale counterparts to achieve comparable levels of efficiency.

In Chapter 3 of this work, the performance of both hydrogen and methane micro-combustors was investigated. It was suggested that the behavior of H_2-air flames and CH_4-air flames was found to be quite different as the combustor's scale was reduced. Methane flames were characterized by much larger temperature overshoots compared

to hydrogen flames, leading to an optimum combustor configuration at a scale much larger than for hydrogen. While the reasons for this discrepancy in behavior remain unclear, one hypothesis is that it is due to dissimilarities in the chemical mechanisms used to model combustion. This would mean that the thermal coupling between the gas and structure that occurs at micro-scale affects the general characteristics of the combustion chemistry as the scale of the combustor is reduced. Further, it suggests that global reaction mechanisms (for example[70, 71]) developed for conventional-scale flows where heat recirculation is not important may not be appropriate for use at the micro-scale where heat recirculation is strong and reaction zones are broadened.

As a result, this chapter seeks to further our understanding of the influence of the thermal interaction between the reacting gas and the structure of the combustor by investigating the effect of this interaction on the chemical species profile through the flame and on the operation of the chemical mechanism for combustion. Particular attention is paid to the relative importance of the different elementary reactions in the mechanism as the scale of the passage, and thus the strength of the interaction between the reacting fluid and the combustor structure, is varied. This is important for understanding the effects of structural heat conduction on the progress of the individual elementary reactions that compose the overall reaction, and the effect of heat transfer on the choice of an appropriate reaction mechanism.

6.2. Alternate definitions of reaction zone thickmess

One way to define a chemically-based reaction zone thickness is to consider radical species concentration distribution. Figure 6-1 shows the H and O radical

profiles for large and small passage height (H=1cm and H=0.005cm respectively) where the passage length is L=1cm. The fuel considered is H_2 burning in air at an equivalence ratio of 0.5 and the numerical code presented in Chapter 2 is used to compute the profiles.
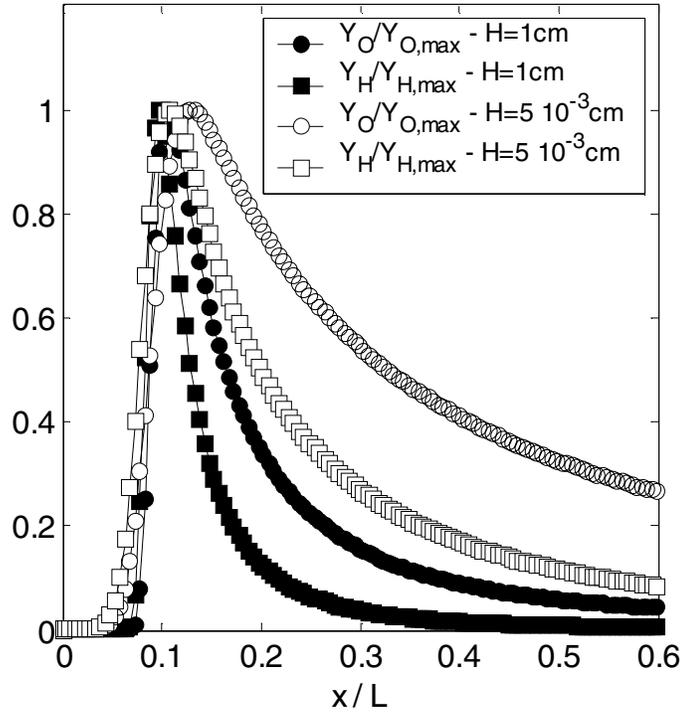
Figure 6-1: H and O radical mass fraction profiles as a function of non-dimensionalized streamwise coordinate for L=1cm, Φ=0.5 and P=1atm.

The figure clearly shows that the thickness of the radical profiles is larger for the situation where H is smaller. There are several possible approaches for determining the flame thickness based on chemical species concentration. One approach is to define the flame thickness as the distance between the points at which the radical mass fraction reaches half of its peak value. This is illustrated in figure 6-2.
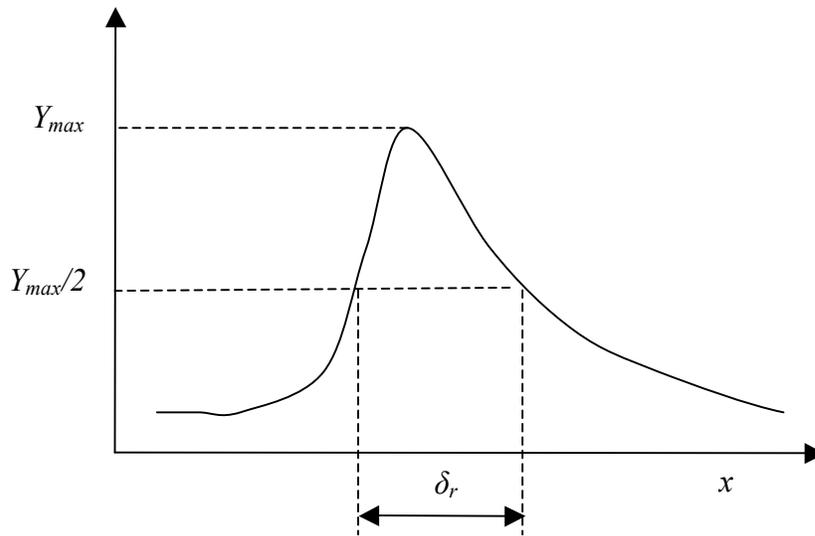
Figure 6-2: Definition of the flame thickness based on the evolution of a radical species mass fraction.

Another approach is to focus on a reaction product such as H_2O and define the flame thickness as the distance necessary to reach 90% of the equilibrium H_2O mass fraction. This is illustrated in figure 6-3. Finally, one could take a similar approach with a reactant by, for example, defining the flame thickness as the distance required for the H_2 mass fraction to drop to 10% of its inlet value.
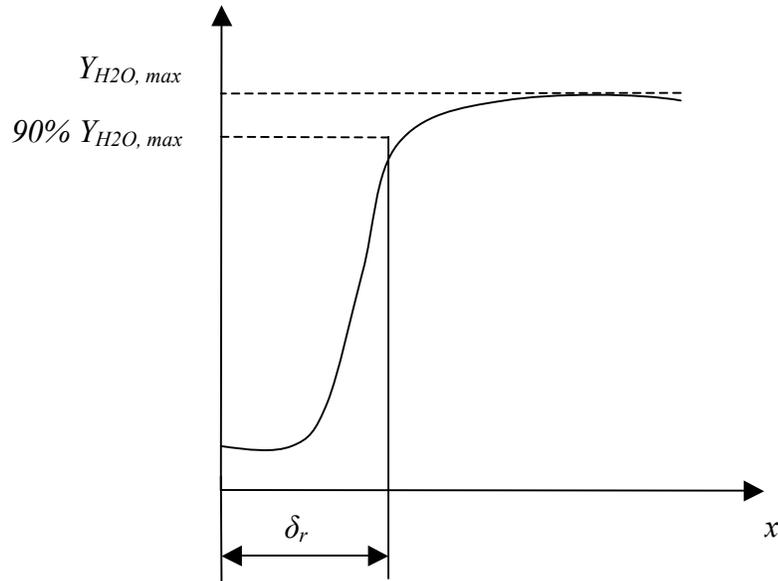
Figure 6-3: Definition of the flame thickness based on the H$_2$O mass fraction.

Figure 6-4 compares the evolution of the non-dimensional flame thickness determined using the alternative chemically-based metrics discussed above to each other and to the flame thickness defined based on the temperature profile (equation 6-1). . The conditions are P=1atm, Φ=0.5 and L=1cm.
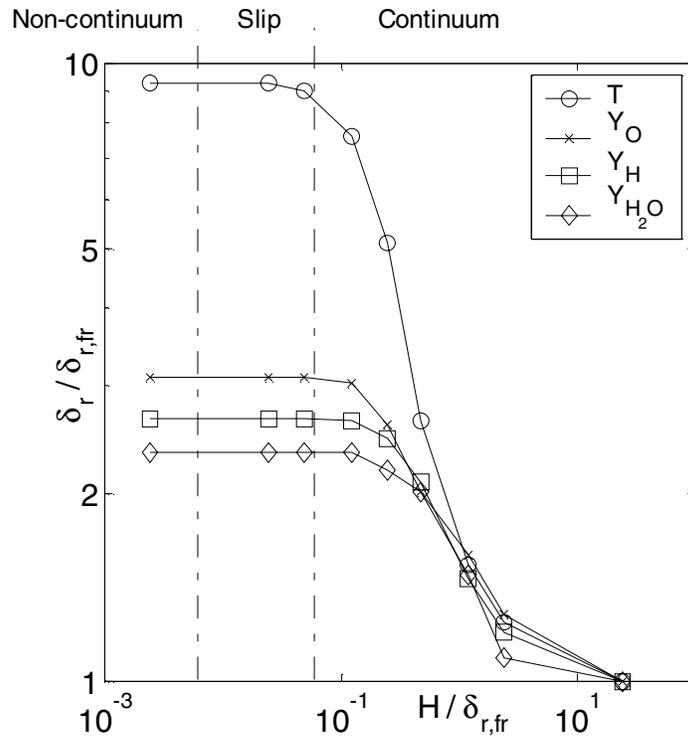
Figure 6-4: Evolution of non-dimensional flame thickness as a function of non-dimensional passage height for several definitions of the flame thickness. The legend indicates the parameter upon which the flame thickness is computation is based.

The figure shows that each method of measuring the reaction zone thickness shows the same limit-cycle behavior. This demonstrates that while the presence of the flame broadening phenomenon is independent of the measurement method, the amplitude of the broadening does depend on the measurement method. Nevertheless, the amplitudes of the species-based metrics do seem to be self-consistent within 30%.

The fact that the species profiles tend to broaden directly affects chemical efficiency. Chemical efficiency is defined as the ratio of the total heat evolved in the

reaction to the total heat available if the reaction were to go to completion. In this work, we assume that this is equivalent to the fraction of H_2 that gets consumed before the mixture exits the micro-channel:

$$\eta_{ch} = \frac{Total\ heat\ evolved\ by\ rxn.}{Maximum\ heat\ available}$$

$$= 1 - \frac{Y_{H_{2,out}}}{Y_{H_{2,i}}}$$

(6-2)

Figure 6-2 and equation 6-2 suggests that a direct consequence of the broadening phenomenon is a reduction in the chemical efficiency. Figure 6-5 is a plot of the chemical efficiency as a function of non dimensional passage height for fixed combustor lengths (L=1cm and L=0.5cm). It shows that decreasing H decreases the chemical efficiency as the flame broadens. It also shows that a greater change in chemical efficiency occurs if the combustor length is reduced.
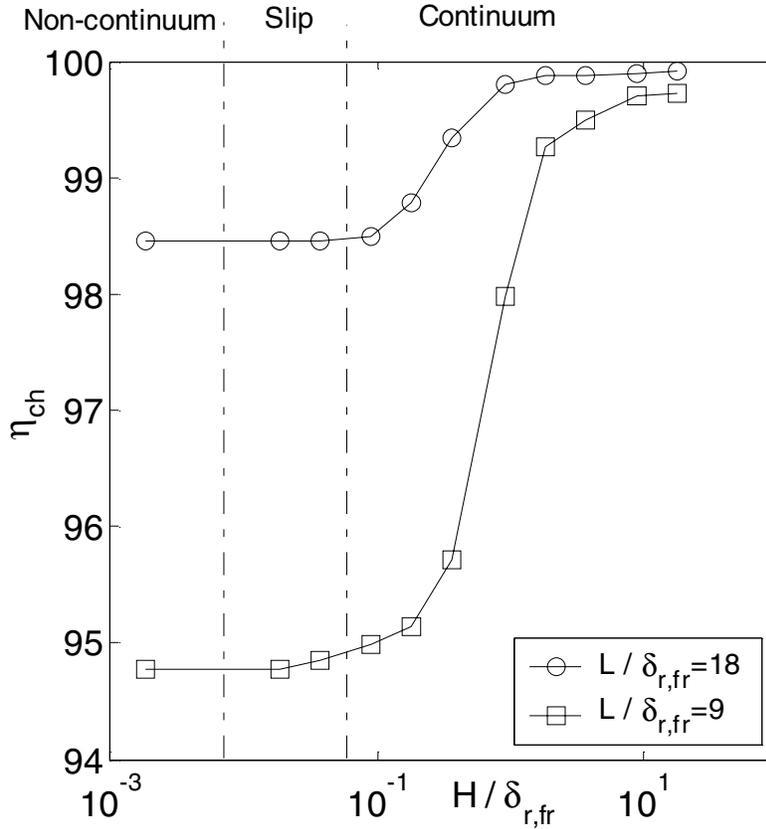
Figure 6-5: Evolution of chemical efficiency as a function of non-dimensionalized passage height for *L*=1cm and *L*=0.5cm. The fuel is H₂ burning in air at an equivalence ratio of 0.5 and a pressure *P*=1 atm.

6.3. Effect of thermal coupling on the kinetics of a multi-step reaction mechanism

The numerical model presented in Chapter 2 of this work is used to investigate the effect of gas-structure interaction on the kinetics of the detailed hydrogen combustion mechanism used to model chemistry, i.e. the relative operation of the individual elementary reactions that are used to model the overall conversion of the reactants

(H_2 and air) to products (H_2O) in the combustion process. Table 4 in Appendix II lists the elementary reactions considered in the analysis as well as their assigned reaction number (R#). Since each reaction has a different activation energy E_a, each reaction has a different sensitivity to changes in temperature. Therefore, it is reasonable to expect that differing levels of heat recirculation could cause the relative rates of the elementary reactions composing the overall reaction to change.

Figure 6-6 shows the rates of progress for the major reactions (those with the largest overall reaction rate) - i.e. 1, 2, 3, 9 and 13 - occurring in the atmospheric pressure H_2-air flame as a function of downstream distance x for L=5mm, H=1cm. These reactions are listed in table 3:

Reaction number	Reaction	Reaction type
1	H+O2=O+OH	Branching
2	H2+O=H+OH	Branching
3	H2+OH=H2O+H	Propagation
9	H+O2+M=HO2+M	Propagation
13	HO2+H=OH+OH	Propagation

Table 3: Major reactions occurring in the flame.

The fuel considered is hydrogen burning in air at an equivalence ratio of 0.5 and a pressure p=1 atm. Figure 6-7 is the same as 6-6 except that the value of H is now reduced to 100μm.
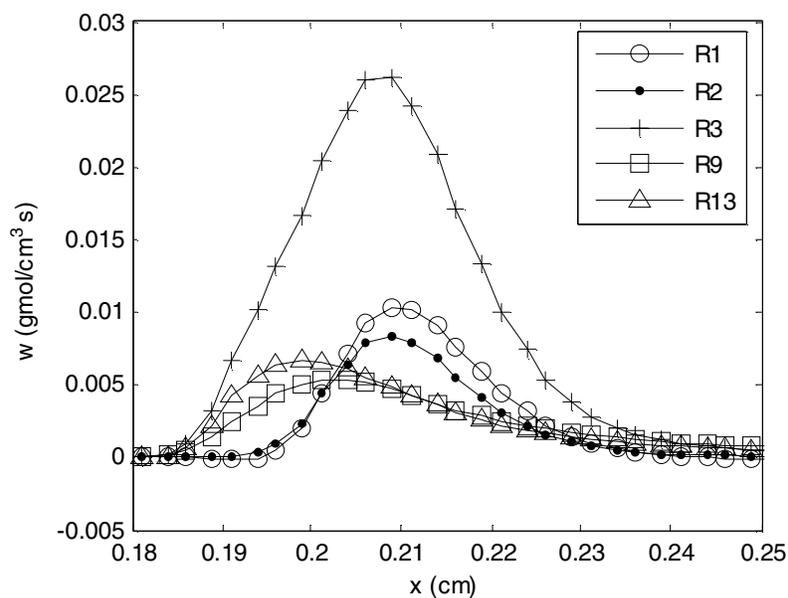
Figure 6-6: Evolution of rates of progress of the five most important reactions as a function of downstream distance for *L*=5mm and *H*=1cm.
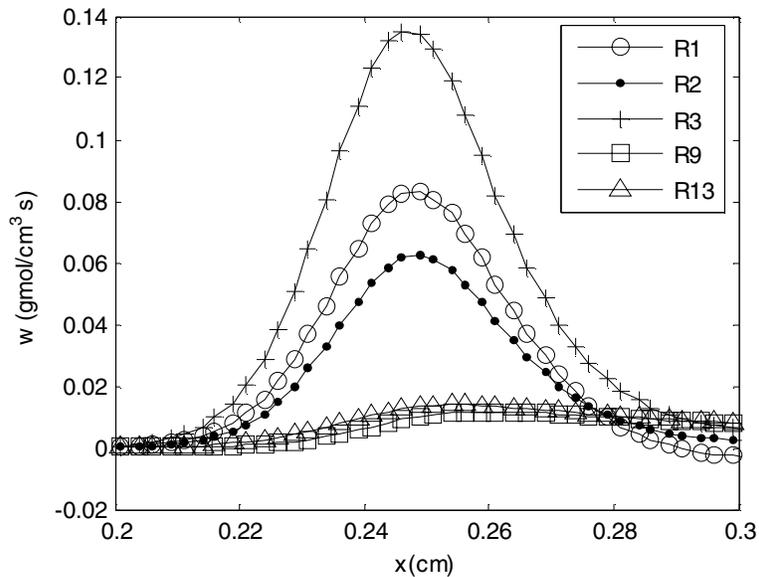
Figure 6-7: Evolution of rates of progress of the five most important reactions as a function of downstream distance for *L*=5mm and *H*=100μm.

Several observations can be made when comparing figures 6-6 and 6-7. First, the rates of progress of the reactions for the smaller passage height are much higher than that for the larger passage height. This is because as H decreases, heat recirculation raises the wall temperature which, in turn, raises gas temperature, the rates of the individual reactions, and hence the rate of the overall reaction. This, in turn, results in an increase in the burning velocity of the mixture. Second, the different peaks in the curves appear to be wider for the smaller passage height compared to the larger passage height (note that the ranges of the x-axis are different in figures 6-6 and 607). This is also a consequence of heat recirculation which tends to broaden the reaction zone, as discussed in section 6.2. Lastly, the overall shapes of the rates of progress curves appear to be different for the two passage heights. Taken together, these results suggest that the thermal coupling between the gas and the structure of the combustor not only has an impact on the burning velocity and flame thickness, but also on the elementary reactions that make up the overall reaction.

To better quantify how the relative importance of the elementary reactions composing the overall reaction is affected by the size of the combustor, we define a parameter ϖ_i which represents the total rate at which a particular reaction "processes" reactants divided by the rate at which material is processed by the overall reaction. This can be written as the area contained under the curves shown on figures 6-6 and 6-7 divided by the burning rate:

$$\varpi_i = \frac{\int_0^L w_i(x)\, dx}{S_L} \qquad (6\text{-}3)$$

145

In equation 6-3, $w_i(x)$ is the rate of progress of reaction i and S_L is the laminar burning velocity. This parameter is representative of the importance of reaction i.

Figure 6-8 shows ϖ_i for the five most important reactions identified in figures 6-6 and 6-7 for two different passage heights: H=1cm and H=100μm. The figure shows that the relative importance of these elementary reactions changes as the size of the combustor is reduced: While ϖ_i increases slightly for reaction 2 and decreases slightly for reaction 1, it decreases significantly for the other reactions. This shows that the reactions that dominate in the detailed mechanism change as the strength of the thermal coupling between the gas and the structure increases.
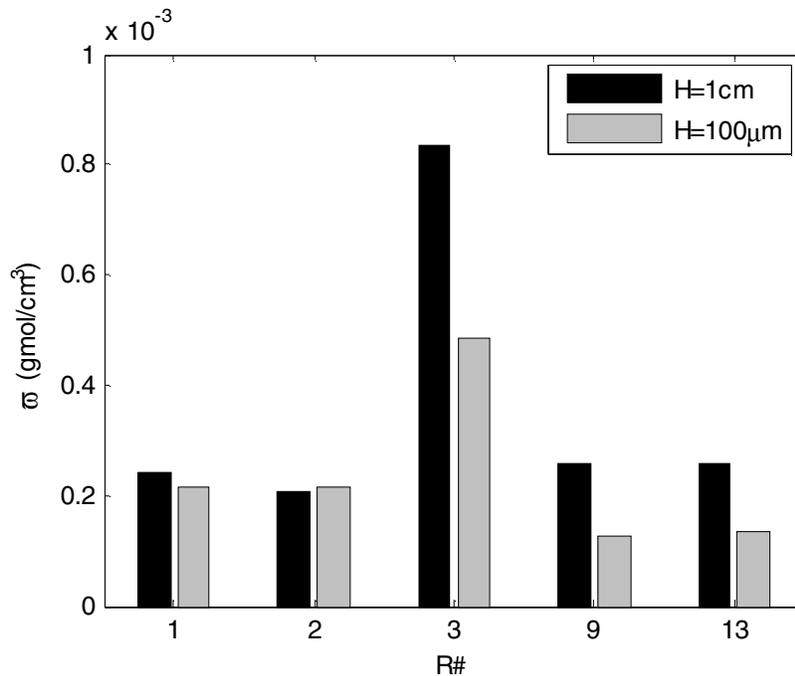
Figure 6-8: Comparison of the relative importance of the five most important reactions for two different values of the passage height.

The results described above are important because they show that the strong interaction between gas and structure that occurs in micro-scale combustors affects the relative rates at which individual elementary reactions run. This, in turn, suggests that global reaction mechanisms developed for conventional-scale problems where heat recirculation is absent or weak may not be appropriate for use in micro-scale combustors. Therefore, in the absence of validated single-step mechanisms, it may be necessary to use detailed reaction mechanisms in order to obtain accurate results.

6.4. Conclusions

While structural heat conduction affects the general characteristics of a flame stabilized in a micro-channel (i.e. burning rate, flame thickness, and stability), the results presented in this chapter show that it also influences flame chemistry itself.

This means that the consequences of flame broadening are not only observed in the temperature profile (which becomes less steep), but also in the evolution of chemical species (radical species, reactants, products) and of the evolution of the reaction rate profiles for each of the different elementary reactions composing the detailed mechanism. Heat recirculation tends to broaden the chemical species profiles, suggesting that as the passage height is reduced a proportionally longer combustor is necessary to achieve good fuel conversion and therefore chemical efficiency.

Another important conclusion is that the relative importance of individual elementary reactions is also affected by heat recirculation, suggesting that global mechanisms developed for large scale combustors where thermal coupling is weak might not be applicable to small scale combustors.

While these observations are a first step towards the understanding of the effect of gas-structure thermal interaction on the chemical reactions itself, more substantial work would be necessary to fully characterize this influence. In particular, the development of single step mechanisms validated for use at the micro-scale would facilitate 3D simulations necessary for capturing the full physics of gas-structure interaction.

Chapter 7:   Conclusions and Perspectives

7.1. Contribution and key findings

This thesis has investigated the effect of structural heat conduction on several aspects of microscale combustion and propulsion. Simple analytical models were developed in order to understand the basic physics of combustion in a micro-channel. Good qualitative agreement between the results of the analytical models and those of a more detailed numerical simulation that included distributed heat transfer between gas and structure, heat conducting within the structure, heat loss, and detailed chemistry was found, suggesting that the physical processes accounted for in the first-order models are those governing flame propagation in the presence of a conductive structure. These compact models offer the possibility for first-order design of micro-combustors by investigating the effect of a wide range of parameters in little computational time. They also provide unique insight regarding the basic physics of flame propagation in micro-channels and show that structural heat conduction is a dominating effect at small scale. The latter was shown to affect flame characteristics and to greatly influence the performance of micro-combustors and micro-thrusters. The key findings of the thesis are summarized below.

First, the structure of the flame itself was shown to be modified due to heat recirculation via the structure of a parallel plate micro-combustor. Increases of flame thickness by an order of magnitude were predicted by a simple analytical model that

extended the theory of Mallard and Le Chatelier. The analytical results were subsequently confirmed by the more detailed numerical simulation.

Second, burning rate was also shown to increase at small scale due to heat recirculation, and substantially raise the power density of micro-combustors as compared to their conventional scale counterparts. However, the price to pay for this larger power density is that overall combustion efficiency decreases.

Third, a similar behavior was found when the power density results were used to model the combustion chamber of a micro-thruster. The possibility for a great increase in thrust-to-weight ratio was suggested, at the price of a lower specific impulse.

Fourth, structural heat conduction was shown to greatly influence flame stability. In particular, enhanced flame stability was observed analytically, numerically, and experimentally. This behavior was found to be in good qualitative agreement with the results of much more detailed 2D numerical simulations performed by other researchers.

Fifth and finally, the thermal interaction between gas and structure was shown to influence chemistry at small scale, questioning the validity of global reaction mechanisms when thermal coupling is not negligible.

7.2. Future work

The field of micro-combustion is still developing and this work only investigated a specific aspect of the problem, i.e. the effect of structural heat conduction. Much

more work is still needed in order to find a truly practical application for sub-millimeter scale combustors.

Much more work is also needed to fully understand the effect of fluid-structure coupling on the characteristic of micro-combustors.

First, one important area that requires more investigation is catalysis in order to take advantage of the large surface to volume ratios characteristic of micro-devices, and to model important processes such as radical quenching.

Second, the results computed using the 1D numerical model should be compared to more detailed 2D numerical simulations. This would allow better modeling of the heat transfer between gas and structure by avoiding the necessity to impose the Nusselt number.

Third, pressure loss can be substantial in micro-devices, and the only reliable way to predict the magnitude of this loss is by solving the momentum equation for the flow field. Thus, integrating this additional equation in the numerical model would be useful and relevant especially for 2D and 3D simulations.

Fourth, the effect of slip on the thermal feedback process should be investigated in greater detail. Temperature slip has already been studied in chapter 2 of this thesis but velocity and species concentration slip could also be important – especially in catalytic systems.

Fifth, more realistic fuels should be considered in order to provide more sensitive estimates of the performance of micro-combustors and micro-thrusters. For example, natural gas or butane could be considered for Earth-based applications, JP10 for

micro-UAV engines, and high pressure liquid hydrogen and oxygen for micro-rockets.

Sixth, the effect of thermal coupling on chemistry was only briefly investigated. Much more work is necessary in order to understand the effect of heat recirculation on detailed chemical processes.

Finally, and probably most importantly, the results presented in this work are mostly analytical and numerical. Thorough experimental investigation of the phenomena predicted by the models is necessary. In particular, experiments need to be developed for measuring flame broadening, the possibility of obtaining high power density in micro-combustors, thrust-to-weight ratio augmentation in micro-thrusters, steady-state and transient stability, and the effect of thermal feedback on chemical conversion.

Appendix I
The Thermal Theory of Mallard and Le Chatelier

In 1884, two French scientists developed the well-established thermal theory of flame propagation[72] based on the idea that the burning velocity is fixed by the rate at which conductive heat transfer from the hot products in the post-flame region pre-heats the reactants entering the reaction zone. The flame is illustrated in figure A1-1 and a simplified temperature profile through it is illustrated in figure A1-2. The flame is divided into two zones:

- A pre-heat zone in which the temperature of the reactants rises from its initial value T_0 to an ignition temperature T_i.

- A reaction zone in which the temperature of the gas rises from T_i to the adiabatic flame temperature T_f.
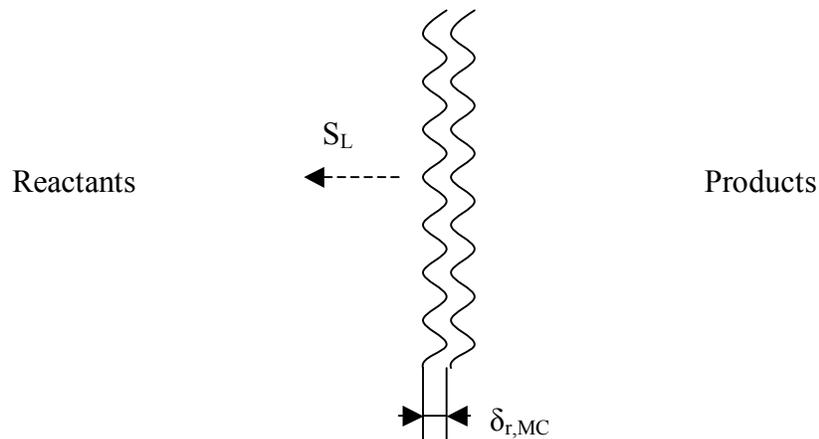
Figure A1-1: Freely propagating laminar premixed flame.
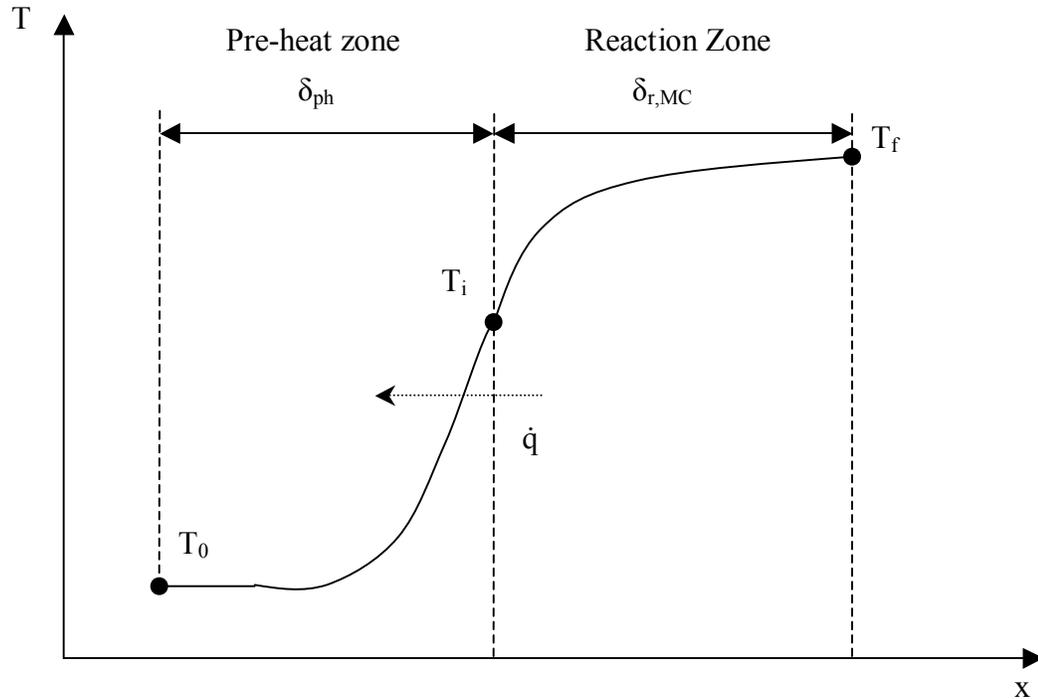
Figure A1-2: Temperature profile through the freely propagating flame.

The basic idea behind this simple model is that the energy needed to heat the reactants from T_i to T_0 in the preheat zone must be transferred by conduction from the reaction zone to the preheat zone. This energy balance is expressed as follows:

$$\dot{m}_r C_{p,r}(T_i - T_0) = \dot{q} \qquad (\text{A1-1})$$

where $\dot{m}_r$ is the mass flow rate of the reactants, $C_{p,r}$ is the specific heat at constant pressure of the reactants and $\dot{q}$ is the rate of conductive heat transfer from the reaction zone to the pre-heat zone.

Assuming that the temperature profile of the gas in the reaction zone is linear gives the following expression for the heat transfer from the reaction zone to the preheat zone can be expressed as:

$$\dot{q} = k_r A_r \frac{T_f - T_i}{\delta_{r,MC}}$$
(A1-2)

In this expression, k_r is the thermal conductivity of the reactants, A_r is the cross-sectional area for conduction in the gas-phase, and $_{r,MC}$ is the flame thickness.

The mass flow rate of the reactants can be expressed as:

$$\dot{m}_r = \rho_r A_r S_L$$
(A1-3)

where S_L is the laminar flame speed or the relative speed of the incoming the reactants. The laminar flame speed is related to the reaction rate RR and the flame thickness δ_r as follows:

$$S_L = \frac{\delta_{r,MC}}{RR}$$
(A1-4)

Substituting A2-2 – A2-4 into A2-1 gives:

$$\rho_r A_r S_L C_{p,r}(T_i - T_0) = (T_f - T_i) A_r RR \frac{1}{S_L}$$
(A1-5)

Solving A1-5 for S_L gives:

$$S_L = \sqrt{\frac{T_f - T_i}{T_i - T_0} \frac{k_r}{\rho_r C_{p,r}} RR}$$
(A1-6)

This is the well-known expression for the laminar flame speed derived by Mallard and Le Chatelier. This expression can be inverted using equation A2-4 to give the reaction zone thickness which is the quantity we are interested in here:

$$\delta_{r,MC} = \sqrt{\frac{T_f - T_i}{T_i - T_0} \frac{k_r}{\rho_r C_{p,r}} \frac{1}{RR}}$$
(A1-7)

It will be convenient to note that A1-6 and A1-7 can also be derived using a thermo-electrical analogy. The appropriate thermal circuit for heat exchange in the flame is depicted in figure A1-3.

155
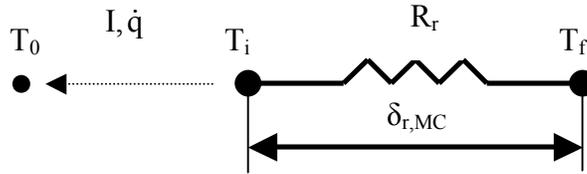
Figure A1-3: Thermal circuit for a freely-propagating flame

In this analogy, electrical current (I) corresponds to heat flow ($\dot{q}$), potentials (V) correspond to temperatures (T), and resistors relate temperature gradients to heat fluxes as follows:

$$\underbrace{I = \frac{\Delta V}{R_r}}_{\substack{\text{Electric} \\ \text{intensity}}} \Leftrightarrow \underbrace{\dot{q} = \frac{\Delta T}{R_r}}_{\substack{\text{Thermal} \\ \text{heat flux}}} \tag{A1-8}$$

The thermal resistance to axial conduction through the reactants gas column R_r can be expressed as:

$$R_r = \frac{\delta_{r,MC}}{k_r A_r} \tag{A1-9}$$

Combining A1-8 and A1-9 gives the conductive heat flow:

$$\dot{q} = \frac{T_f - T_i}{R_r} = \frac{T_f - T_i}{\delta_{r,MC}} k_r A_r \tag{A1-10}$$

Note that this is the same expression as A1-2.

156

Combining A1-1, A1-3 and A1-10, and solving for S_L and δ_r recovers the same expressions for S_L and δ_r as derived earlier (A1-6 and A1-7).

Appendix II
Detailed Reaction Mechanisms

The mechanisms are written in CHEMKIN format:

$$k = AT^b e^{-Ea/RT}$$

The units are A: mole-cm-sec-K, E: cal/mole

II.1. Hydrogen Combustion Mechanism

Reaction number	Reaction	A	b	Ea
1	H+O2=O+OH	5.10E+16	-0.8	16510
2	H2+O=H+OH	1.80E+10	1	8830
3	H2+OH=H2O+H	1.20E+09	1.3	3630
4	OH+OH=H2O+O	6.00E+08	1.3	0
5	H+OH+M=H2O+M	7.50E+23	-2.6	0
6	O2+M=O+O+M	1.90E+11	0.5	95560
7	H2+M=H+H+M	2.20E+12	0.5	92600
8	H2+O2=OH+OH	1.70E+13	0	47780
9	H+O2+M=HO2+M	2.10E+18	-1	0
10	H+O2+O2=HO2+O2	6.70E+19	-1.4	0
11	H+O2+N2=HO2+N2	6.70E+19	-1.4	0
12	HO2+H=H2+O2	2.50E+13	0	700
13	HO2+H=OH+OH	2.50E+14	0	1900
14	HO2+O=OH+O2	4.80E+13	0	1000
15	HO2+OH=H2O+O2	5.00E+13	0	1000
16	HO2+HO2=H2O2+O2	2.00E+12	0	0
17	H2O2+M=OH+OH+M	1.20E+17	0	45500
18	H2O2+H=HO2+H2	1.70E+12	0	3750
19	H2O2+OH=H2O+HO2	1.00E+13	0	1800

Table 4: Hydrogen combustion mechanism[73]

II.2. Methane Combustion Mechanism

Reaction number	Reaction	A	b	Ea
1	H2+CH2(S)=CH3+H	7.23E+13	0	0
2	H2+O=OH+H	51200	2.7	26.3
3	H2O+H=H2+OH	452000000	1.6	77.1
4	CH4+O2=CH3+HO2	3.97E+13	0	238
5	CH4+C=CH+CH3	5E+13	0	100.5
6	CH4+H=CH3+H2	13200	3	33.6
7	CH4+CH=C2H4+H	3.01E+13	0	-1.7
8	CH4+CH2=CH3+CH3	4.3E+12	0	42
9	CH4+CH2(S)=CH3+CH3	7E+13	0	0
10	CH4+C2H=CH3+C2H2	1.81E+12	0	0
11	CH4+O=CH3+OH	723000000	1.6	35.5
12	CH4+OH=CH3+H2O	15700000	1.8	11.6
13	CH4+HO2=CH3+H2O2	9.03E+12	0	103.4
14	C2H2+C2H2=H2CCCCH+H	2000000000	0	242
15	C2H2+O2=C2H+HO2	1.2E+13	0	312
16	H2+C2H=C2H2+H	1.08E+13	0	9.1
17	C2H2+H(+M)=C2H3(+M)	8.43E+12	0	10.8
18	C2H2+CH=C2H+CH2	2.11E+14	0	-0.5
19	C2H2+CH2=C3H4	1.2E+13	0	27.7
20	C2H2+CH2(S)=H2CCCH+H	1.75E+14	0	0
21	C2H2+C2H=C4H2+H	9.03E+13	0	0
22	C2H2+O=CH2+CO	2170000	2.1	6.6
23	C2H2+O=HCCO+H	5060000	2.1	6.6
24	C2H2+OH=C2H+H2O	6E+13	0	54
25	C2H2+M=C2H+H+M	1.14E+17	0	447
26	C2H4+H=C2H3+H2	5.42E+14	0	62.4
27	C2H4+H(+M)=C2H5(+M)	3970000000	1.3	5.4
28	C2H4+CH=C3H4+H	1.32E+14	0	-1.4
29	C2H4+CH2(S)=C3H6	9.64E+13	0	0
30	C2H4+CH3=CH4+C2H3	4.16E+12	0	46.6
31	C2H4+O=H+CH2HCO	4740000	1.9	0.8
32	C2H4+O=CH3+HCO	8130000	1.9	0.8
33	C2H4+O=CH2CO+H2	680000	1.9	0.8
34	C2H4+OH=C2H3+H2O	2.05E+13	0	24.9
35	C2H4+M=C2H2+H2+M	9.97E+16	0	299.3
36	C2H4+M=C2H3+H+M	7.4E+17	0	404.1
37	C2H6+H=C2H5+H2	1450000000	1.5	31
38	C2H6+CH=C2H4+CH3	1.08E+14	0	-1.1
39	C2H6+CH2(S)=CH3+C2H5	2.4E+14	0	0
40	C2H6+CH3=C2H5+CH4	0.000000151	6	25.3
41	C2H6+O=C2H5+OH	1000000000	1.5	24.3
42	C2H6+OH=C2H5+H2O	7230000	2	3.6
43	C2H6+HO2=H2O2+C2H5	1.32E+13	0	85.6

44	C4H2+O=C3H2+CO	7.89E+12	0	5.6
45	C4H2+OH=C3H2+HCO	6.68E+12	0	-1.7
46	O2+CO=CO2+O	1.26E+13	0	196.9
47	O2+CH2O=HCO+HO2	6.02E+13	0	170.1
48	O2+C=CO+O	1.2E+14	0	16.7
49	O2+H+M=HO2+M	2.1E+18	-0.8	0
50	O2+H+H2O=HO2+H2O	6.89E+15	0	-8.7
51	O2+H=OH+O	9.76E+13	0	62.1
52	O2+CH=CO+OH	1.66E+13	0	0
53	O2+CH=CO2+H	1.66E+13	0	0
54	O2+CH2=CO2+H2	5.43E+12	0	6.2
55	O2+CH2=CO2+H+H	5.43E+12	0	6.2
56	O2+CH2=CO+OH+H	8.15E+12	0	6.2
57	O2+CH2=CO+H2O	1.48E+12	0	6.2
58	O2+CH2=CH2O+O	4.2E+12	0	6.2
59	O2+CH2(S)=CO+OH+H	3.13E+13	0	0
60	O2+CH3=CH2O+OH	3.31E+11	0	37.4
61	O2+C2H=HCCO+O	9.05E+12	0	0
62	O2+C2H=CO2+CH	9.05E+12	0	0
63	O2+C2H3=C2H2+HO2	5.42E+12	0	0
64	O2+C2H5=C2H4+HO2	10200000000	0	-9.2
65	O2+C3H2=HCO+HCCO	1E+13	0	0
66	O2+H2CCCH=CH2CO+HCO	30100000000	0	12
67	O2+HCO=HO2+CO	3.01E+12	0	0
68	O2+CH3O=CH2O+HO2	21700000000	0	7.3
69	O2+CH2OH=CH2O+HO2	1.57E+15	-1	0
70	O2+CH2OH=CH2O+HO2	7.23E+13	0	15
71	O2+HCCO=CO+CO+OH	1.63E+12	0	3.6
72	H2O2+H=HO2+H2	1.69E+12	0	15.7
73	H2O2+H=OH+H2O	1.02E+13	0	15
74	H2O2+O=OH+HO2	6.62E+11	0	16.6
75	H2O2+OH=H2O+HO2	7.83E+12	0	5.6
76	OH+OH(+M)=H2O2(+M)	7.23E+13	-0.4	0
77	CO+O+M=CO2+M	1.54E+15	0	12.6
78	CO+OH=CO2+H	16600000	1.3	-3.2
79	CO+HO2=CO2+OH	1.51E+14	0	99
80	CO+CH=HCCO	2.77E+11	0	-7.2
81	CO2+CH=HCO+CO	3.43E+12	0	2.9
82	CO2+CH2=CH2O+CO	23500000000	0	0
83	CH2O+H=HCO+H2	126000000	1.6	9.1
84	CH2O+CH=CH2+HCO	9.64E+13	0	-2.2
85	CH2O+CH3=CH4+HCO	7.83E-08	6.1	8.2
86	CH2O+O=HCO+OH	4.16E+11	0.6	11.6
87	CH2O+OH=HCO+H2O	3430000000	1.2	-1.9
88	CH2O+HO2=H2O2+HCO	3.01E+12	0	54.7
89	CH2O+M=HCO+H+M	1.4E+36	-5.5	404.6
90	CH2O+M=H2+CO+M	3.26E+36	-5.5	404.6
91	CH2CO+H=CH3+CO	1.81E+13	0	14.1
92	CH2CO+O=CH2+CO2	1.33E+12	0	5.7
93	CH2CO+O=CH2O+CO	4.58E+11	0	5.7

94	CH2CO+O=HCO+H+CO	2.52E+11	0	5.7
95	CH2CO+O=HCO+HCO	2.52E+11	0	5.7
96	CH2CO+OH=CH3+CO2	2.52E+12	0	0
97	CH2CO+OH=CH2OH+CO	4.68E+12	0	0
98	CH2CO+M=CH2+CO+M	6.57E+15	0	241
99	CH2CO+M=HCCO+H+M	1140000000	0	0
100	C+CH2=C2H+H	5E+13	0	0
101	C+CH3=C2H2+H	5E+13	0	0
102	C+OH=CO+H	5E+13	0	0
103	H+H+M=H2+M	1.87E+18	-1	0
104	H+H+H2=H2+H2	9.79E+16	-0.6	0
105	H+CH=C+H2	8.43E+12	0	0
106	H+CH2=CH+H2	6.02E+12	0	-7.5
107	H+CH2(S)=CH2+H	2E+14	0	0
108	H+CH3(+M)=CH4(+M)	1.69E+14	0	0
109	H+C2H3=C2H2+H2	1.2E+13	0	0
110	CH3+CH3=C2H5+H	3.01E+13	0	56.5
111	H+O+M=OH+M	1.18E+19	-1	0
112	H+OH+M=H2O+M	5.53E+22	-2	0
113	H+HO2=H2+O2	4.28E+13	0	5.9
114	H+HO2=OH+OH	1.69E+14	0	3.7
115	H+HO2=H2O+O	3.01E+13	0	7.2
116	H+HCO=CO+H2	9.03E+13	0	0
117	H+CH3O=CH2O+H2	1.81E+13	0	0
118	H+CH2OH=CH3+OH	1.02E+13	0	0
119	H+CH2OH=CH2O+H2	3.08E+13	0	0
120	H+HCCO=CH2+CO	1.51E+14	0	0
121	CH+CH2=C2H2+H	4E+13	0	0
122	CH+CH3=C2H3+H	3E+13	0	0
123	CH+C2H3=CH2+C2H2	5E+13	0	0
124	CH+O=CO+H	3.97E+13	0	0
125	CH+OH=HCO+H	3E+13	0	0
126	CH+HCCO=C2H2+CO	5E+13	0	0
127	CH2+CH2=C2H2+H2	1.2E+13	0	3.3
128	CH2+CH2=C2H2+H+H	1.08E+14	0	3.3
129	CH2+CH3=C2H4+H	4.22E+13	0	0
130	CH2+C2H3=C2H2+CH3	1.81E+13	0	0
131	CH2+O=CO+H+H	7.2E+13	0	0
132	CH2+O=CO+H2	4.8E+13	0	0
133	CH2+OH=CH2O+H	1.81E+13	0	0
134	CH2+HCO=CH3+CO	1.81E+13	0	0
135	CH2+HCCO=C2H3+CO	3E+13	0	0
136	CH2+HCCO=C2H+CH2O	1E+13	0	8.4
137	CH2(S)+M=CH2+M	1.51E+13	0	0
138	CH3+CH3(+M)=C2H6(+M)	3.61E+13	0	0
139	CH3+O=CH2O+H	8.43E+13	0	0
140	CH3+OH=CH2(S)+H2O	7.23E+13	0	11.6
141	CH3+HO2=CH3O+OH	1.8E+13	0	0
142	CH3+HCO=CH4+CO	1.2E+14	0	0
143	CH3+M=CH2+H+M	2.91E+16	0	379.1

161

144	C2H+C2H3=C2H2+C2H2	1.9E+13	0	0
145	C2H+O=CH+CO	1E+13	0	0
146	C2H+OH=HCCO+H	2E+13	0	0
147	C2H+OH=CH2+CO	1.81E+13	0	0
148	C2H3+O=CO+CH3	3E+13	0	0
149	C2H3+OH=C2H2+H2O	5E+12	0	0
150	C2H5+O=CH2O+CH3	6.62E+13	0	0
151	H2CCCH+O=C2H2+CO+H	1.39E+14	0	0
152	H2CCCH+OH=C3H2+H2O	2E+13	0	0
153	H2CCCCH+M=C4H2+H+M	1.12E+16	0	194.6
154	O+O+M=O2+M	5.4E+13	0	-7.5
155	O+HO2=O2+OH	3.19E+13	0	0
156	O+HCO=CO+OH	3.01E+13	0	0
157	O+HCO=CO2+H	3.01E+13	0	0
158	O2+CH3=CH3O+O	4.4E+13	0	131.4
159	O+CH3O=CH2O+OH	1.81E+12	0	0
160	O+CH2OH=CH2O+OH	9.03E+13	0	0
161	O+HCCO=H+CO+CO	9.64E+13	0	0
162	OH+OH=O+H2O	1510000000	1.1	0.4
163	OH+HO2=H2O+O2	2.89E+13	0	-2.1
164	OH+HCO=H2O+CO	1.02E+14	0	0
165	OH+CH3O=CH2O+H2O	1.81E+13	0	0
166	OH+CH2OH=CH2O+H2O	2.41E+13	0	0
167	OH+HCCO=HCO+HCO	1E+13	0	0
168	OH+HCCO=CH2O+CO	1E+13	0	0
169	HO2+HO2=H2O2+O2	4.22E+14	0	50.1
170	HO2+HO2=H2O2+O2	1.32E+11	0	-6.8
171	HCO+HCO=CH2O+CO	3.01E+13	0	0
172	HCO+M=H+CO+M	4.49E+14	0	65.9
173	CH3O+M=CH2O+H+M	1.55E+14	0	56.5
174	CH2OH+M=CH2O+H+M	1.26E+16	0	125.6
175	HCCO+HCCO=C2H2+CO+CO	1E+13	0	0

Table 5: The Leeds reaction mechanism for methane combustion[74]

Bibliography

[1] Juergen Mueller, "Micropropulsion for small spacecraft", Progress in Aeronautics and Astronautics, Volume 187, AIAA, 2000

[2] Mehra, A, "Development of a High Power Density Combustion System for a Silicon Micro Gas Turbine Engine", Ph.D. Thesis, MIT, Feb 2000.

[3] D. G. Shepherd, "Aerospace Propulsion", American Elsevier Publishing Company, Inc., p. 24.

[4] Mehra, A, "Development of a High Power Density Combustion System for a Silicon Micro Gas Turbine Engine", Ph.D. Thesis, MIT, Feb 2000.

[5] Zeldovich, Ya B., *Zh. Eksp. Theor. Fiz.*, 11:159-168 (1941)

[6] D. B. Spalding, *Proc. Royal Soc. A*, 240, 1220 (1957) 83-100.

[7] Hardesty, D. and Weinberg, F., *Combustion Sci. and Tech.* 8 (1974) 201-214.

[8] T. Takeno, K. and Sato, K *Combustion Sci. and Tech.* 20 (1979) 73-84.

[9] Peterson, R. B., *Microscale Thermophysical Engineering*, 2, pp 121-131, 1998

[10] Aichlmayr, H. T., Kittelson, D.B., and Zachariah, M. R., *Chemical Engineering Science*, v. 57, n. 19, Oct 21 2002, p. 4161-4171

[11] Daou, J. and Matalon, M., *Combustion and Flame* 128 (2002) pp. 321-339.

[12] Daou, J. and Matalon, M., "Flame Propagation in Channels: Differential Diffusion Effects", 3rd Joint Meeting of the U.S. Sections of The Combustion Institute, March 2003.

[13] Ronney, P.D., *Combustion and Flame* 135 (2003) pp. 421-439.

[14] Y. Ju, B. Xu, *Proc. Combust. Inst.*, vol. 30, 2005, pp. 2445-2453.

[15] D. G. Norton, D. G. Vlachos, *Combustion and Flame*, 138, pp 97-107 (2004).

[16] S. W. Churchill, *Chem. Eng. Technol.*, 12, pp 249-254 (1989).

[17] Alexeenko AA, Levin DA, Fedosov DA, Gimelshein SF, Collins RJ , *Journal of Propulsion and Power* 21 (1) 95-101 Jan-Feb 2005

[18] Ketsdever AD, Clabough MT, Gimelshein SF, Alexeenko A, *AIAA Journal* 43 (3): 633-641 March 2005

[19] Epstein, A. and Senturia, S. D., *Science* 1997, 276 1211

[20] Mehra, A, "Development of a High Power Density Combustion System for a Silicon Micro Gas Turbine Engine", Ph.D. Thesis, MIT, Feb 2000.

[21] Spadaccini, C. M, Zhang, X., Cadou, C. P., Miki, N., and Waitz, I. A., "Development of a Catalytic Silicon Microcombustor for Hydrocarbon-fueled Power MEMS", Proceedings of the IEEE Micro Electro Mechanical Systems (MEMS), 2002, p. 228-231

[22] Jeongmin Ahn, Craig Eastwood, Lars Sitzki and Paul D. Ronney, *Proc. Combust. Inst.*, vol. 30, 2005

[23] Miesse C, Masel RI, Short M, Shannon MA, *Combustion Theory And Modelling* 9 (1): 77-92 Feb 2005

[24] A.P. London, A.A. Ayon, A.H. Epstein, S.M. Spearing, T. Harrison and al, *Sensors and Actuators A* 92 pp351-357, 2001.

[25] Hitt D.L, Zakrzwski, C.M. and Thomas M.K., 2001, *Smart Mater. Struct.*, vol. 10, 1163-1175.

[26] Ketsdever AD, Clabough MT, Gimelshein SF, Alexeenko A, *AIAA Journal* 43 (3): 633-641 Mar 2005

[27] Leach, T. T., "Modeling and Simulation of the Micro-Combustion between Two Parallel Plates", M.S. Thesis, University of Maryland, 2003.

[28] T. Leach, C. Cadou, G. Jackson, *Combustion Theory and Modelling*, Vol. 10, No. 1, February 2006, 85–103.

[29] Mallard, E. and Le Chatelier, H. L., *Ann. Mines* 4 (1883) 379.

[30] D. B. Spalding, *Proc. Royal Soc. A*, 240, 1220 (1957) 83-100.

[31] Hardesty, D. and Weinberg, F., *Combustion Sci. and Tech*. 8 (1974) 201-214.

[32] T. Takeno, K. and Sato, K *Combustion Sci. and Tech*. 20 (1979) 73-84.

[33] Coffee, T.P., Kotlar, A.J., and Miller, M.S, *Combustion and Flame* 54 (1983) 155-169.

[34] Zhu, H. and Jackson, G.S., "Transient Modeling for Assessing Catalytic Combustor Performance in Small Gas Turbine Applications", 2001-GT-0520, Proceedings of ASME Turbo Expo 2001: 46th ASME International Gas Turbine & Aeroengine Technical Congress, New Orleans, LA, June 4-7, 2001.

[35] Miller, J. A., and Bowman, C. T., *Progress in Energy and Combustion Science* 15 (1989) 287-338.

[36] Deuflhard, P., Harier, E., and Zugck, J., *Numer. Math.* 51 (1987) 501-516.

[37] Miller, J.A., Mitchell, R.E., Smooke, M.D., and Kee, R.J., *Proc. Comb. Inst.* 19 (1982) 181.

[38] Law, C.K, "A Compilation of Experimental Data on Laminar Burning Velocities" in: N. Peters and B. Rogg, (Eds) Reduced Kinetic Mechanisms for Applications in Combustion Systems, Springer-Verlag, New York, 1993, pp. 15-26.

[39] Law, C.K. and Sung, C.J., *Progress in Energy and Combustion Science* 26 (2000) 459-505.

[40] Glassman, I., "Combustion", Third edition, Academic Press, 1996.

[41] Karniadakis, G.E. and Beskok, A., "Micro-Flows: Fundamentals and Simulation", Springer, New York, pp. 15.

[42] Karniadakis, G.E. and Beskok, A., "Micro-Flows: Fundamentals and Simulation, Springer", New York, pp. 15.

[43] Mohamed Gad-el-Hak, *ASME Journal of Fluids Engineering*, 121 (1999).

[44] N. G. Hadjiconstantinou, O. Simek, *ASME Journal of Heat Transfer*, 124 (2), 356-364.

[45] R. L. Panton, "Incompressible flow", Second edition, John Wiley and Sons, Inc.

[46] Ronney, P.D., *Combustion and Flame* 135 (2003) pp. 421-439.

[47] Mills, A. F., "Basic Heat and Mass Transfer", Irwin, pp. 241, 1995.

[48] Lide, D.R (ed.), "CRC Handbook of Chemistry and Physics", 81th ed.

[49] Miller, J. A., and Bowman, C. T., *Progress in Energy and Combustion Science* 15 (1989) 287-338.

[50] T. Takeno, K. and Sato, K *Combustion Sci. and Tech*. 20 (1979) 73-84

[51] A. Carlos Fernandez-Pello, *Proc. Combust. Inst.* 29 (2002)

[52] W. A. Strauss, R. Edse, *Proc. Combust. Inst.* 7 (1959) 377.

[53] K.J. Hughes, T. Turányi, A. Clague, M.J.Pilling, *Int. J. Chem. Kinet.,* 2001, 33, 513-538

[54] John D. Anderson, "Modern Compressible Flow", Third Edition, McGraw Hill.

[55] www.boeing.com/defense-space/space/propul/SSME.html

[56] J. Buckmaster, T. Takeno, *Combustion Science and Technology*, 25, pp 153-158 (1981).

[57] S. W. Churchill, *Chem. Eng. Technol.*, 12, pp 249-254 (1989).

[58] A. F. Mills, "Basic Heat and Mass Transfer", Irwin.

[59] A. F. Mills, "Basic Heat and Mass Transfer", Irwin.

[60] S. R. Turns, "An Introduction to Combustion", 2nd Edition, McGraw and Hill.

[61] T. P. Coffee, A. J. Kotlar, M. S. Miller, *Combust. And Flame* 54 pp 155-169 (1983).

[62] Glassman, I., "Combustion", Third edition, Academic Press, 1996, p. 174.

[63] Y. Ju, B. Xu, *Proc. Combust. Inst.*, vol. 30, 2005, pp. 2445-2453.

[64] Y. Ju, B. Xu, *Proc. Combust. Inst.*, vol. 30, 2005, pp. 2445-2453.

[65] D. G. Norton, D. G. Vlachos, *Combustion and Flame*, 138, pp 97-107 (2004).

[66] Scott Heatwole, "In Situ Infrared Diagnostics for a Silicon Walled Micro-Scale Combustion Reactor", MS Thesis, University of Maryland, 2004.

[67] Heatwole S, Cadou CP, Buckley SG, *Combustion Science And Technology* 177 (8): 1449-1461 Aug 2005

[68] Scott Heatwole, "In Situ Infrared Diagnostics for a Silicon Walled Micro-Scale Combustion Reactor", MS Thesis, University of Maryland, 2004.

[69] Heatwole S, Cadou CP, Buckley SG, *Combustion Science And Technology* 177 (8): 1449-1461 Aug 2005

[70] T. Coffee, A. Kotlar, M. Miller, *Combust. Flame*, 58 (1984) 59-67.

[71] C.K. Westbrook, F.L. Dryer, *Combust. Sci. Technol.* 27 (1981) 31–43.

[72] Mallard, E. and Le Chatelier, H. L., *Ann. Mines* 4 (1883) 379.

[73] Miller, J. A., and Bowman, C. T., *Progress in Energy and Combustion Science* 15 (1989) 287-338.

[74] K.J. Hughes, T. Turányi, A. Clague, M.J.Pilling, *Int. J. Chem. Kinet.*, 2001, 33, 513-538